Heat and mass transfer in solidification cladding.

SILISAN, Akin.

HEAT AND MASS TRANSFER

in

SOLIDIFICATION CLADDING

A

THESIS

presented

for the Degree of

DOCTOR OF PHILOSOPHY

in the

SHEFFIELD POLYTECHNIC

by

AKIN SILISAN

May, 1975.

3 НЕр*

/7~20373 o\

ABSTRACT

The conditions under which solidification cladding can be carried out are considered, and the heat and mass transfer phenomena involved in the process are investigated.

Most of the experiments involve the exposure of rotating cylindrical probes to liquid metal at various superheats as well as at zero superheat, and have been carried out using lead and tin and certain of their binary alloys.

The initial chill-layer formed on the probe is remelted only in the presence of superheat. The melt back of the chill-layer is succeeded by dissolution of the probe surface. The rates of chill-layer growth and melt-back as well as the rate of surface dissolution have been determined experimentally for various degrees of superheat and probe rotation speeds. The problem has also been approached from the theoretical point of view by:

1 adopting an integral profile method and applying it to a cylindrical geometry in order to predict the rate at which metal will solidify against a finite rotating cylindrical wall and the rate at which it subsequently remelts,

and

2 deriving the equations governing the relevant rate controlling dissolution mechanisms.

This theoretical work has involved the development of a model for unsteady conductive/convective heat transfer in a liquid metal, and an investigation into the mass transfer processes controlling the dissolution of lead and tin into lead/tin alloys. The results obtained in this work can be used to predict the heat and mass transfer conditions under which successful solidification cladding process can be carried out on an industrial scale.

LIST OF CONTENTS

		Page
1	Introduction	15
2	Literature Survey	17
2.1	Cladding.	18
2.2.	Solidification and its structures.	20
2.5	The theoretical solutions of the problem of heat transfer during solidification.	25
2.3*1	Approximate Solutions.	25
2.3.1.1	The integral profile method for planar solidification.	25
2.3.1.2	Application of integral profile method to nonplaner solidification.	27
2.3.1.3	Hills' solution.	29
2.4	Heat and mass transfer to rotating cylinders.	35
2.4.1	Fluid flow between concentric rofeting cylinders.	36
2.4.2	Heat transfer between concentric rotating cylinders.	40
2.4.3	Mass transfer from rotating cylinders.	42
3	Theoretical treatment	44
3.1	Introduction.	44
3.2	Limensionless model for a growing layer on a plane finite wall.	45
3.3	Application of Hill's integral profile method for solidification onto the outside of a cylindrical probe.	47
3.3.1	Heat flow in the chill-layer.	48
3.3.2	Heat flow in the probe-wall.	52
3.3*3	Heat flow in the liquid metal.	54
3.3.3*1	The decay of the conduction layer.	58
3.3.4	Numerical methods of solution and computer programme.	60
3.4	Mass transfer - Dissolution process.	62
3.4.1	The nature and kinetics of the dissolution process.	62
3.4.2	Transport controlled dissolution.	63
4	The apparatus and the nrobe	68
4.1	The apparatus.	68
4.1.1	The furnace .	69
4.1.2	The probe assembly and the rotating mechanism.	71

		Page
4.1.3	The control panel and the recorders.	75
4.2	The cylindrical probe.	77
4.2.1	Precasting preparations.	79
4.2.2	Casting of the probes.	81
5	Experimental procedure	82
5.1	Experimental sequence.	82
5.1.1.1	Zero bath superheat.	83
5.1.1.2	Superheated baths.	85
5.1.2	Dissolution experiments.	85
5.1.3	Preparation of micro and macro structures.	86
5.1.3.1	Pb - Sn in their pure form.	86
5.1.3.2	Pb - Sn alloys.	88
6	Results	93
6.1	Chill-layer results.	93
6.1.1	Chill-layer growth at zero superheat.	93
6.1.2	Chill-layer growth and melt-back in superheated baths.	93
6.1.3	Microstructural examination of chill-layer.	104
6.2	Dissolution results.	105
6.2.1	Dissolution rates.	105
6.2.2	Calculation of mass transfer coefficient.	109
6.2.3	Visual observation of the probe surface.	118
6.2.4	Metallographic examination of the dissolving probe materials.	128
7	Discussion	140
7.1	Introduction.	140
7.2	Theoretical treatment of the heat transfer phenomenon.	140
7.2.1	A comparison of the integral profile methods for cylindrical and planar cases at zero superheat.	140
7.2.2	Interface heat transfer coefficient.	143
7.2.3	The prediction of chill-layer growth and melt back in the presence of superheat.	143
7.2.4	The conduction/convection model for heat flow in the liquid metal.	145
7.3	Dissolution of lead, tin and lead/tin alloys in molten lead/tin eutectic.	154
7.3.1	Mechanism of the dissolution process.	154
7.3.2	Effect of grain size, orientation and grain boundaries.	154

Page

7.3.3 Morphology of the dissolution interface and fluid flow. 155

7.3.4 Effect of rotation speed on dissolution rates. 158

7.3.5 Comparison with previous work. 159

7.4 Accuracy of comparison between the theory and the experiments. 161

7.4.1 Heat losses during chill-layer experiments. 161

7.4.2 The accuracy of the theory. 163

7.4.2.1 Heat transfer phenomena. 163

7.4.2.2 Dissolution. 164

7.4.3 Errors of measurement. 164

7.4.3.1 Thickness. 164

7.4.3.2 Time. 164

7.4.3.3. Temperature. 165

7.4.3.4. Additional possible sources. 166

8 Conclusion. 167

APPENDICES

1 An attempt to grow a bonded layer. 168

2 Tables of experimental chill-layer results. 171

3 Tables of experimental dissolution results. 180

4 Analysis of materials used. 188

5 Physical and thermal properties of Pb, Sn, Pb-Sn eutectic and stainless steel. 189

Nomenclature. 190

Bibliography. 194

Acknowledgements. 198

FIGURES

		Page
Figure 1	Various morphologies of Alloy solidification.	21
2	The relationship between the ratio G/R and solute concentration.	22
3	The different macrostructual zones in an ingot	23
4	The effect of cooling rate on the size and shape of crystals.	23
5	Effect of different profile equations, for the radial temperature distribution, in an infinite medium surrounding a cylindrical cavity, on the predicted surface temperature of the cavity.	28
6	Temperature distribution across a layer of solidifying metal under linear heat flow conditions.	29
7	Diagram of Taylor vortices.	37
8	Vortices between rotating cylinders.	39
9	Heat transfer during growth of the chill-layer, on a plane finite wall.	46
10	Heat transfer during growth of a chill-layer on a cylindrical probe.	47
11	Heat flow in the probe wall.	52
12	The relationship between the main program and the subroutines.	61
13	Typical phase diagram for a binary alloy system A/B involving two solid solutions.	63
14	Boundary conditions for transport in a liquid with moving boundaries.	63

		Page
15	The apparatus.	68
16	The Furnace.	70
17	Section of Rotating Probe support with sliprings.	73
18	Section of lead probe.	78
19	Parts of the steel mould.	79
20	Main reading area.	84
21	Chill-layer thickness versus time for zero superheat.	94
22	Wall-temperature versus time for zero superheat.	95
23	Chill-layer thickness versus time for $3^{o}C$ superheat.	96
24	Chill-layer thickness versus time for $7^{o}C$ superheat.	97
25	Wall-temperature versus time for $7^{o}C$ superheat.	98
26	Chill-layer thickness versus time for $12^{o}C$ superheat.	99
27	Chill-layer thickness versus time for $17^{o}C$ superheat.	100
28	Wall temperature versus time for 17^{o} and $20^{o}C$.	101
29	Chill-layer thickness versus time for 27 and $37^{o}C$ superheat.	102
30	Wall temperature and probe - chill-layer interface temperature versus time for $27^{o}C$ superheat.	103
31	Average rates of dissolution at 60 r.p.m. for pure lead.	107
32	Average rates of dissolution for pure lead at different rotation speeds but constant temperature ($230^{o}C$.)	108

		Page
33	Average rates of dissolution for pure lead probes at 120 r.p.m. rotation speed.	110
34	Average rates of dissolution of pure tin probes at 200°C.	111
35	Average rates of dissolution of 90% Pb - 10% Sn probes at 230°C.	112
36	Lead - tin phase diagram.	116
37	Comparison of the present limiting mass transfer coefficient with some other investigations.	117
38	Chill-layer thickness versus Time curves for planar and cylindrical integral profile methods (zero superheat).	141
39	Chill layer thickness versus exposure time. Eutectic Sn-Pb, 20°C superheat, Pb insert ^{6}	146
40	Chill-layer thickness versus time (pure conduction).	151
41	Theoretical chill-layer thickness versus time curves for different half-life times	151
42	Chill-layer thickness versus time curves Stainless steel probe Pb-Sn eutectic bath.	153
43	Braking of Taylor vortices at high rotation speeds	157
44	Typical shapes of chill-layer during growth and meltback.	162
45	The theoretical curves representing chill-layer growth, meltback, dissolution and cladding at 186° and 195°C.	170

PiATES

		Page
Plate 1	The apparatus .	72
Plate 2	A close up to the rotax^n mechanism .	74.
Plate 3	The control panel of the apparatus *	76
Plate 4	Precasting arrangements.	80
Plate 5	Microstructure of Pb~Sn eutectic hath as cooled in air,	89
Plate 6	Chill-layer growth on a Pb-probe under unstirred conditions.	90
Plate 7	Chill-layer growth on a Pb-probe under stirred and unstirred conditions .	91
Plate 8	Microstructure of the chill-layer .	92
Plate 9	A Pb-Probe, as machined prior to dissolution experiment.	119
Plate 10	A dissolution experiment carried out with Pb-probe without surface **machining ,**	**120**

Plate 11 Dissolution at a static Pb - Probe .

Plate 12 A dissolution experiment carried out with Sn probe at 41 r.p.m.

Plate 13 A dissolution experiment carried out with a Pb - probe at 60 r.p.m,

Plate 14 A dissolution experiment carried out with Pb-probe at 40 and 80 r.p.m.

Plate 15 A dissolution experiment carried out with a Sn-probe at 60 r.p.m.

Plate 16 A dissolution experiment carried out with Pb-probe at 120 r.p.m.

Plate 17 A dissolution experiment carried out with Sn-probe at 60 r.p.m.

Plate 18 Macrostructure of a Pb-probe after a dissolution experiment. Sectioned normal to the surface, viewed by oblique illumination.

Plate 19 Typical ambiguous structure produced as a result of incomplete preparation technique.

Page

Plate 20 Macrostructure of a Pb-probe after a dissolution experiment. 131

Plate 21 Ditto 132

Plate22 Surface structure of a 80% Sn, 20% Pb alloy before and after dissolution. 133

Plate 23 Microstructure of metals in Plate 22. 134

Plate 24 Surface appearance and microstructure of a 90% Sn, 10% Pb alloy probe after 40 secs. of dissolution time. 136

Plate 25 Microstructure of a 90 wt % Sn, 10 wt. % Pb alloy probe after 60 seconds of dissolution time. 137

Plate 26 Macrostructure of a Snprobe after a dissolution experiment. 138

Plate 27 Surface appearance and microstructure of a 90 wt. % Pb, 10 wt. % Sn alloy probe after 100 sec. of dissolution time. 139

TABLES

		Page
1	Chill-layer thickness results for "zero" superheat.	172
2	Chill-layer thickness results for "3°C" superheat.	173
3	ditto "7°C" "	174
4	ditto "12°C" "	175
5	ditto "17°C" "	176
6	ditto "27°C" "	177
7	ditto "37°C" "	178
8	ditto "47, 57, and 67°C." superheat.	179
9	Dissolution results.	106
10	Dissolution rates of pure lead probes in Pb-Sn eutectic bath (30 r.p.m.).	181
11	Dissolution rates of static pure lead probes in Pb-Sn eutectic bath.	182

Page

Table 12 Dissolution rates of pure lead probes in Pb-Sn eutectic baths (60 r.p.m.) 183

13 Dissolution rates of pure lead probes in Pb-Sn eutectic bath (120 r.p.m.) 184

14 Dissolution rates of 90% lead 10% tin probes in lead-tin eutectic bath (50, 100 r.p.m. 185

15 Dissolution rates of pure tin probes in Pb-Sn eutectic bath (30,41 r.p.m.) 186

16 Dissolution rates of pure tin probes in Pb-Sn eutectic bath 60, 120 r.p.m. 187

17 Calculation of mass transfer coefficients for Pb-probes. 113

18 Calculation of mass transfer coefficients for Sn - and %10 Sn, %90 Pb-probes. 114

INTRODUCTION

The idea of combining two materials by coating one with the other, to give a composite material, having the more desirable properties of each of the components, has obvious attractions to metallurgists and engineers. In this manner the extra cost of fabricating relatively expensive alloys can be eliminated, and the savings can be used much more satisfactorily in other directions.

Brooks has recently highlighted the difficulties of cladding by casting processes.

Hills and Brooks* have shown that the liquid metal must attack the surface of the solid metal if a bond is to be formed in this type of process, either by partial melting or by dissolution.

Strong bonds can only be produced, therefore, under certain specific conditions of heat transfer.

Hills and Brooks* have designed an experimental apparatus in which these conditions can be realized and studied, and have used this apparatus in attempts to bond stainless steel to cast iron and a lead/tin eutectic to lead. They have also used Hill's integral-profile method [10] to predict the heat transfer conditions required to bond one pure metal to another pure metal. They found however some discrepancies between theoretical and experimental results; this is thought to be partly as a result of applying an integral profile method derived for planar shapes to an axi-symmetrical heat flow situation. They were not able to form a bond between stainless steel and mild steel because of the high rate at which the stainless steel was dissolved by the molten mild steel, and because of the apparently random nature of the dissolution process.

* Unpublished work

The main objects of the present work are to study the pre-cladding conditions, by investigating:

1 the heat transfer phenomenon occurring during solidification and meltback of the chill-layer formed on a cylindrical rotating substrate when immersed in melts at different temperatures,

and

2 the substrate dissolution process that commences after meltback of the chill layer under static and dynamic conditions.

2 Literature Survey

After a brief review of the various processes for the cladding of one metal with another metal, an introductory review is presented of the structure of cast metals. This is followed by a listing of the mathematical methods for the prediction of solidification rates, followed by a detailed presentation of one integral-profile method.

The experimental apparatus used in the work described in this thesis involves fluid flow and heat and mass transfer in an annular space between two rotating cylinders. Relevant knowledge about these processes is reviewed in the final sections of the literature survey.

Cladding

Increasingly dissimilar materials are being brought together to solve material problems in all aspects of manufacturing.

Rolled gold and 'Sheffield plate' (silver on a copper based substrate,) were the earliest examples of cladding.

Hot pressure rolling or electro-welding, were the processes used to join the coatings to the substrate.

Copper cladding of steel is especially useful for wire or tube, and is normally carried out by casting.

The ductilities and thermal properties of steel and nickel are so similar, that nickel cladding is particularly useful for steel.

Electro-welding, hot compacting, (rolling or pressing), or casting, can be used to bond stainless steel to carbon steel, but the bond strength is generally dependent upon the quality of fluxing.

Shepherd and Brooks [1] have reviewed the major processes that have been used to produce stainless clad steels.

Although not yet widely accepted, lead clad steel sheet, produced by roll bonding has considerable potential.

The desirability of obtaining cheap aluminium coating for mild steel, has led to interest in applying metal powders to the surface of steel strip, followed by a compaction or sintering process.

The Elphal process of Bisra has used electrophoresis to deposit aluminium from a suspension in methanel. [2,3]

A parallel Japanese development [4] uses atomized injection to apply aluminium powder to the steel surface, and to ensure bonding, after a drying operation, an adhesive of the polymethaphosphate type is used.

Jenkins [5] reviewed similar developments for chromium and zinc, and clearly there may be rapid advancements in this field.

Brooks [6] has recently highlighted the difficulties of cladding by casting processes.

The work presented here, continues his work by investigating pre-cladding conditions (e.g. surface cleanliness and smoothness, the influence of different modes of fluid materials) and proceeds to explain some of the phenomena involved.

2.2 Solidification and its Structures

The structures of the solidified metals are determined by three major factors:

1 Alloy constitution;

2 Thermal conditions;

3 Impurities.

Metal composition governs the basic mode of crystallisation, end determines whether the equilibrium structure will consist of a single phase or eutectic grains, or both. The composition cf alloy is also characterised by the distribution a^d diffusion coefficients of the solute in the liquid, and solid phases, which- determine tendencies for COnStitUtionai under cooling and segregation.

The temperature distribution and rate of cooling in solidifying metals depend on the initial temperature conditions, and the thermal -rope: L'*es of metal and mould. Since wide variations in thermal conditions can occur at various stages during the cooling of a metal, its overall structure may consist of separate zones with widely different characteristics.

The relative possibilities for nucleation and growth depend upon foreign particles, or solutes present in the liquid, e.g. a pure metal solidifies with a plane solid/liquid interface, and the resulting micro-structure will only show very thin grain boundaries. When a minute quantity of solute is present, the solid/liquid interface will show small grooves, and the resulting micro-structure will show thick cell boundaries, (cellular structure). When the amount of solute is no longer small, its rejection may lead to the formation dendrites which can either be oriented in the heat flow direction (columnar dendrites) or randomly oriented. Where the oriented phase does not form secondary arms, the structures are called composites, or fibrous dendritic structures.

INTERFACE

-Decreasing temperature gradient

rate of solidification

CELLULAR INTERFACE

v..v

ORIENTED DEK-RITES

'i'W.'S •.•'v'o

V*fJ' :

W y m f m

RANDOMLY ORIENTED

^ ——*1 * *< % 'J

FIBROUS DENDRITES

[sj *SOLID*

rr^i *f tr>l ME)*

VARIOUS MORPHOLOGIES OF ALLOY SOLIDIFICATION

(a) dong heat Row direction
(b) microstructure normal to beat flay/ ai solidus front

Figure 2

The relationship between the ratio G/H. and the solute concentration

The ratio /„ (where G is temperature gradient, and R the rate of freezing), is a significant parameter, with respect, both to mode of growth, and to final structure in solid solution alloys. These successive stages are illustrated schematically in Figure 1 and the associated thermal conditions in Figure 2.

In the present investigation the microstructure of the solid layer growing on the substrate as well as the microstructure of the substrate itself have been observed and considered in relation to these various factors.

The Macro Structure of Solidified Metals

It is generally recognized that three macrostructural

Figure 5

The Different Macrostructural Zones in an Ingot

zones st in one solidified ingot:

1 a "chill" zone ox fine griins,

2 a "columnar zone" containing grains elongated in the direction of heat flow,

3 a control zone of "ecuiaxed" grains.

These zones are shown shema^cally in Figure 3 andmay occur in various proportions, depending principally upon the rate of heat extraction, the amount and composition of the metal, and the potency of the nucleans present. The metalographic examination at the neat extraction direction of the lead and

(b) (c)

The Effect of Cooling Rate on the Size and Shape of crystals in

a pure metals and intermetalio compounds,

b solid solution alloys and

c eutectics.

tin probes used in this work showed the existence of the "chill" and "columnar" zones. Their significance and possible causes at the solution interfaces is discussed later in the thesis.

In Figure 4, the effect of the cooling rate on the size and shape of crystals in pure metals, solid solutions, alloys and eutectics can be seen.

2.3 The Theoretical Solution of the Problem of Heat Transfer during Solidification

The unsteady state heat conduction problem, which deals with one dimensional heat flow during solidification, or melting of material, is often referred to as the problem of "Stefan". This problem has been the subject of numerous theoretical investigations, which can be divided into two broad categories.

(a) Approximate mathematical solutions using realistic and almost realistic solidification conditions, and

(b) exact solutions under conditions rarely achieved in practice.

2.3.1 Approximate Solutions

Two types of approximate mathematical methods which can be used are:

(a) Numerical integration of the equations by finite difference methods, and

(b) integral profile technique.

The first method has the disadvantage of being very lengthy and tedious to apply, and must be repeated each time a parameter is changed. The use of this method is described by Landau [8] and Forster. [9]

2.3.1.1 The Integral Profile Method for Planar Solidification

The integral profile method (sometimes known as the heat balance integral) reduces the nonlinear boundary value problem to an ordinary initial value problem, which gives useful solutions quite easily and in many cases leads to expressions which can be solved analytically.

Hills' [10] integral profile solution for solidification of pure metals has been used in the development of the theory

presented in Chapter 3, and a full account of it is given below.

Integral methods were first introduced by Von Karman and Pohlhauser in order to solve non-similar boundary layer problems in fluid mechanics.[11] Goodman[12] has applied the 'Heat Balance Integral' to problems involving phase changes, and to problems involving the heating of bodies under linear and non-linear boundary conditions.[13] This method was further used in analysing the melting of finite slabs[14] and for materials with temperature dependent thermal properties.[15] Some numerical results for the case of a linearly varying surface temperature, and for constant heat flux are presented in Reference.[16]

An integral profile approach to the solidification of alloys was used by Tien and Geiger[17] who assumed in their treatment that the cooled surface remained at a constant temperature below the solidus throughout the solidification process. This unrealistic boundary condition has been replaced in a subsequent solution given by the same author.[18] Koump and Tien s[19] have developed a method involving a time dependent surface temperature.

Schneider[20] considers radiation cooling of finite slabs, while additional comments on, and applications of, the integral method are presented, in references[21,22].

In his most recent paper Hills[10] has concisely described a general integral profile solution, which allows solidification rates to be predicted under a wide range of different cooling conditions. The method is a generalisation of the integral profile methods previously developed by Goodman and Hills.[12,23,2

The generalization has been achieved by characterising the layers of solidified metals in terms of two variables, rather than the simple variable used before, and by formulating the relevant differential equations, in terms of the heat flow from the cooled surface, and its partial differentials, and the heat flux to the solidification interface. Hills' method has been the basis for the theory developed here, for cylindrical case, as presented in Chapter 3, and a full account

of it is given in Section 2.3.1.3

2.3.1.2 Application of Integral Profile Method to Non-Planar Solidification

In all the above mentioned papers, in Chapter 2.3.1.1, with exception of References [21,22] the integral method has been applied to problems of planar geometry.

Veinik [22] treats several heat conduction problems, in both planar and non-planar geometries, under the assumption that the spatial temperature distribution are polynomial functions.

However, Sparrow [25] in a recent discussion, has indicated that some inaccuracy is present in the application of Goodmans Heat Balance integral approach, with polynomical profiles to problems involving non-planar geometry.

Thomas J. Lardner and Frederick V. Pohle [25] analyzed the case in which a cylindrical boundary is exposed to a constant heat flux, and showed the surface temperature to be logarithmically dependent on the cylinder radius i.e.

$$T = U \times (\ln r)$$

where $U = T \times r$

Their result is presented in Figure 5 for parabolic and logarithmic profiles with the exact solution.

In the present investigations the cylindrical heat conduction equations has been used together with a linear profile, which has been found sufficiently accurate to tackle the present solidification problem.

Figure 5

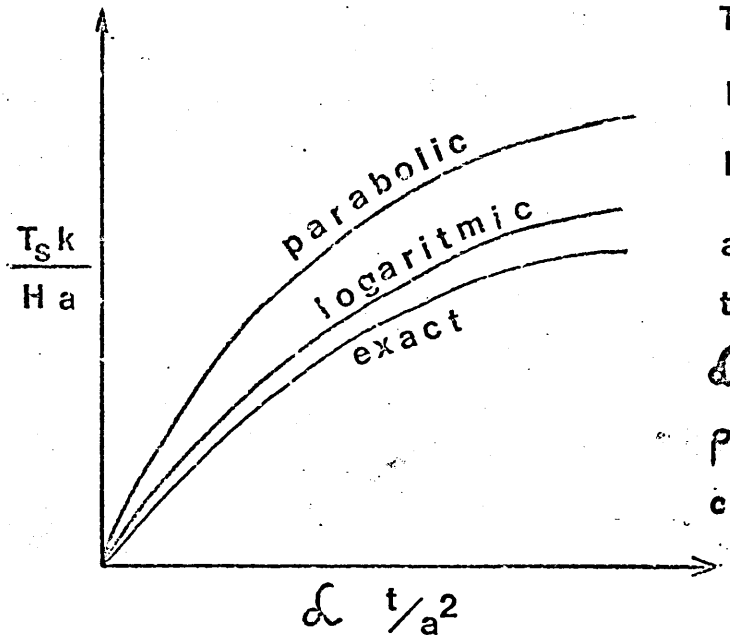

T_s	Surface temperature
k	thermal conductivity
H	constant flux
a	radius of cylinder hole
t	time
α	diffusivity, $k/\rho . c$
ρ	mass density
c	specific heat per unit mass

Effect of different profile equations for the radial temperature distribution in an infinite medium surrounding a cylindrical cavity on the predicted surface temperature of the cavity.

2.3.1.3. Hills' Solution to the integral Profile Method for a Growing Layer of Solid Metal

Hills' solution is presented in terms of two parameters, the temperature of the cooled surface and the thickness of the solid layer. Two simultaneous ordinary differential equations are derived for these parameters. The derivation is discussed here in some detail as it provides a general illustration of the integral profile method and it forms the basis of the theoretical methods developed later in this work.

Figure 6 Temperature distribution across a layer of solidifying metal under linear heat flow conditions.

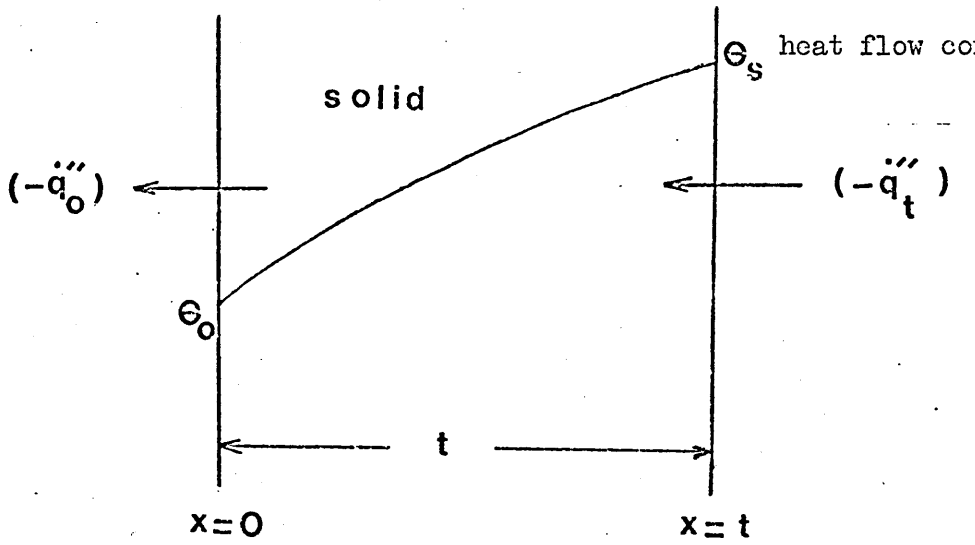

The above Figure 6 illustrates the growing solid layer, cooled at the surface, $x = 0$. Heat crosses the moving boundary, $x = t$ from the liquid metal. The temperature distribution within the solid metal must satisfy the unsteady state heat conduction equation

$$k \frac{\partial^2 \theta}{\partial x^2} = \rho c \frac{\partial \theta}{\partial \tau} \qquad (1)$$

The integration of this equation across the solid layer yields

$$\int_0^t \left[\frac{\partial^2\theta}{\partial x^2}\right]_k \partial x = \int_0^t \rho \cdot c \frac{\partial \theta}{\partial \tau} \, dx \qquad (2)$$

or applying the Leibnitz * integral formula to the right-hand side,

$$k\left[\frac{\partial \theta}{\partial x}\right]_t - k\left[\frac{\partial \theta}{\partial x}\right]_0 = \frac{d}{d\tau}\int_0^t \rho \cdot c\theta dx - \rho c \frac{dt}{d\tau}(\theta)_t \qquad (3)$$

Applying the heat conservation principle at the boundaries

$$-k_s\left[\frac{\partial \theta}{\partial x}\right]_0 = \dot{q}''_0 \qquad (4)$$

and

$$-k_s\left[\frac{\partial \theta}{\partial x}\right]_t = \dot{q}''_t - \rho H \frac{dt}{d\tau} \qquad (5)$$

Thus equation (3) becomes

$$\rho H \frac{dt}{d\tau} - \dot{q}''_t + \dot{q}''_0 = \frac{d}{d\tau}\left\{\int_0^t \rho c\theta dx - \rho c\theta_s \frac{dt}{d\tau}\right\} \qquad (6)$$

The most convenient auxillary function to use in evaluating the integral in equation (6) is a quadratic polynomial.

$$\theta = a_0 + a_1\left(\frac{x}{t}\right) + a_2\left(\frac{x}{t}\right)^2$$

The coefficients can be evaluated using the boundary conditions and equations (4), which gives

$$\theta = \theta_0 - \frac{\dot{q}''_0 t}{k}\left(\frac{x}{t}\right) + \left(\theta_s - \theta_0 + \frac{\dot{q}''_0 t}{k}\right)\left(\frac{x}{t}\right)^2 \qquad (7)$$

so that the integral becomes

$$\int_0^t \theta \, dx = \left(\frac{1}{3}\theta_s + \frac{2}{3}\theta_0 - \frac{1}{6}\frac{q''_0 t}{k}\right) t \qquad (8)$$

As the integral of an approximate function is more accurate than the function itself, the approximate integral can be substituted in equation (6) without great error.

Differentiating the resulting equation and re-arranging gives

---

* Page 48

$$\left\{\rho H + \frac{1}{3}\rho c\left[2(\theta_s - \theta_o) + \frac{\dot{q}_o'' t}{k}\right]\right\}\frac{dt}{d\tau} - \frac{2}{3}t\rho c\frac{d\theta_o}{d\tau} +$$

$$\frac{1}{6}t^2\frac{\rho c}{k_s}\frac{d\dot{q}_o''}{d\tau} = -(\dot{q}_o'' - \dot{q}_t'') \qquad (9)$$

The variables can be most easily expressed in dimensionless form as

$$t^* = \frac{-\left[\dot{q}_o''\right]_o t}{\theta_s k} \qquad \text{Dimensionless thickness} \qquad (10)$$

$$\theta^* = \frac{\theta_o}{\theta_s} \qquad " \qquad \text{surface temp.} \qquad (11)$$

$$\xi = \frac{\left[\dot{q}_o''\right]_o^2 \tau}{\theta_s^2 \rho c k} \qquad " \qquad \text{time} \qquad (12)$$

$$H^* = \frac{H}{c\theta_s} \qquad " \qquad \text{latent heat} \qquad (13)$$

$$q_o^* = \frac{\dot{q}_o''}{\left[\dot{q}_o''\right]_o} \qquad " \qquad \text{surface heat flux} \qquad (14)$$

$$q_t^* = \frac{\dot{q}_t''}{\left[\dot{q}_o''\right]_o} \qquad " \qquad \text{heat flux from liquid metal} \qquad (15)$$

In terms of these variables, equation (9) becomes

$$\left\{H^* + \frac{2}{3}(1 - \theta^*) - \frac{1}{3}t\,q_o^*\right\}\frac{dt^*}{d\xi} - \frac{2}{3}t^*\frac{d\theta}{d\xi} -$$

$$\frac{1}{6}t^{*2}\frac{dq_o^*}{d\xi} = q_o^* - q_t^* \qquad (16)$$

In general, the heat flux from the surface will be a function of the surface temperature, or of time, or of both. Thus we can write

$$q_o^* = f(\theta_o^*, \xi) \qquad (17)$$

$$\frac{dq_o^*}{d\xi} = \frac{\delta f}{\delta \theta}\frac{d\theta^*}{d\xi} + \frac{\delta f}{\delta \xi} = f'_\theta \cdot \frac{d\theta^*}{d\xi} + f'_\xi \qquad (18)$$

Re-arranging equation (16) in forms of these partial differentials gives

$$\left\{ H^* + \frac{2}{3}(1-\theta^*) - \frac{1}{3} t^* q_o^* \right\} \frac{dt^*}{d\xi} - \frac{1}{6} t^* (4 + f_\theta' t^*) \frac{d\theta^*}{d\xi} =$$

$$= q_o^* - q_t^* + \frac{1}{6} t^{*2} f_\xi' \qquad (19)$$

Finally equation (19) gives a differential equation consisting of two variables:

1 Dimensionless thickness of solidified metal

2 " surface temperature of the metal.

But in order to solve the above equation, we require another equation and this can be derived by considering the variation of $\frac{d\theta^*}{d\tau}$ across the solid metal layer.

At the stationary surface, x = 0, we can write

$$\left[\frac{d\theta}{d\tau}\right]_o = \frac{d\theta_o}{d\tau} \qquad (20)$$

At the moving surface, x = t, the temperature is constant so we can write

$$\frac{d}{d\tau}\theta(t,\tau) = \left[\frac{\delta\theta}{\delta x}\right]_t \frac{dt}{d\tau} + \left[\frac{\delta t}{\delta \tau}\right]_t = 0 \qquad (21)$$

Re-arranging this equation and substituting for the temperature gradient from equation (5) gives

$$\left[\frac{d\theta}{d\tau}\right]_t = - \frac{dt}{d\tau}\left\{\frac{\rho H}{k}\frac{dt}{d\tau} - \frac{\dot{q}_t''}{k}\right\} \qquad (22)$$

Integrating the heat conduction equation (1) across the solid layer gives

$$\left[\frac{\delta\theta}{\delta\tau}\right]_t - \left[\frac{\delta\theta}{\delta\tau}\right]_o = \frac{k}{\rho c}\left\{\left[\frac{\delta^2\theta}{\delta x^2}\right]_t - \left[\frac{\delta^2\theta}{\delta x^2}\right]_o\right\} = \frac{k}{\rho c}\int_o^t \frac{\delta^3\theta}{\delta x^3}\,dx \qquad (23)$$

Substituting (20) and (22) into equation (23) we get

$$-\frac{dt}{d\tau}\left\{\frac{\rho H}{k}\frac{dt}{d\tau} - \frac{\dot{q}_t''}{k}\right\} - \frac{d\theta_o}{d\tau} = \frac{k}{\rho c}\int_o^t \frac{\delta^3\theta}{\delta x^3}\,dx \qquad (24)$$

From equation (24) it seems that it is necessary to know accurately the temperature distribution across the solid layer. If there is no sudden change of cooling conditions

the value of $\frac{\partial \theta}{\partial x}$ would not change very much within the solid layer and, assuming this change to be linear, the value of $\frac{\partial^2 \theta}{\partial x^2}$ will not alter significantly within the solid. The integral appearing on the right hand side of equation (24) is thus given by

$$\int_0^{\delta} \frac{\partial^2 \theta}{\partial x^2}\, dx = \left(\frac{\partial \theta}{\partial x}\right)_{x=\delta} - \left(\frac{\partial \theta}{\partial x}\right)_{x=0} \qquad (25)$$

Differentiating the heat conduction equation equation (i), with respect to x gives

$$\frac{\partial^2 \theta}{\partial x \partial t} = \frac{\partial^2 \theta}{\partial x^2} \qquad (26)$$

Substituting equation (4) mfc (26) ant)(25) and writing this equation for x = o

$$\left(\frac{\partial q}{\partial r}\right)_{r=0} = \left(\frac{\partial \theta}{\partial t}\right)_{r=0} \qquad (27)$$

thus equation (24) becomes

$$\frac{d\delta}{dt} \int_0^{\delta} \theta\, dr + \left(\frac{\partial \theta}{\partial t}\right)_{r=\delta} \delta = \left(\frac{\partial q}{\partial r}\right)_{r=0} \qquad (28)$$

Re-arranging (28) in terms of dimensionless variables and substituting from equation (18) gives

$$\frac{d\delta^*}{d\tau} = \frac{\int_0^{\delta^*} \theta^*\, dr^* + \left(\frac{\partial \theta^*}{\partial r^*}\right)_{r^*=\delta^*}}{1 + \delta^* \left(\frac{\partial \theta^*}{\partial t^*}\right)_{r^*=\delta^*}} \qquad (29)$$

Substituting this equation in (19) we get a quadratic equation in

$$\frac{d\delta^*}{dt^*}$$

$$\left(\frac{d\delta^*}{dt^*}\right)^2 \left(\frac{\partial \theta^*}{\partial t^*}\right)_{r^*=\delta^*} + \frac{d\delta^*}{dt^*} \left(\frac{\partial \theta^*}{\partial r^*}\right)_{r^*=\delta^*} - \left(\frac{\partial^2 \theta^*}{\partial r^{*2}}\right)_{r^*=\delta^*} = 0 \qquad (30)$$

where $\theta = E\, t\, (4 + t f_Q)$ (31)

$$\left(\frac{\partial^2 \theta^*}{\partial r^{*2}}\right)_{r^*=\delta^*} = \left(\frac{\partial \theta^*}{\partial r^*}\right)_{r^*=\delta^*} + 4\,(1 - \theta^*) - 2\delta^* q^* \qquad (32)$$

$$+ q^* \delta^* (4 + t f_Q)$$

$$A = 6(q^* - \quad)(1 + \delta^* \quad) - 3 \quad \delta^* \qquad (33)$$

Thus we can write

$$\frac{dt^*}{d\xi} = \frac{-\Gamma^* \pm \sqrt{\Gamma^{*2} + 4\Lambda^*\Omega^*}}{2\,\Omega^*} \qquad (34)$$

Since q_t^* is less than q_o^*, Λ^* and $dt^*/d\xi$ will both be positive and the positive root of equation (30) is relevant. Multiplying both sides of equation (34) with $(\sqrt{\Gamma^{*2} + 4\Lambda^*\Omega^*} + \Gamma^*)$ we get

$$\frac{dt^*}{d\xi} = \frac{2\,\Lambda^*}{\Gamma^* + \sqrt{\Gamma^{*2} + 4\Lambda^*\Omega^*}} \qquad (35)$$

Equation (35) has no irregularities in this form and can be integrated numerically with equation (30) providing algebraic expressions are available for $\dot{q}^*_o$, f'_θ, f'_ξ and $\dot{q}_t^*$.

2.4 Heat and mass transfer to rotating cylinders

Heat and mass transfer between rotating cylinders has been fairly extensively investigated. These transport properties are affected very significantly by the geometry of the flow patterns between the two cylinders. At low rotation speeds a laminar flow pattern is set up known as Couette flow in which the fluid between the cylinders flows in a tangential velocity, there being a uniform velocity gradient across the annular space. When the inner cylinder is rotating and the outer cylinder is at rest, centrifugal forces will tend to cause fluid to flow radially. This can result in breakdown of the laminar Couette flow, and this can strongly affect heat and mass transfer to the rotating cylinder.

Fluid Flow between Concentric Rotating Cylinders

A considerable amount of work has been done on fluid flow between concentric rotating cylinders concerning rotation of both cylinders, or one stationary, one rotating, with different speeds as well as different directions. A large proportion of this work considers either a narrow gap, or non metallic fluids. Most of the fundamental work has been reviewed by Forfman [30] in his section on rotating cylinders.

Taylor, [31] in a very early paper, showed that above a critical speed of rotation, the laminar Couette flow breaks down into a flow consisting of a set of cellular, toroidal vortices spaced regularly along the axis of the two cylinders. Figure 7 shows a cross section of these three dimensional ring-shaped vortexes.

Hagarty [32] has photographed such vortex patterns, using the optical property of glycerine and water solutions, and concluded that there are three modes of flow when the annulus is very long:

1 When the inner cylinder rotates slowly, all particles move in circular paths concentric with the axis of the cylinders. This is a form of gouette motion.

2 As the speed of rotation of the inner cylinder is increased, a stable secondary motion develops. Pairs of ring vortexes appear. In this motion each particle of fluid rotates simultaneously about the axis of the rotating cylinder, and about the core of the ring vortex, of which it is a part.

3 At relatively high speeds of rotation, the vortex motion becomes unstable, and the motion becomes generally irregular and turbulent.

Fritz Schultz Gruncw and Hans George Hein [33] used a similar technique for examining Taylor Yortices, and showed that their number decreases with increasing speed. Evidence of this phenomenon has been observed on the rotating probes of the present investigation, as ring shaped grooves, wdiich increased

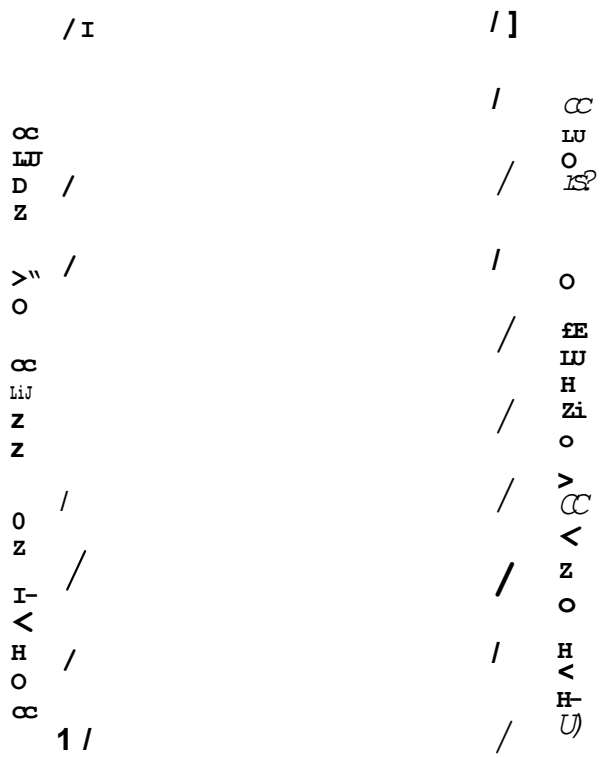

FIG.7 ; Diagram of Taylor Vortices

in a fluid filling the annular space

between relating cylinders.

in width with increasing probe rotation speed.

Taylor [31] predicted the onset of the instability for a small gap in terms of inner cylinder radius R_1, the gap between the cylinders b, angular velocity , and viscosity , in the form

$$T_a = \frac{R_1^{1/2} b^{2/3} \Omega_1}{\nu} \qquad (36)$$

which is named the Taylor Number.

In the case of a large gap it is convenient to form the Taylor Number, not in terms of the inner cylinder radius R, but in terms of the mean radius $Rm = \frac{1}{2}(R_1 + R_2)$. So the Taylor Number takes the form

$$\overline{T}_a = \frac{Rm^{1/2} b^{2/3} \Omega_1}{\nu} \qquad (37)$$

In addition to the vortices discovered by Taylor which arise when the laminar flow becomes unstable, Pai [34] observed vortices that are formed in turbulent conditions as a result of a secondary flow, at speeds which are several hundred times the critical speed. (Figure 8)

Recently E. H. Sparrow, W. D. Munro and V. K. Jonsson [35] investigated the instability of the flow for the wide gap situation between rotating cylinders. They produced critical Taylor Numbers for laminar instability covering a wide range of rotational speeds with different geometries.
They used the dimensionless term

$$T^* = \frac{R_2^4 \Omega_1^2}{\nu^2} \qquad (38)$$

as modified Taylor Number. In the present investigation the different modes of the flow have been considered as one of the effects governing the different surface patterns of erosion observed.

INNER CYLINDER WALL

Heat Transfer between Concentric Rotating Cylinders

The three types of flow we have seen in the previous section are the main controlling factors for heat transfer between rotating cylinders. The simplest problem involving a rotating cylinder is the rotating cylinder in an infinite and still environment, where heat is transferred away from the cylinder by free convection.

Many authors are agreed on the strong effect of free convection at low rotational speeds, in which laminar flow and heat transfer by conduction prevail. For example, Anderson and Saunders [36] and Dropkin and Carmi [37] have come to the similar conclusions, namely that at rotational Reynolds Number below about one thousand, heat transfer is virtually un-affected by rotation, but between 1,000 - 10,000 the rotational Reynolds Number is of importance.

W. M. Kays and I. S. Bjorkland [38] combined the effects of rotation, free convection and cross flow, and formulated the Nusselt Number by the equation

$$N_{Nu} = 0.135 \left[(0.5\, N^2_{Re} + N^2_{Re_s} + N_{Gr})\, N_{Pr} \right]^{1/3} \qquad (38.1)$$

for rotating Reynolds Numbers in the range 2,000 - 45,000.

When N_{Re_s} (cross flow Reynolds Number) and N_{Gr} (Grashof Number) are negligible compared to N^2_{Re} (rotating Reynolds Number) and for $N_{Pr} = 0.7$, Equation (38.1) above reduces to

$$N_{Nu} = 0.095\ N_{Re}^{2/3} \qquad (38.2)$$

At high speeds of rotation Edmund [39] and then Dropkin and Carmi [37] showed $Nu \propto Re^{7}$.

In a later paper Bjorklund and Kays [40] correlated their data for the case of the inner cylinder only rotating by the equation

$$N_{Nu} / N_{Nu\ cond} = 0.175\ N_{Ta}^{1/2} \qquad (38.3)$$

where N_{Nu} = Nusselts Number; $N_{Nu\ cond}$ = Nusselts Number for pure conduction.

For Taylor Numbers between 90 - 2,000, Carl Gazley [41] considered the convective heat-transfer charateristics of the flow in the annular gap between a rotating inner cylinder, and a stationary outer cylinder, using both smooth and slotted surfaces. His findings indicate that regular ring shaped vortices result in a heat-transfer rate that is even greater than that with turbulent flow.

Mass Transfer from Rotating Cylinders

Many workers have investigated mass transfer from cylinders rotating about their axis especially since the role played by mass transfer in a solid/liquid reaction can be ascertained by examining how its rate is affected by varying the speed of rotation of a cylinder of the solid reacting in the liquid. King [42] dissolved rotating cylinders in aqueous acid using baffles, and found a linear dependence of dissolution rate with rotational speed. Ward and Taylor [43] have studied the kinetics of the dissolution of a solid copper cylinder in liquid lead and bismuth alloy and showed an approximately linear power dependence.

Jackson and Grace [44] immersed a rotating zinc cylinder in bismuth allowing it to dissolve completely at constant speed so that the Reynolds Number decreased to zero during each experiment. The dissolution dependence was found to be nearly linear.

Roald and Beck [45] used rotating cylinders in a study of rates of dissolution of magnesium and its alloys in hydrochloric acid solutions and found that the rate of dissolution increased with the 0.71 power of the speed of rotation. Eisenberg, Tobias and Wilke [46] dissolved solid organic acids in different glycerol solutions. Using the rotor diameter as the characteristic length in the Reynolds Number they found a power dependence of 0.7.

Sherwood and Ryan [47] investigated heat mass and momentum transfer data from five different sources and showed that all the data is close to a 0.7 power dependence on Reynolds Number.

Olsson, Koump and Perzak [48] investigated the rate of dissolution of rotating iron and Fe - C alloy cylinders in graphite-saturated molten iron at temperatures below the melting point of the solid. They concluded that the rate of dissolution is controlled by mutual counter diffusion of carbon and iron in the boundary layer.

In their more recent work [49] they dipped rotating carbon cylinders in molten Fe - C and came to the conclusion

that the rate of dissolution of carbon in Fe - C alloys is controlled by the rate of carbon diffusion from the interface.

Both their investigations showed 0.7 power dependence on surface velocity.

Pehlke, Goodell and Dunlop [50] dissolved steel in molten pig iron and found that the rate of solution is a function of bath composition, temperature and stirring.

Lommel and Chalmers [51] looked at lead cylinders dissolving in lead tin alloys keeping $C_L - C_0 > 0.05$ gr. atoms (C_L being concentration of the dissolving species of Liquidus Line at a chosen temperature; Co - concentration of the dissolving species in the bulk liquid.) They discovered that dissolution was independent of rotation speed and thus concluded that the surface reaction was the controlling step.

In a more recent paper Ohno [52] studied the dissolution of iron cylinders in liquid Cu and Cu-Fe alloys at different speeds and temperature ranges. Their rate constant is found to vary with the 0.85 to the 0.96 power of the Reynolds Number, which suggested another diffusion controlled process.

3. Theoretical Treatment

3.1 Introduction

The theory may be conveniently divided into two sections. The first part is concerned mainly with the heat transfer phenomena and the second part with the dissolution process.

In the first section of the theory the dimensionless model of the integral profile method is given and the equations for cylindrical solidification are derived. These are basically applications of Hills integral profile method [10] to a different geometry by means of convenient modifications. The computer solutions for flat and cylindrical geometries describe the solidification and subsequent melt-back of a liquid metal in imperfect contact with a flat or cylindrical wall respectively.

In the second section of the theoretical treatment the different modes of dissolution are discussed and the equations for transport controlled dissolution are derived.

Dimensionless Model for a Growing Layer on a Plane Finite Wall

This model (Figure 9) has been extensively described by Hills [10] and Brooks [6] and is discussed in literature survey (page 19).

The resulting differential equations governing the change of chill-layer thickness, inside-layer temperature and wall temperature with time are expressed in dimensionless terms as

$$\frac{dt^*}{d\xi} = \frac{2\Lambda^*}{\Gamma^* + \sqrt{\Gamma^2 + 4\Lambda^*\Omega^*}} \tag{39}$$

$$\frac{d\theta_o^*}{d\xi} = -\frac{H^*\left(\frac{dt^*}{d\xi}\right)^2 + q_s^*\left(\frac{dt^*}{d\xi}\right) + t^* f_\xi'}{1 + t^* f_\theta' \theta^*} \tag{40}$$

$$\frac{d\theta_w^*}{d\xi} = \frac{\frac{3(\theta_o^* - \theta_w^*)}{\gamma_w^* R^*} + \left(R^* \left(\frac{dt^*}{d\xi}\right)\right) \Big/ k^*}{\frac{R^*}{k^*} + 3} \tag{41}$$

where $\Omega^* = H^* t^* (1 + t^* f_\theta^*)$ (42)

$$\Gamma^* = \sqrt{6H^* + 4(1-\theta_o^*) - 2t^* q_o^*}(1+t^* f_\theta^*) + q_s^* t^* (4 + t^* f_\theta^*) \tag{42.1}$$

$$\Lambda^* = 6(q_o^* - q_t^*)(1 + t^* f_\theta^*) - 3t^* \tag{43}$$

f_θ^* and f_ξ' being

$$f_\theta'^* = 3k^* / (R^* + 3k^*) \tag{44}$$

$$f_\xi'^* = -\frac{3k^*(\theta_o^* - \theta_w^*)}{\gamma^* R^* (R^* + 3k^*)} \tag{45}$$

Results obtained using these equations will be compared with those for the cylindrical case in section 6.1

* Dimensional symbols are described on page 192 .

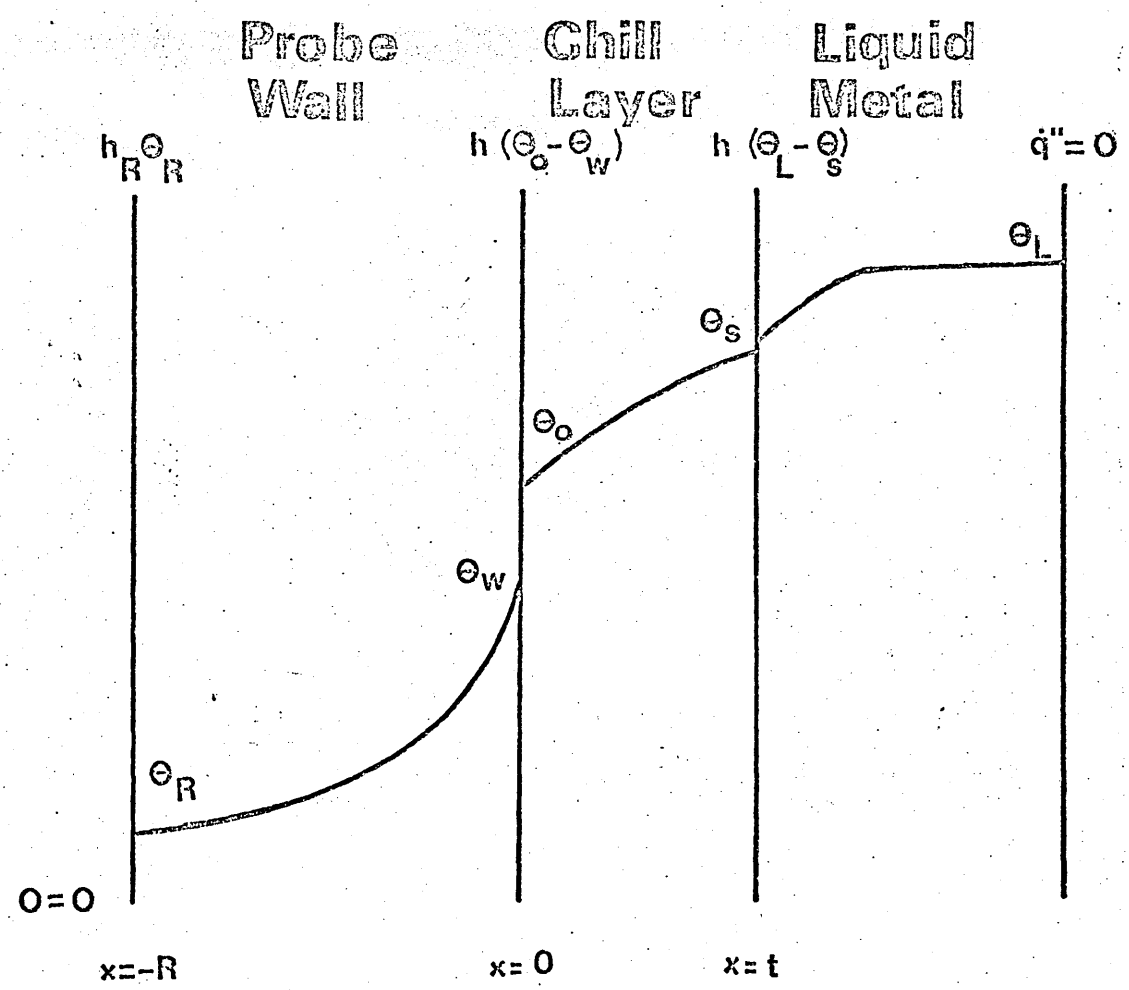

Figure 9

Heat transfer during growth of the chill-layer.

3.3 Application of Hills Integral Profile Method for Solidification on to the outside of a Cylindrical Probe

Figure 10

Heat transfer during growth of a chill-layer on a cylindrical probe.

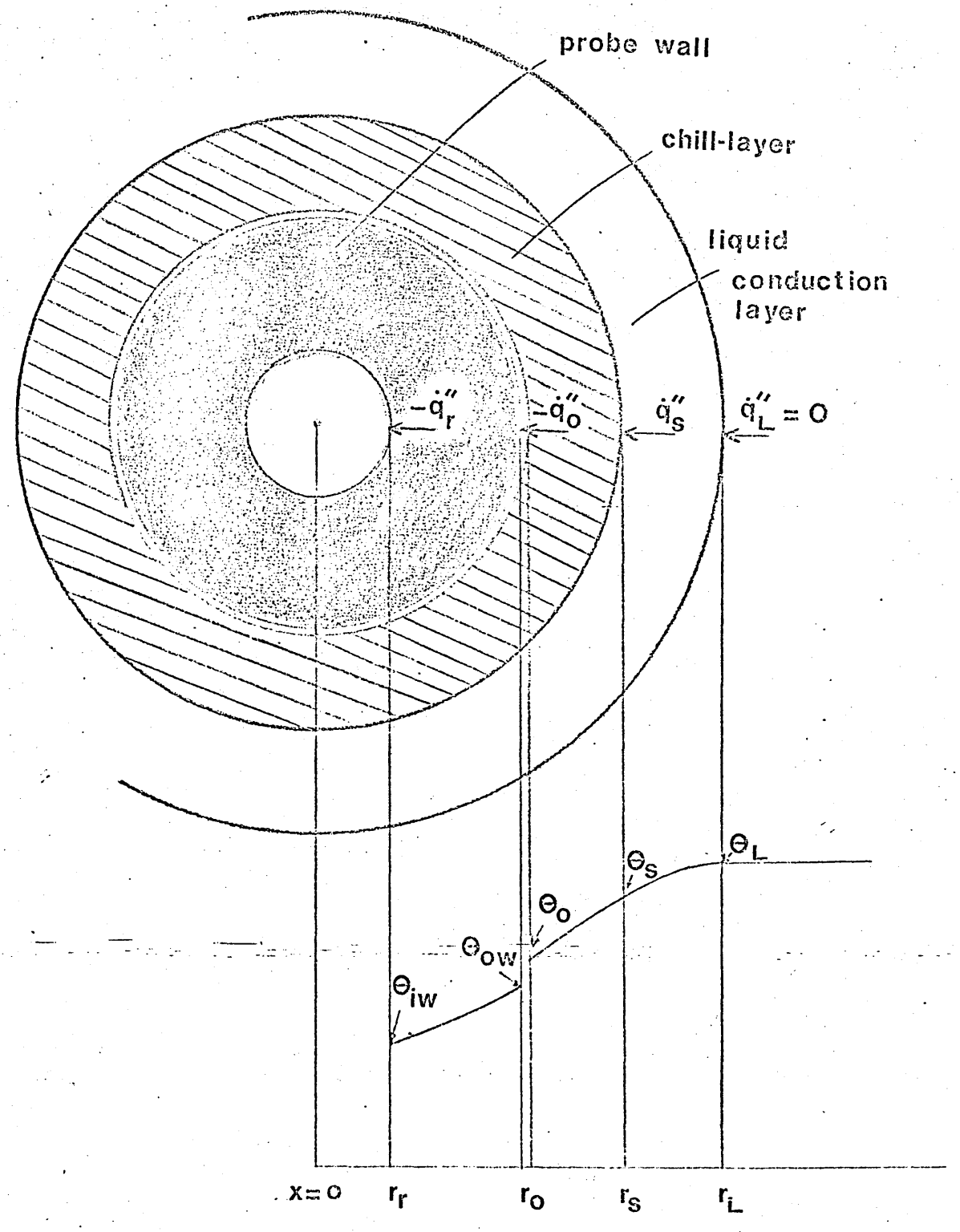

As shown in Figure 10 the cylindrical model can conveniently be divided into three zones: the probe wall, the chill-layer and the liquid conduction layer. Heat transfer in each of these zones is treated separately and a complete solution obtained by a combination of the three .

3.3.1 Heat Flow in the Chill-Layer

A cylindrical interface between solid and liquid metal is considered during solidification (Figure 10) and the unsteady state heat conduction equation is applied to the growing chill-layer. The Differential equation within the solidifying metal in cylindrical co-ordinates, is:

$$k\left(\frac{\delta^2\theta}{\delta r^2}+\frac{1}{r}\frac{\delta\theta}{\delta r}\right)=\rho c\frac{\delta\theta}{\delta\tau} \qquad (46)$$

Multiplying each side by r, integrating from r_o to r_s and applying the Leibnitz integral formula to the RHS gives:

(Leibnitz Theorem for differentiation: an integral with moving limits.

$$\frac{d}{dy}\int_a^b f(x,y)dx=\int_a^b\frac{df}{dy}dx+f(b,y)\frac{db}{dx}-f(a,y)\frac{da}{dx}\Bigg\}$$

$$\left[r\frac{\delta\theta}{\delta r}\right]_{r_o}^{r_s}-\left[\theta\right]_{r_o}^{r_s}+\left[\theta\right]_{r_o}^{r_s}=$$

$$=\frac{\rho c}{k}\left\{\frac{d}{d\tau}\int_{r_o}^{r_s}\theta\,r\,dr-\theta_s r_s\frac{dr_s}{d\tau}\right\} \qquad (47)$$

The first term of equation (47) is evaluated by considering the conservation of heat firstly at the solidification front, which gives

$$\left[r\frac{\delta\theta}{\delta r}\right]_{r_s}=r_s\frac{\rho H}{k}\frac{dr_s}{d\tau}-r_s\frac{\dot{q}''_s}{k} \qquad (48)$$

and then at the cooled inner surface of the solidifying metal, which gives

$$\left[r \frac{d\theta}{dr} \right]_{r_o} = - r_o \frac{\dot{q}_o''}{k} \qquad (49)$$

Substituting equations (48) and (49) into equation (47) and re-arranging gives

$$r_s(\rho H + \rho c \theta_s) \frac{dr_s}{\delta \tau} - \rho c \frac{d}{\delta \tau} \int_{r_o}^{r_s} \theta r dr = -(r_o \dot{q}_o'' - r_s \dot{q}_s'') \qquad (50)$$

An approximation to the integral of the heat content of the chill-layer is made by assuming the temperature profile to be linear

$$\theta = \frac{\theta_s(r_o - r) - \theta_o(r_s - r)}{(r_o - r_s)} \qquad (51)$$

This profile satisfies the conditions

$$r = r_s \qquad \theta = \theta_s$$

$$r = r_o \qquad \theta = \theta_o$$

Substituting (51) into (50) and re-arranging gives

$$\left[\rho H r_s + \frac{\rho c}{6} \left((r_o + 2r_s)(\theta_s - \theta_o) \right) \right] \frac{dr_s}{d\tau} - \frac{\rho c}{6} (r_s + 2r_o)(r_s - r_o) \frac{d\theta_o}{d\tau}$$

$$= - (r_o q_o'' - r_s q_s'') \qquad (52)$$

To get a solution for $\frac{dr_s}{d\tau}$ the term $\frac{d\theta_o}{d\tau}$ must be evaluated.

At the moving boundary

$$r = r_s : \theta = \theta_s = \text{constant so that } d\theta = 0$$

hence

$$d[\theta(r,\tau)] = \frac{\delta \theta}{\delta \tau} d\tau + \frac{\delta \theta}{\delta r} dr = 0 \qquad (53)$$

Thus

$$\frac{\delta \theta}{\delta \tau} = - \frac{\delta \theta}{\delta r} \cdot \frac{\delta r_s}{\delta \tau} \qquad (54)$$

The conservation of heat at the moving boundary $r = r_s$ gives:

$$\rho \frac{H \, dr_s}{d\tau} - \dot{q}_s'' = k \frac{\delta \theta}{\delta r} \qquad (55)$$

Substituting (55) into (54) gives

$$\left[\frac{\delta\theta}{\delta\tau}\right]_{r_s} = -\frac{1}{k}\left(\rho H \frac{dr_s}{d} - \dot{q}''_s\right)\frac{dr_s}{d\tau} \tag{56}$$

At the inner cooled surface we have

$$\left[\frac{\delta\theta}{\delta\tau}\right]_{r_o} = \frac{d\theta_o}{d\tau} \tag{57}$$

Assuming

$$\left[\frac{\delta\theta}{\delta\tau}\right]_{r} = \left[\frac{\delta\theta}{\delta\tau}\right]_{r_s} + b(r - r_s) \tag{58}$$

where $$b = \left[\frac{\delta}{\delta r}\left(\frac{\delta\theta}{\delta\tau}\right)\right]_{r_o} = \left[\frac{\delta^2\theta}{\delta r\,\delta\tau}\right]_{r_o} \tag{59}$$

but $$\frac{\delta\theta}{\delta r} = -\frac{\dot{q}''}{k}$$

and $$\frac{\delta^2\theta}{\delta\tau\,\delta r} = -\frac{1}{k}\frac{\delta\dot{q}''}{\delta\tau} = \frac{\delta^2\theta}{\delta r\,\delta\tau} \tag{60}$$

and at $r = r_o$

$$\left[\frac{\delta^2\theta}{\delta r\,\delta\tau}\right]_o = -\frac{1}{k}\frac{dq''_o}{d\tau} = b \tag{61}$$

substituting (61) into (58) gives

$$\left[\frac{\delta\theta}{\delta\tau}\right]_{r_o} = \left[\frac{\delta\theta}{\delta\tau}\right]_{r_s} - \frac{1}{k}\left(\frac{d\dot{q}''_o}{d\tau}\right)\left(r_o - r_s\right) \tag{62}$$

substituting from (57) and (56) gives

$$\frac{d\theta_o}{d\tau} = -\frac{\rho H}{k}\left(\frac{dr_s}{d\tau}\right)^2 + \frac{\dot{q}''_s}{k}\frac{dr_s}{d\tau} + \left(\frac{r_s - r_o}{k}\right)\frac{d\dot{q}''_o}{d\tau} \tag{63}$$

Providing $\dot{q}''_o = f(\theta_o, \tau)$

calling

$$\frac{\delta \dot{q}_o''}{\delta \tau} = f_\tau' \qquad \text{and} \qquad \frac{\delta \dot{q}_s''}{\delta \theta_o} = f_\theta'$$

then $$\frac{dq_o''}{d\tau} = f_\tau' + f_\theta' \frac{d\theta_o}{d\tau} \tag{64}$$

Substituting (64) into (63) and re-arranging will give

$$\frac{d\theta_o}{d\tau} = - \frac{\rho H \left(\frac{dr_s}{d\tau}\right)^2 - \dot{q}_s'' \left(\frac{dr_s}{d\tau}\right) - (r_s - r_o) f_\tau'}{k - (r_s - r_o) f_\theta'} \tag{65}$$

Substituting (65) into equation (52) gives

$$\Omega \left(\frac{dr_s}{d\tau}\right)^2 + \Gamma \left(\frac{dr_s}{d\tau}\right) - \Lambda = 0 \tag{66}$$

where $$\Omega = \rho^2 Hc\,(r_s + 2r_o)(r_s - r_o) \tag{67}$$

$$\Gamma = [k - (r_s - r_o) f_\theta'] [6 \rho H r_s + \rho c (r_o + 2r_s)(\theta_s - \theta_o)] - q_s'' \rho c (r_s + 2r_o)(r_s - r_o) \tag{68}$$

$$\Lambda = \rho c (r_s + 2r_o)(r_s - r_o)^2 f_\tau' - 6(r_o \dot{q}_o'' - r_s \dot{q}_s'') [k - (r_s - r_o) f_\theta'] \tag{69}$$

Since $\frac{dr_s}{d\tau}$ is positive whilst $- r_o q_o'' > - r_s q_s''$,

quadratic theory gives the solution of equation (66) as:

$$\frac{dr_s}{d\tau} = \frac{2\Lambda}{\Gamma + \sqrt{\Gamma^2 + 4\Lambda\Omega}} \tag{70}$$

Figure 11

Heat Flow in the

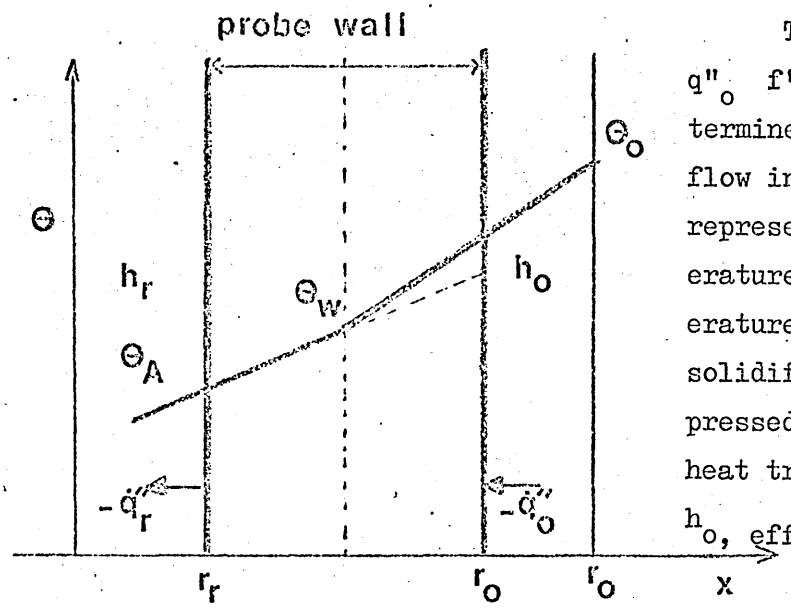

The forms of equation for q''_o f'_θ and f'_γ are to be determined by considering heat flow into the probe wall. If we represent the average wall temperature by Θ_w the midwall temperature, the heat flow from the solidifying metal can be expressed in terms of an effective heat transfer coefficient $h_{o,\,eff}$:

$$q''_o = - h_{o,eff} (\theta_o - \theta_w) \qquad (71)$$

and the heat flow from the probe wall to the cooling medium:

$$q''_r = - h_{r,eff} (\theta_w - \theta_A) \qquad (72)$$

where Θ_A is the temperature of the cooling medium . The two effective heat transfer coefficients are given by:

$$h_{o,eff} = \frac{1}{\frac{1}{h_o} + \frac{r_o - r_r}{2k_w}} \qquad (73)$$

$$h_{r,eff} = \frac{1}{\frac{1}{h_r} + \frac{r_o - r_r}{2k_w}} \qquad (74)$$

A heat balance on the probe wall is necessary to determine the mid-wall temperature.

Heat gained by unit length of wall in unit time

$$= - q''_o \cdot 2\pi r_o \qquad (75)$$

Heat loss by unit length of wall in unit time

$$= - q''_r \; 2\pi r_r \tag{76}$$

Heat stored in unit length of wall

$$= \pi (r_o^2 - r_r^2) \rho_w c_w \frac{d\theta_w}{d\tau} \tag{77}$$

Thus

$$\pi (r_o^2 - r_r^2) \rho_w c_w \frac{d\theta_w}{d\tau} = - 2\pi (r_o \dot{q}''_o - r_r \dot{q}''_r) \tag{78}$$

Substituting (71) and (72) in (78) and rearranging gives

$$\frac{d\theta_w}{d\tau} = 2 \frac{r_o h_{o,eff} (\theta_o - \theta_w) - r_r h_{r,eff} (\theta_w - \theta_A)}{(r_o^2 - r_r^2) \rho_w c_w} \tag{79}$$

Differentiating equation (71) with respect to time

$$\frac{d\dot{q}''_o}{d\tau} = - h_{o,eff} \left(\frac{d\theta_o}{d\tau} - \frac{d\theta_w}{d\tau} \right) \tag{80}$$

or,

$$\frac{dq''_o}{d\tau} = f'_\tau + f'_\theta \frac{d\theta_o}{d\tau} \tag{81}$$

where, obviously

$$f'_\theta = - h_{o,eff} \tag{82}$$

$$f'_\tau = + h_{o,eff} \frac{d\theta_w}{d\tau} \tag{83}$$

or substituting (71) into (83) we get

$$f'_\tau = 2h_{o,eff} \frac{r_o h_{o,eff} (\theta_o - \theta_w) - r_r h_{r,eff} (\theta_w - \theta_A)}{(r_o^2 - r_r^2) \rho_w c_w} \tag{84}$$

3.3.3. Heat Flow in the Liquid Metal

Brooks [6] work revealed the invalidity of treating the heat flow from a stirred liquid metal to a solid in terms of a boundary layer, of constant thickness having a constant heat transfer coefficient. The shape of his experimental curves of solidified thickness versus time for different amounts of superheat suggests that the heat flux is very high at the beginning, possibly due to unsteady state heat conduction. The need for a more flexible model led to the assumption that there is a conduction layer close to the solidification front whose thickness depends on time but also on the speed of rotation of the probe. This conduction layer lies between r_s and r_L as shown in Figure 10.

The thickness of this conduction layer was assumed to grow by unsteady state conduction during the early stages but then to be disturbed by the convection currents that develop as the bath of eutectic metal becomes stirred by the rotating probe. Once this happens the conduction layer is assumed to decay in thickness, approaching the thickness of the imaginary stationary film that is equivalent to the convective heat transfer coefficient at the surface of the probe.

The heat flux from the conduction layer can be represented by the heat conduction formula for heat conduction across unit length of a hollow cylinder:

$$\dot{q}' = -2r_s k \frac{d\theta}{dr} \pi = -\frac{2\pi k (\theta_L - \theta_s)}{\ln \frac{r_L}{r_s}} \qquad (85)$$

Expanding $\ln \frac{r_L}{r_s}$ and taking the first terms of the series as an approximation

$$\dot{q}' = - \frac{k\pi(r_L + r_s)(\theta_L - \theta_s)}{(r_L - r_s)} \qquad (86)$$

Dividing by $2\pi r_s$ gives:

$$\dot{q}''_s = - \frac{k(r_L + r_s)}{2r_s(r_L - r_s)} (\theta_L - \theta_s) \qquad (87)$$

This equation is used throughout the model to describe the flow of heat across the conduction layer to the solidification front. The variation of $\dot{q}''_s$ is developed by the substituting the varying values of r_s and r_L into this equation. The equations from which the values were determined are developed below. The growth of the conduction layer is assumed to occur by conduction only, so that the heat conduction equation within the layer is

$$k\left(\frac{\delta^2\theta}{\delta r^2} + \frac{1}{r}\frac{\delta\theta}{\delta r}\right) = \rho c \frac{\delta\theta}{\delta\tau} \qquad (88)$$

Providing $\left(\frac{d\theta}{dr}\right)_{r_L} = 0$, integrating equation (88) gives

$$-\frac{r_L + r_s}{2(r_L - r_s)} (\theta_L - \theta_s) = \frac{\rho.c}{k}\left(\frac{d}{d\tau}\int_{r_s}^{r_L}\theta r dr + \theta_s r_s \frac{dr_s}{d\tau} - \theta_L r_L \frac{dr_L}{d\tau}\right) \qquad (89)$$

Where the temperature gradient at the solidification front has been determined from equation (87) which gives:

$$r_s\left[\frac{d\theta}{dr}\right]_{r_s} = - \frac{(r_L + r_s)}{2(r_L - r_s)} (\theta_L - \theta_s) \qquad (90)$$

Assuming an effective temperature $\left(\frac{\theta_L + \theta_s}{2}\right)$ for the metal between r_s and r_L

$$\int_{r_s}^{r_L} \theta \cdot r dr = \frac{\theta_L + \theta_s}{2} \cdot \frac{r_L^2 - r_s^2}{2} \qquad (91)$$

and

$$\frac{d}{d\tau}\int_{r_s}^{r_L} \theta r dr = \frac{\theta_L + \theta_s}{2}\left(r_L \frac{dr_L}{d} - r_s \frac{dr_s}{d}\right) \qquad (91.1)$$

and $$\frac{d}{d\tau}\left(\int_{r_s}^{r_L}\theta r dr + \theta_s r_s \frac{dr_s}{d\tau} - \theta_L r_L \frac{dr_L}{d\tau}\right) =$$

$$= \theta_s r_s \frac{dr_s}{d\tau}\left(1 - \frac{1}{2}\right) \theta_L r_L \frac{dr_L}{d}\left(1 - \frac{1}{2}\right) + \frac{1}{2}\theta_s r_L \frac{dr_L}{d\tau} -$$

$$- \frac{1}{2} \theta_L r_s \frac{dr_s}{d\tau} \qquad (92)$$

re-arranging equation (92) and substituting in equation (89) gives the differential equation for the growth of conduction layer.

$$r_L \frac{dr_L}{d\tau} = \left(\frac{k_L}{\rho_L c_L}\left(\frac{r_L + r_s}{r_L - r_s}\right) - r_s \frac{dr_s}{d\tau}\right) \qquad (93)$$

Solidification does not start immediately the probe wall is exposed to the liquid metal in the case of superheat. A short time will elapse before the temperature of the liquid metal surface reaches the solidification temperature.

Thus some heat must be transferred to the probe wall before solidification starts so that θ_w will increase.

The thickness of the cooled liquid layer at the moment solidification starts is given by:

$$q''_o = - h_{o,eff}\,(\theta_s - \theta^s{}_w) = \frac{k(r^s{}_L + r_o)(\theta_L - \theta_s)}{2r_o(r^s{}_L - r_o)} \qquad (94)$$

where $r^s{}_L$ and $\theta^s{}_w$ are the values of r_L and θ_w just before solidification starts. The only unknown value in this equation is $\theta^s{}_w$ which can be determined from a heat balance between the cooled liquid layer and the heated probe wall:

Heat lost from the liquid metal

$$= \pi\left[(r_L{}^s)^2 - (r_o)^2\right] \frac{\theta_L - \theta_s}{2} \rho_L c_L \qquad (95)$$

Heat gained by wall

$$= \pi (r_o^2 - r_R^2)\, \theta_w \rho_w c_w \qquad (96)$$

from equations (95) and (96)

$$\theta_w^s = \frac{\rho_L \cdot c_L}{\rho_w \cdot c_w} \cdot \frac{(r_L^s)^2 - (r_o)^2}{2[(r_o^2 - r_R^2)]} \cdot (\theta_L - \theta_s) \qquad (97)$$

Putting (97) and (94) and re-arranging gives a cubic equation of r_L^s

$$A(r_L^s)^3 - Ar_o(r_L^s)^2 + (k - \theta - Ar_o^2)\, r_L^s + (k + \theta + r_o^2 A) r_o = 0 \qquad (98)$$

This equation can be solved for r_L^s using Newton - Raphson method.

Once this equation is solved, the value of r_L^s that has been determined is the value at which solidification starts and which could also be used to evaluate θ_w^s in equation (97)

The time τ_s when solidification starts can be determined by integrating equation (93) between r_o and r_L^s.

Considering $r_s = r_o$ and $\frac{dr_s}{d\tau} = 0$ before solidification starts equation (93) becomes

$$r_L \frac{dr_L}{d\tau} = \frac{k_L}{\rho_L C_L} \cdot \frac{r_L + r_o}{r_L - r_o} \qquad (99)$$

re-arranging and integrating the time dependent term between 0 and τ_s:

$$\tau_s = \frac{\rho_L C_L}{2k_L} (r_L^s - r_o)(r_L^s - 3r_o) + 4r_o^2 \ln\left(\frac{r_L^s + r_o}{2r_o}\right) \qquad (100)$$

The main differential equations, number (65), (70), (79) and (93), can be solved simultaneously as soon as solidifying starts.

3.3.3.1 The decay of the Conduction layer

Once the convection currents are fully built up in the liquid metal, the heat transfer to the solidification front is given by:

$$\dot{q}''_s = h_{LIQ} (\theta_L - \theta_s) \qquad (101)$$

where h_{LIQ} is the heat transfer coefficient from the liquid to the probe.

The effective stationary layer thickness t_{LIM} is very small so that the effect of the curvature of the cylindrical probe can have only a negligible effect. Thus we can write:

$$q''_s = \frac{k_L}{t_{LIM}} (\theta_L - \theta_s) \qquad (101.1)$$

so that

$$t_{LIM} = \frac{k_L}{h_{LIQ}} \qquad (101.2)$$

The substitution of the limiting value of $r_L = r_s + t_{LIM}$ into equation (87) will produce a value of $\dot{q}''_s$ almost identical to that given by equation (101).

Thus we have a situation during the early stages of solidification in which the outer radius of the conduction layer, r_L grows as given by equation (93) and then decays to a limiting value given by:

$$r_{LIM} = r_s + t_{LIM} \qquad (102)$$

An exact treatment for the decay of the conduction layer as the convection currents are established is extremely complicated, and certainly beyond the scope of the present treatment. The simplest approach to the decay is to represent it in terms of an exponential decay equation:

$$\frac{dr_L}{d\tau} = -\frac{Ln0.5}{\tau_{\frac{1}{2}}} \quad (r_L - r_s - t_{LIM}) \qquad (103)$$

where $\tau_{\frac{1}{2}}$ represents the half life of the decay process.

Equation (106) is used to describe the decay of the conduction layer after a certain time τ_c, prior to which its growth was assumed to be given by equation (94). After τ_c then, the growth and melt back of the solidified layer is given by solving equations (65), (70), (79) and (103).

For a probe rotating at 60 r.p.m., in lead/tin eutectic the following values have been used:

τ_c = 5 secs.

$\tau_{1/2}$= 6 secs.

h_{LIQ}= 8500 W/m^2 °C.

The theoretical lines plotted in Result section have been determined using this model.

Other values have been used in determining theoretical lines related to probes rotating at different speeds, and in different media. These values are given in Table 19in Appendix 5 which lists all the values used in computing the results presented in the thesis.

The choice of the values of the parameters, and the validity of the model are discussed in Section 7.2.

3.3.4 Numerical Methods of Solution and Computer Programme

The differential equations developed in Chapter3.3. and be solved numerically using a Runge-Kutta method of integration.

Two different computer programmes are written concerning planar and cylindrical models.

They both consist of a main programme and three subroutines written in Fortran IV assembly language.

The relationship between the main programme and the subroutines with respect to both cases are shown in Figure 12

The main programme and subroutine Difre related to the cylindrical case were developed in the present investigation.

The two other subroutines, Rukut and Step 4 were developed by Hills (Hills A. W.D.[54] Ph.D Thesis, University of London, 1966)

The main programme reads the data and calculates the initial values necessary for the start of integration as well as the corresponding time. All these calculated values are then written and Subroutine Rukut is called. This subroutine then calls subroutine step 4, the subroutine in which the numerical integrations are carried out. Rukut controls the integration by varying the step length used in step 4.

The original step length and print intervals are read from the main programme to which the values of the parameters are returned after integration and written at more or less constant print intervals. Subroutine step 4 calls subroutine Difre in which the actual values of the differentials are calculated.

The computation is carried out for each experimental system first at zero superheat in conjunction with flat and cylindrical models. Then it is repeated this time concerning only the cylindrical model, at superheats used experimentally, for different liquid heat transfer coefficients and halflife times of conduction layer until melt back is produced at times comparable to the experiments.

FIG 12

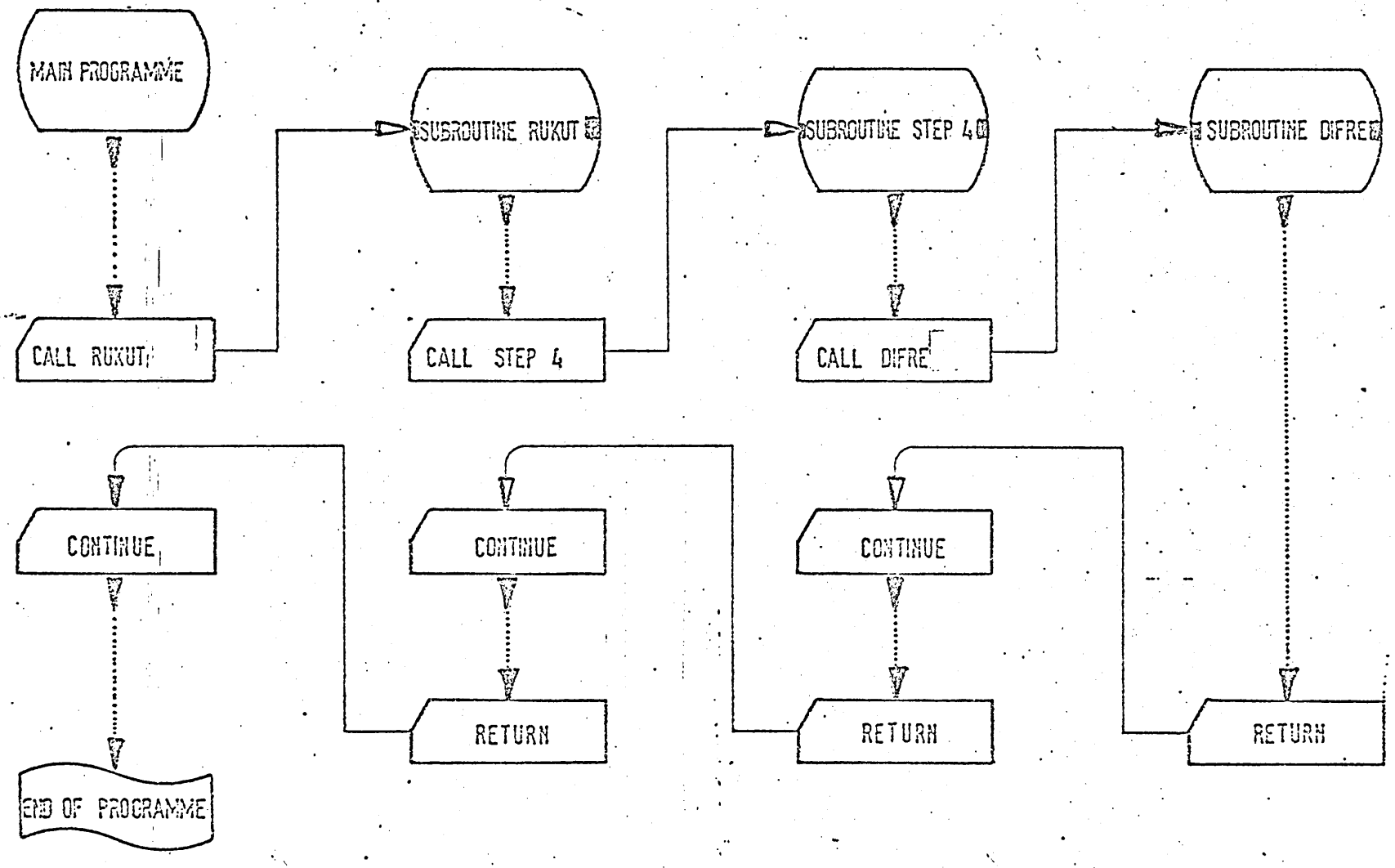

THE RELATIONSHIP BETWEEN THE MAIN PROGRAMME AND THE SUBROUTINES

3.4 Mass Transfer - Dissolution Process

3.4.1 The Nature and Kinetics of the Dissolution Process

The dissolution of a crystalline solid in a liquid involves a dissolution step at the solid-solid interface, in which the atoms, ions or molecules of the solid leave their positions in the lattice and enter the liquid phase, and a transport step in which the dissolved solid species is transported into the bulk of the liquid phase. The relative ease with which these two steps occur will vary from system to system. If the transport step occurs very much more easily than the dissolution step, the latter will control the rate of dissolution and the dissolution process is said to be interface controlled. If the dissolution step occurs the more readily, the rate of dissolution will be determined by the transport step and the dissolution process is said to be transport controlled.

In situations where there is little to choose between the relative ease of the two processes, they will both contribute to controlling the rate of dissolution, a situation known as mixed control.

In addition of course heat will have to be transported to or from the solid/liquid interface because the dissolution step will involve an exothermic or endothermic heat effect.

It is thus possible that heat transfer may exert some controlling influence on the rate of the reaction although instances where this occurs are relatively rare.

The next section of the work derives an equation for the rate of dissolution, assuming it to be mass transfer controlled. Equations have not been presented for interface control since, as will be seen later the dissolution processes studied in this work were found to be mass transfer controlled.

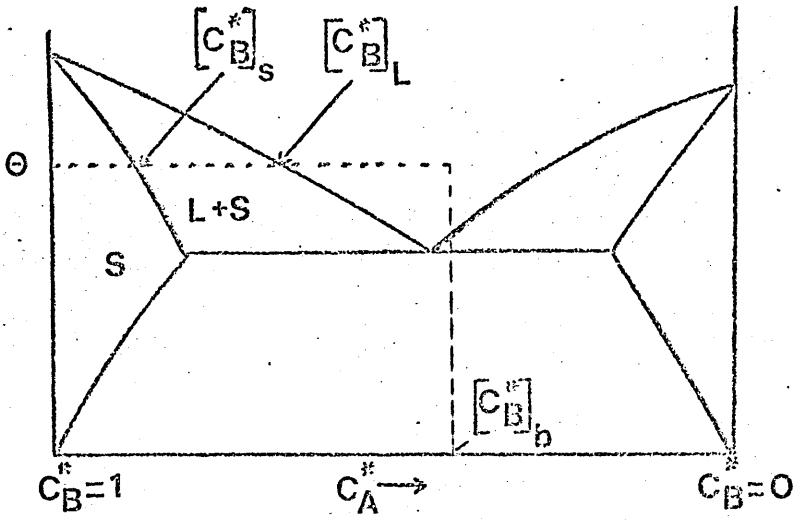

Figure 13 Typical phase diagram for a Binary alloy system A/B involving two solid solutions

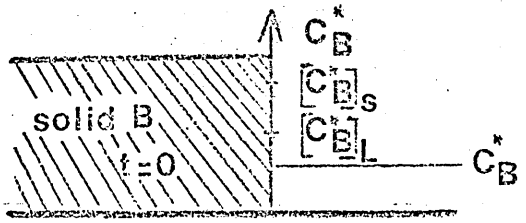

(a) Initial conditions

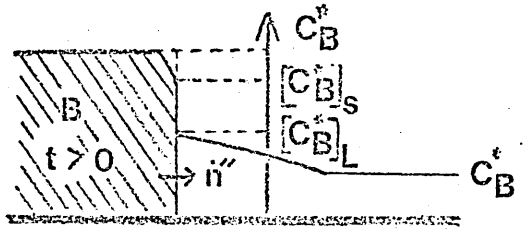

(b) Transport in static liquid

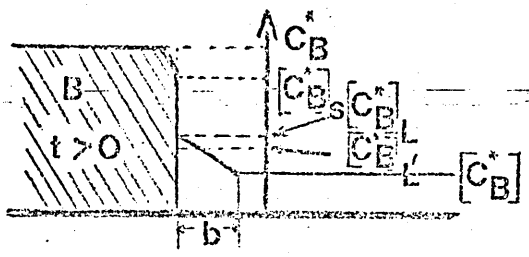

(c) Transport in a stirred liquid

Figure 14 Boundary conditions for transport in a liquid with moving boundaries.

Figure 14(a) represents the concentration gradients that exist before dissolution starts, and Figure 14(b) when solid B is dissolving in liquid A. The concentration terms used on both these Figures has been demonstrated in Figure 13 on a simple eutectic system with limited solubility. The mass flux of B away from the surface is also shown on the Figure 14(b). It is transported by diffusion and by the convective motion of the liquid phase stirred by natural or forced convection. Since species B can be present in high concentrations in the liquid, analysis of this convection process is somewhat difficult to carry out. The following simplified approach, however, provides a result of sufficient accuracy.

The simplified approach is illustrated in Figure 14(c) in which the convective boundary layer in Figure 14(b) is replaced by an affective stationary layer of thickness b, b being smaller than the thickness of actual convective boundary layer. Species B is transported across the effective stationary layer merely by diffusion and by the bulk motion brought about by the transport of B itself. Thus we can write:

$$n''_B = - D_{AB} C_T \frac{dC^*_B}{dx} + C^*_B n''_B \qquad (104)$$

where

C^* = mass fraction of metal B in a binary alloy of metals A and B

C_T = mass density of alloy

$D_{A/B}$ = binary diffusion coefficient in the liquid alloy A/B at low concentrations of B

n''_B = mass transfer flux of B

$(\ )_i$ = value at solidification interface

$(\ )_b$ = value in bulk liquid phase.

Equation (104) ignores the fact that the solid/liquid interface recedes as dissolution takes place. The effect, however, is quite small and can be ignored without introducing a significant error.

Equation (104) can be re-arranged:

$$n''_B (1 - C^*_B) = - D_{AB} C_T \frac{dC_B}{dx} \tag{105}$$

whence

$$\int_{(C^*_B)_i}^{(C^*_B)_b} \frac{dC^*_B}{(1-C^*_B)} = - \frac{n''_B}{d_{AB}C_T} \int_0^b dx \tag{106}$$

$$\ln \left(\frac{1 - (C^*_B)_b}{1 - (C^*_B)_i} \right) = \frac{\dot{n}''_B b}{D_{AB}C_T} \tag{107}$$

so that

$$\dot{n}''_B = \frac{D_{AB}C_T}{b} \ln \left\{ \frac{(C_A^*)_b}{(C^*_A)_i} \right\} \tag{108}$$

since the liquid phase contains only A and B. Equation (108) can be re-arranged in the form:

$$\dot{n}''_B = \frac{D_{AB}C_T}{b} \left| (C^*_B)_i - (C^*_B)_b \right| x \frac{\ln \left(\frac{(C^*_A)_b}{(C_A^*)_i} \right)}{(C^*_A)_b - (C_A^*)_i} \tag{109}$$

$$\text{since } (C^*_B)_i - (C^*_B)_b = (C_A^*)_b - (C_A^*)_i \tag{110}$$

Equation (109) can be represented in a simpler form by defining the log mean mass fraction of A:

$$(C_A^*)_{ln} = \frac{(C_A^*)_b - (C_A^*)_i}{\ln \left(\frac{(C_A^*)_b}{(C_A^*)_i} \right)} \tag{111}$$

so that

$$n''_B = \frac{D_{AB} C_T}{b(C_A^*)_{ln}} \left| (C_B^*)_i - (C_B^*)_b \right| \tag{112}$$

The value of b can be determined from the limiting

mass transfer situation - that is mass transfer that occurs when the transferred species is present at very low mass fractions. For such situations it is possible to write:

$$(n''_B)_{lim} = C_T \alpha^o_{AB} \left[(C_B^*)_{i,\,lim} - (C_B^*)_{b,lim}\right] \qquad (113)$$

where α^o_{AB} is the limiting mass transfer coefficient, and is a function of the stirring conditions only. Furthermore, since $C_B^* \longrightarrow 0$; $C_A^* \longrightarrow 1$

and

$$(C_A^*)_{Ln} = 1 \qquad (114)$$

so that comparison of equation (113) and equation (112) written for limiting mass transfer conditions, gives:

$$\alpha^o_{AB} = \frac{D_{AB}}{\delta} \qquad (115)$$

For non-limiting conditions, then, equation (112) becomes

$$n''_B = \frac{\alpha^o_{AB}\, C_T}{(C_A^*)_{ln}} \left[(C^*_B)_i - (C^*_B)_b\right] \qquad (116)$$

Equation (116) controls the rate at which the dissolving species B is removed from the solid/liquid interface. If the dissolution process is transport controlled, $(C_B^*)_i$, will be determined by equilibrium conditions at the solid/liquid interface. For example, consider a situation in which pure metal B is dissolving in a liquid A/B alloy, Figure 13 showing a binary alloy phase diagram.

$(C_B^*)_b$ is the composition of the bulk liquid alloy, and Θ, is taken as the temperature at which the dissolution process is taking place, $(C_B^*)_S$ and $(C_B^*)_L$ being respectively, the solidus and liquidus alloy compositions at that temperature.

If the dissolution step at the solid/liquid interface is not rate controlling, equilibrium will exist at the interface. This means that the liquid alloy at the interface will

contain $(C_B^*)_L$ of B and that the surface layers of the solid metal B will contain sufficient A in solid solution for the composition of the solid surface to be $(C_B^*)_S$. These layers will be continually dissolving so that this A does not leave sufficient time to diffuse into the bulk of the solid.

Under these conditions, then, the liquid composition at the interface is given by the liquidus line, and equation (116) becomes:

$$n_B'' = \frac{\mathcal{D}^o_{AB} \, C_T}{(C_A^*)_{Ln}} \left\{ (C_B^*)_L - (C_B^*)_b \right\} \qquad (117)$$

This equation will be used later to analyse transport controlled dissolution rates.

4.1 The Apparatus

The apparatus is similar to that originally designed by Brooks. It consists of three independantly mobile sections (Figure 15). A photograph of the apparatus is shown on Plate 1.

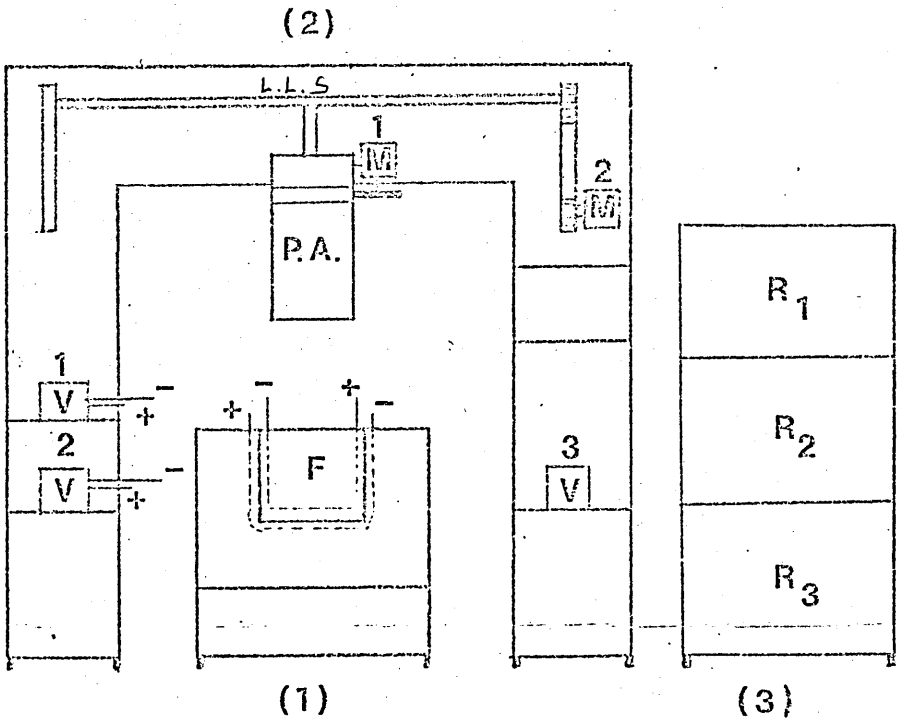

Figure 15 The Apparatus

1 The furnace
2 The probe assembly P.A.)
Control panel (C.P)
Lifting and lowering system (L.L.S)
Variacs (V) and Motors (M)
3 The Recorders (R)

4.1.1 The Furnace

The furnace consists of a large austenitic stainless steel crucible which is powered externally by a 2 kW thermocord heater and internally by a 1 kW insulated, stainless sheathed heating coil. (Figure 16)

Both of the heaters are controlled by means of Variacs [V_1 and V_2 in Figure (15)]

Heat losses are minimized by 100 mm of vermiculite insulation.

The alloy is melted and remelted inside the crucible which has a tilting mechanism to pour out the molten metal if required.

The bulk liquid metal temperature is measured by a stainless steel sheathed chromel/alumel thermocouple.

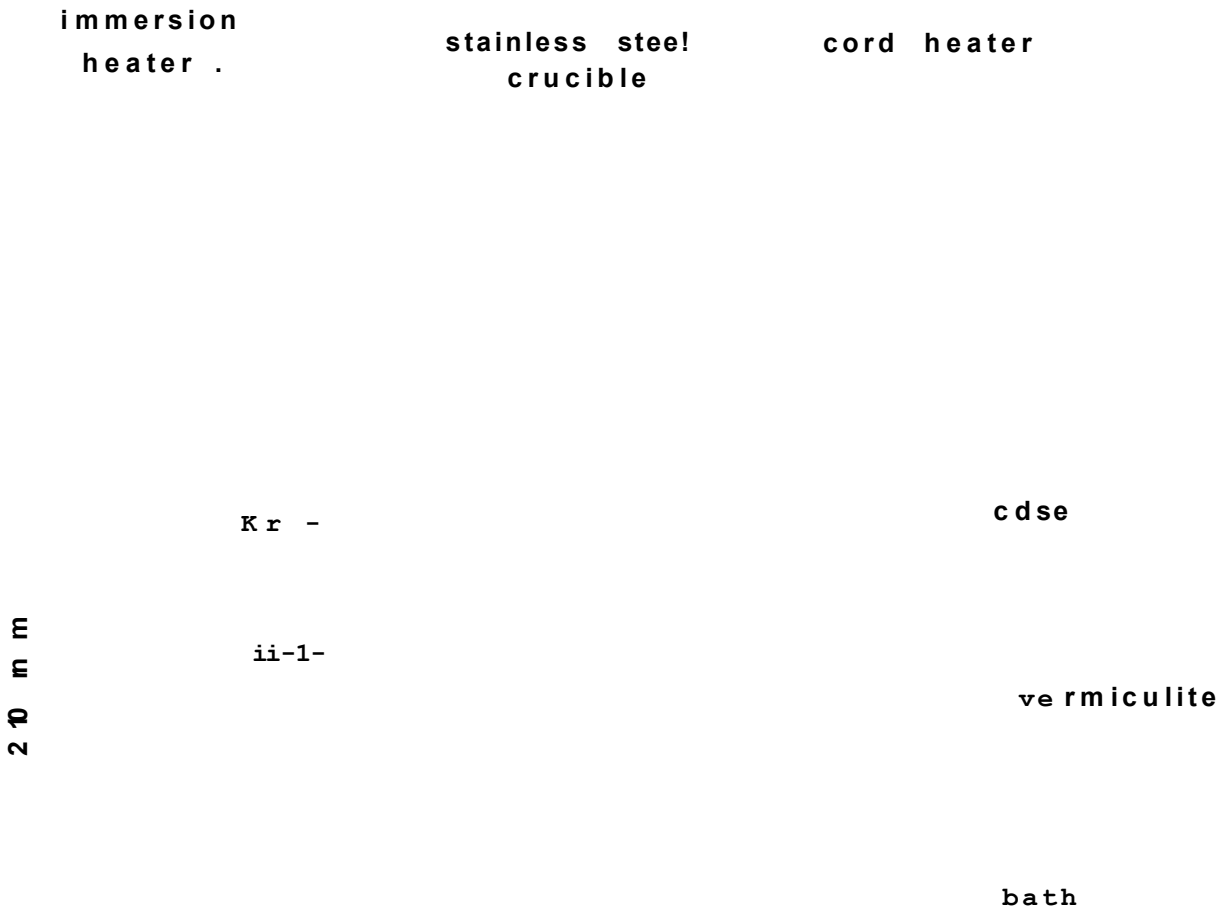

Figure 16

The Furnace

4.1.2 The Probe Assembly and the Rotating Mechanism

The probe assembly (P.A) is supported by a frame which enables the cylindrical probes to be lowered into or raised from the liquid bath at a constant speed by means of an A.C.Motor (M2) (Figure 15, Plate 1)

The travel is limited at its upper and lower positions by micro switches.

Another A.C.Motor (M1) which is attached to the probe assembly and controlled by the Variac V_3 enables the probe to be rotated at chosen speeds within the range 0 - 180 r.p.m. The rotation mechanism used permits continuous, vibration-free rotation of the probe with continuous monitoring of up to three thermocouple outputs from the probe.

The mechanism (Figure 17, Plate 2a) originally constructed by Brooks (unpublished paper) is supported on a central stator (d) by the ball race (a), and driven by a friction wheel pressed against the mechanism at (g), the side thrust being resisted by the ball race (b).

Six copper slip-rings (c) are bonded with araldite to an ebonite sleeve attached to the stator. The contact brushes (e) are cold rolled Cu-Be strips mounted on a Tufnel block (f) attached to the rotating probe assembly. This block also acts as the terminal strip for the thermocouple leads from the Probe to the recorders. The cylindrical, hollow probe is suspended from the rotor by three threaded rods which screw into threaded tubes, integrally cast into the probe wall (Section 4.1.3). Cooling air can be supplied to the inside wall of the probe by a 2.54 cm diameter pipe (i) attached to the stator and positioned concentrically inside the probe.

PLATE 1

The apparatus

P L A T E 1

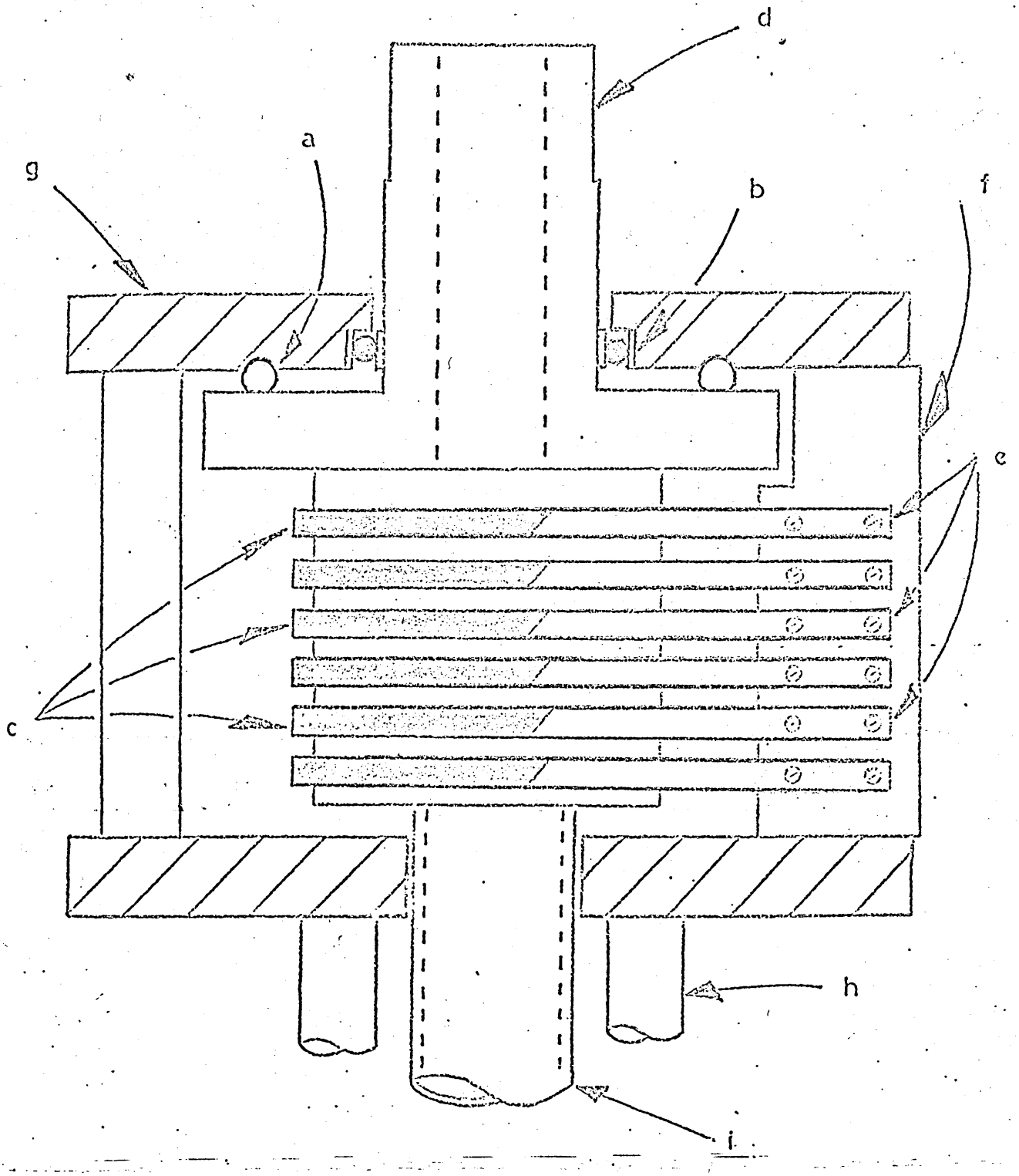

FIGURE 17

Section of Rotating Probe Support with Slipring s.

PLATE 2

A close up to the rotation mechanism

A probe just after a chill-layer experiment

PLATE 2

4.1.3 The Control Panel and the Recorders

A close-up of the control panel can be seen on Plate 3.

The control panel contains an emergency switch-off system as well as independent switches for operation of the variacs, lifting and lowering system and the rotation mechanism. Heater currents are displayed on the two ammeters.

The thermocouples are connected to the recorders via the panel.

One speedomax type recorder with ranges 0 2, 5, 10, 25, 50 and 100 m.v and two Honeywell Elektronik 15 type recorders with ranges 0 10, 100 m.v are used to monitor the outputs of the thermocouples cast into the probe wall.

A push button on the control panel operates the battery powered 'event marker' which, by injecting a D.C. pulse into the recorder inputs, enables the exact moment that the probe enters or leaves the bath to be marked on the recorder charts.

PLATE 3

The control panel of the apparatus

PLATE 3

4.2 The cylindrical probes

Figure 18 shows a section through the hollow probes used in this work. The probes were produced by casting as described in the next sections. They were supported from the rotor mechanism by three rods that were screwed into three internal threaded tubes that were cast into the top of the probe wall. Three thermocouples were cast in to the wall of the probe as shown in the figure so that the temperatures of the inner and outer surfaces of the probe wall could be continuously measured during the experiments. Probes we manufactured were of commercially pure lead, commercially pure tin and three lead tin alloys, containing 10% tin, and 80% tin and 90% tin.

Figure 18

SECTION OF LEAD PROBE

4.2.1 Pre-casting Preparations

A cylindrical steel mould for casting the hollow cylindrical probes was prepared in two halves [(a) and (b)] by machining from a solid bar of mild steel.

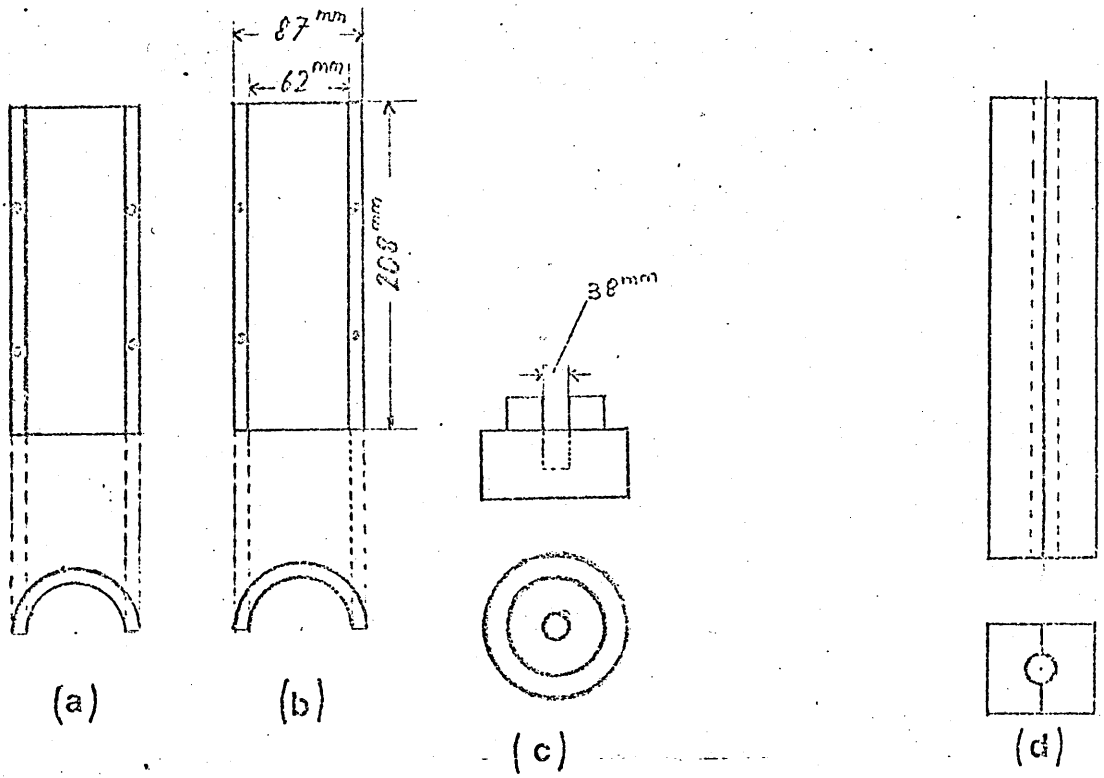

Figure 19 (a), (b) and (c):
Parts of the steel mould.
(d) wooden core-box
(e) sand core

A bottom piece (Figure19c) fits tightly to the main body to complete the mould. (Plate 4, 3.) The hole in the bottom section enables a sand-core to be centred in the mould to provide cylindrical cavity in the probe. (Plate 4 a, b.)

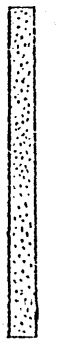

The sand-cores were prepared in a wooden core-box (Figure 19d, plate 4a) from Windsor-Rose sand using the CO_2 process.

PLATE 4

(a) Precasting arrangements showing sandcore as prepared in a wood-core-box, three steel connection rods and the stainless steel mould

(b) The above shown items put together ready for casting

4.2.2 Casting of the Probes

Three hollow steel rods threaded on both surfaces are positioned at 120° angles in the top of the mould. After casting, these enable the probe to be attached to the rotor assembly by means of threaded rods of smaller diameter. (Plates 2 and 4).

Three chromel-alumel thermocouples are carefully positioned inside the mould for measuring inside and outside wall-temperatures over the main reading section during the experiments. The core, (Section 4.2.1, Figure 19d) the thermocouples and the rods are held stationary by means of clamps whilst the probe is cast.

The closed bottom part of the probe is cast into position after the probe is removed from the mould.

A longitudinal section through a lead probe is shown diagramatically in Figure (18).

The stainless steel mould extracted heat very rapidly from the solidifying probe metal, ensuring that it solidified in a radial direction. A high degree of directional solidification was thus achieved in the production of all the probes, as can be seen from the micrographs of probe material shown in Plates 18, 20, 21, 22, 24 and 25.

EXPERIMENTAL PROCEDURE

All the experiments concerning heat and mass transfer were carried out on the apparatus described in the previous section.

The main object of these experiments was to provide sufficient data to test the theoretical developments and to give useful information to advance some parts of the theory.

5.1 Experimental sequence

5.1.1 Chill Layer Experiments

These experiments were carried out to determine:

1 the rate of growth and meltback of the chill-layer on a cylindrical substrate;

2 the change of the inside and outside surface temperatures of the probe wall with time.

Each chill layer experiment began by melting the alloy in the bath and preheating it to about 4 - 5°C. above the selected temperature. Then, with zero power input the melt would start to cool at about 1.8°C. per minute.

In the meantime the probe was screwed to the probe assembly by means of the steel rods and the thermocouple leads connected to the terminal block on the rotating assembly.

Prior to each experiment the bath had to be stirred by a hand-held, motorized, rotary stirrer because of the large difference in density of the two component metals. When the bath temperature had fallen to within $\frac{1}{2}^{\circ}$ to 1° of the chosen temperature the stirrer was taken out of the bath, dross was removed from the surface of the melt and rotation of the probe commenced. (Failure to remove dross from the surface of the melt gave rise to an uneven probe surface.) The rotation speed was measured by a hand hold tachometer. During all the chill layer experiments the rotation speed was kept at 60 r.p.m.

Each experiment was started by lowering the ro-rotating probe into the bath. The event marker was operated just as the probe touched the bath surface, (and again just as it cleared the bath surface on withdrawal.)

During the period while the probe was in the melt the bath temperature and the probe wall temperature were monitored continuously. A stop watch was used to measure the time of immersion.

5.1.1.1 Zero bath superheat

Before every experiment with zero bath superheat, the bath temperature was brought just above its melting point.

The first probe was lowered with zero power output of the heaters into the bath and removed immediately so as to obtain the minimum possible time of exposure. This gave about 6 seconds of exposure to the bottom end of the probe, (the probe moved at about 4 cm/sec. the length exposed was about 12 cm.) The exposure time was then gradually increased for each set of experiments (in 3 - 6 second intervals), so that the thickness of the growing chill-layer on the probe could be measured as a function of the time of immersion. This measurement was made when the probe had cooled using a micrometer at various circumferential positions. The measurements were made in a 4 cm wide region starting 4 cm above the bottom end of the probe, (i.e. mostly 4 cm. below the melt surface) as this was found to be a suitable region in which to take a mean reading to give the thicknesses of the chill-layer at a specific time. (Figure 20)

As Fig. 20 and Plate 6 show, erroneously enhanced thicknesses of solid metal formed close to the bath surface and close to the bottom plug. These were due to the effect of heat flow upwards along the probe wall from the bath surface, and into the bottom plug of the probe. Three separate dips were made for each

Prob:

main, reading
area (4 cm)

4 cm

CHILL-LAYER

Fig. 20

MAIN READiNG AREA

chosen exposure time and at least nine different measurements were made of the chill-layer thickness for each such dip. Chill-layer experiments for zero superheat were discontinued once the layer was found to have stopped growing.

5.1.1.2 Superheated baths

Another series of experiments was carried out with the bath at various degrees of superheat, cylindrical rotating lead probes again being immersed in the eutectic lead-tin melt.

The time for which the rotating probe remained in the melt was progressively increased in separate experiments until it could be removed with a relatively clean lead surface on which no chill-layer remained within the area designated in Section 5.1.1.1 as the area within which measurements were made.

Thickness readings were taken in a similar way to those at zero superheat.

5.1.2 Dissolution experiments

These experiments were carried out to determine the mechanism controlling the rate of dissolution by investigating possible relationships between the rate of dissolution and :

1 the rotation speed of the probe,
2 the experimental temperature
3 the orientation dependence of the dissolution process. The probes for the dissolution experiments were identical to those used in the chill-layer experiments except that they contained no thermocouple.

Immediately before the experiments, the probes were machined (Plate 9). To remove the thin oxide films films that readily form even at room temperatures, the lowest possible machining speed was chosen to avoid as far as possible recrystallisation of the probe material.

Prior to each experiment the probes were weighed and the experiments were started by dipping the probes into the melt. After the relevant chill-layer melt back time had been exceeded the probe was held in the bath for a pre-selected period of time after which it was weighed again to determine the amount of metal dissolved. Experiments were carried out for a range of steadily increasing dissolution times. Selected probes were also prepared for a macro-structural examination.

These experiments were repeated for pure lead, pure tin and for some of their alloys at different rotation speeds, different concentration driving forces and different temperatures. (See Table 9). After each experiment the melt was brought back to the eutectic composition by adding the necessary amounts of the metal. After every 5 experiments the bath composition was chemically analysed for Pb and Sn.

5.1.3 Preparation of Micro and Macro Structures

5.1.3.1 Pb - Sn in their pure form

To investigate the attack of liquid on the solid probes as well as the possible orientation dependence of this attack, samples were cut from some of the dissolved probes so that sections could be prepared through the surface layers.

Special attention was given to the preparation of the samples from the pure lead and tin probes since these materials can be easily deformed. Such deformation usually leads to immediate recrystallisation which changes the structure of the materials under investigations. The procedure adopted in this work is as follows.

The samples were cut out of those probes by a band saw at the lowest possible speed.

After the samples had been mounted in cold setting

Metset 'FT' resin, they were hand-ground wet on the following series of waterproof polishing papers for the indicated periods of time:

(i) number: 120, 220 320 (about 20 minutes each)
(ii) 400 (30 minutes) and
(iii) 600 (60 minutes).

The specimens were then polished on a wheel covered with napped wool cloth impregnated with 4 - 8 diamond paste and rotating at around 40 - 60 r.p.m. until most of the scratches had dissappeared and the surface of the specimens had become bright. (6 - 8 hours.) The same operation was then carried out using No. 0 - 7 diamond paste.

During the course of the fine polishing the lead and tin samples were etched several times. The samples of all metals were then finally etched to develop their microstructures. For the etching of lead two different solutions were tried:

1 Normal Vilella's etching medium (3 minutes)
16 cm^3 Nitric acid (1.40)
16 cm^3 Glacial acetic acid
68 cm^3 Glycerol

2 20 cm^3 nitric acid (1.40) (10 minutes)
80 cm^3 distilled water

The second solution produced the best results, and all the micro- and macro-sections illustrated in the thesis have been prepared with this etchant. For the etching of pure tin the following solution was used:

2 cm^3 HCl
10g Ferric chloride
95 cm^3 Distilled water
3 cm^3 Alcohol

5.1.3.2 Pb - Sn Alloys

The bath material, as cooled in the air, and the growing chill layer of the same composition were sectioned for micro-structural observation. (Plates 5, 7, 8) The preparation of these micro-structures was not as difficult as for the pure metals. The method of preparation used is as indicated on the relevant plates.

PLATE 5

Pb-Sn eutectic(bath)cooled in air

Etchant: Acetic acid; Nitric acid; Glycerol = 1:1:4

Magnification: x 40

r>LATE 5

PLATE 6

Chill-layer grown on a Pb-probe under unstirred conditions.

PLATE 6

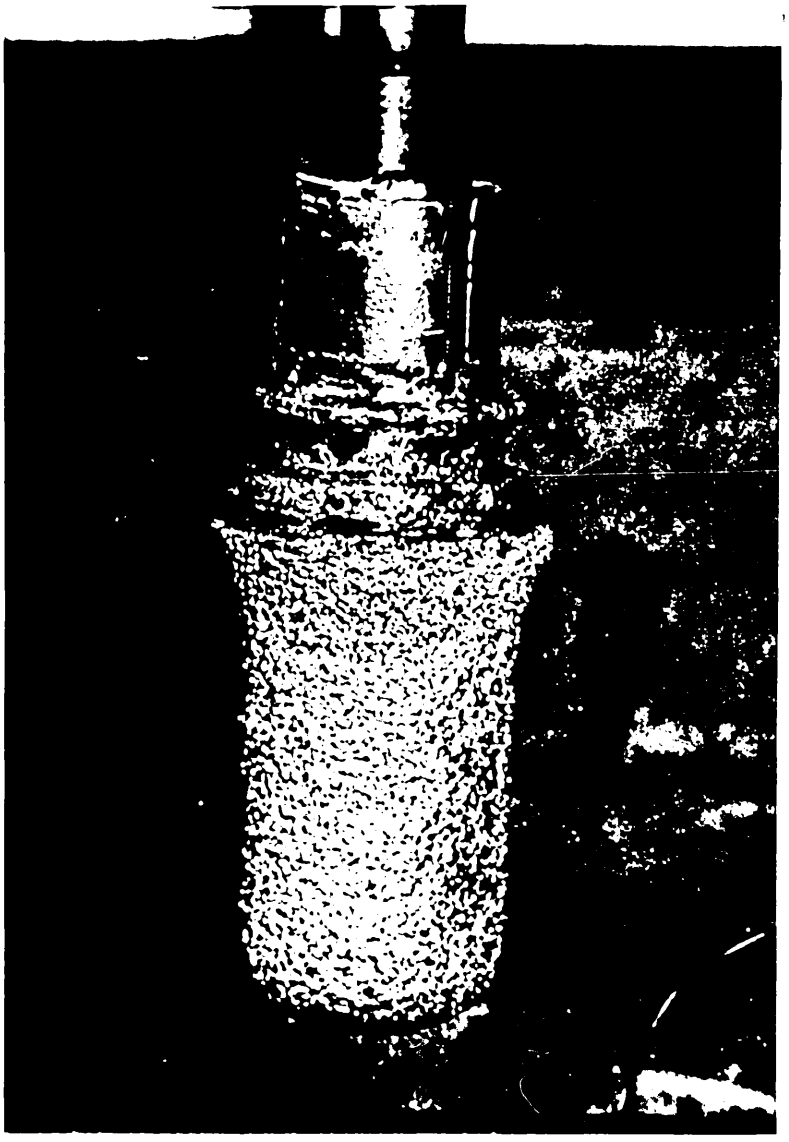

PLATE 7

Chill-layer growth on a Pb-probe from Pb-Sn eutectic bath under

(i) unstirred conditions

(ii) stirred conditions.

Magnification: x 20.

(iii) stirred conditions

Magnification: x 40.

Etchant: Acetic acid; Nitric acid; Glyserol = 1:1:4

PLATE 7

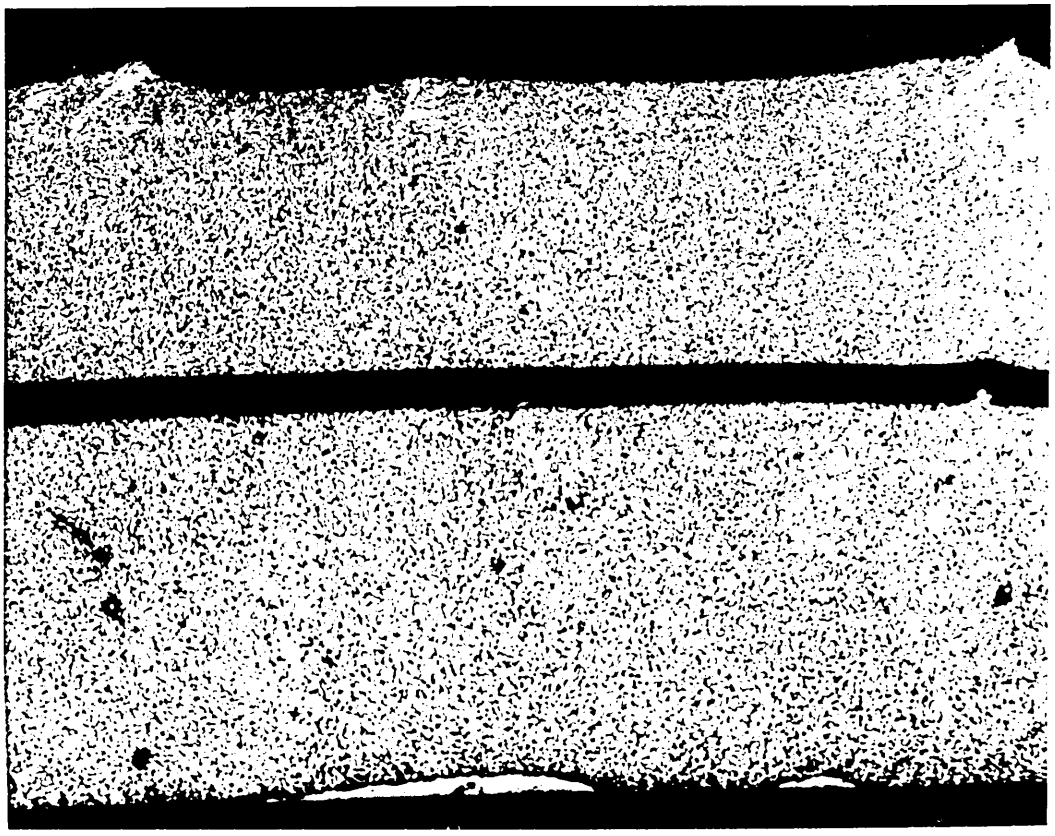

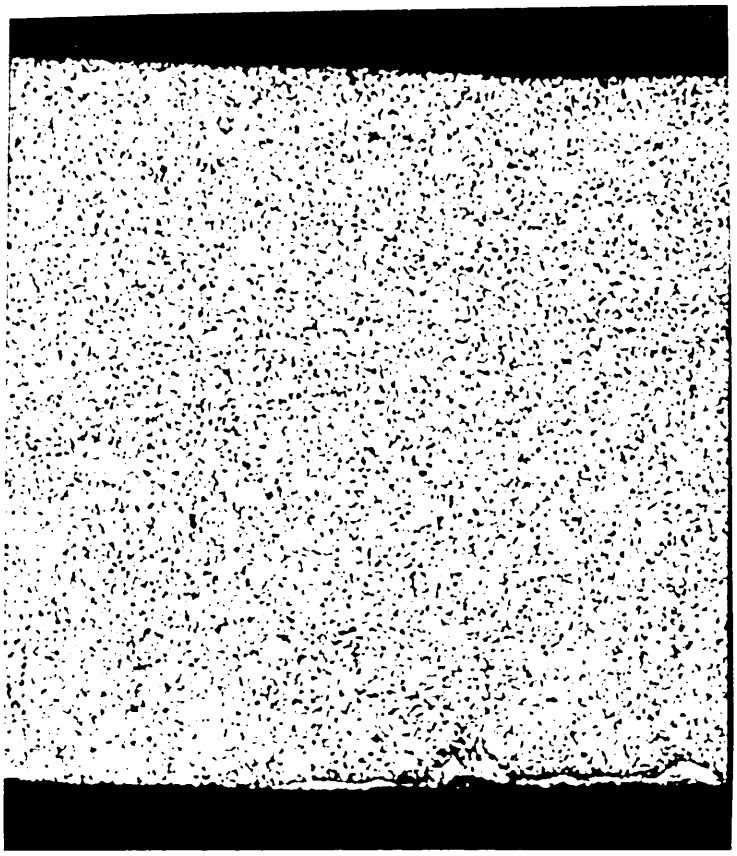

PLATE 8

A close up of one of the perturbations on the growing chill-layer shown on Plate 7 (top right-hand corner).

Magnification: x 60

A section taken (normal) through chill-layer (normal to the growth direction).

Magnification: x 60

Etchant: Acetic acid; Nitric acid; Glyserol = 1:1:4

Chill-layer resulxs

6.1.1 Chill-layer growth at Zero Superheat

The experimentally measured growth of the chill-layer on a pure Pb-probe immersed in a Pb - Sn eutectic bath at zero superheat using a probe rotation speed of 60 r.p•m. is shown by the error bars in Figure *21* Each error bar covers the range of chill-layer thicknesses determined for three separate immersions. The results are also tabulated in Table 1 which shows the mean of three thickness readings taken in tnree different radial directions at a specific height from the bottom of the pxobe, readings being taken at three such heights for each exposure time.

Experimental results obtained by Brooks under the same conditions are included in Figure *21* for comparison.

Also shown are the results of the present theoretical treatment for two different values of the interface heat transfer coefficient.

Figure 22 compares the experimental inside and outside wall temperatures of the probe with the theoretically predicted midwall temperatures.

6.1.2 Chill-layer growth and melt-back in superheated baths

The experimentally measured growth and melt-back of the chill-layers on pure lead probes immersed in Pb - Sn eutectic baths at 186°, 190°,195°> 200 , 210 and 220°C. are shown in Figures 23, 24, 26, 27, and are tabulated in Tables 1 - 8 . A probe rotation speed of **60** r.p•m. was used throughout.

These Figures also show the results of the present theoretical treatment for an appropriately chosen value' of the interface heat transfer coefficient. Some theoretical results due to Brooks, for similar conditions are also shown.

M

xxx Experimental

M—

HfH

HH

.X

l il *n* **JC**
O

i-wsX

JZ

SZ

.o

Figure 23 Chill-layer thickness ($r_c - r_s$) versus Time for 3 C superheat

oo
o
0)

ex

o o

0©

©0

©©

a.

-J

< m

Figure 26 Chill-layer thickness versus Time for 12°C

cP

o

CM

Time (sec

(0

8 to co CM 8 to CM

a

£

o o
st liJ

ti ■*

■xx

o

Ci

-I £L

-! s
< Lii
g: H

. \

Figure 29 Chill-layer thickness versus Time for 27 and 37 C superheat

HH M3H

O

C

CM

H

s

£1

o o

KO

X

x x

X XX

< oJ

Results obtained at bath temperatures above 220°C are given in tabular form only (Table) since the chill-layer thickness melt back times at these temperatures were relatively small.

6.1.3 Microstructural examination of chill-layer

Some microstructural examinations of chill-layers grown under either static or dynamic conditions showed a globular form of eutectic (Plates 7, 8) as opposed to the characteristically lamellar eutectic structure produced in the same composition when slowly cooled. (Plate 5.)

In an unstirred bath the growth of the chill-layer was accompanied by the formation of primary tin dentrites which caused a roughening of the chill-layer.

Plate 6 shows the rough surface appearance of the probe resulting from dendritic growth of the chill-layer. The upper of the two chill layers shown in the top photograph in Plate 7 shows how this roughness is related to the dendritic structure. The top photograph in Plate 8, which is a magnification of the top right hand portion of this chill layer, shows how each protuburence of the rough surface is related to an individual dendrite.

This dentritic growth was avoided by stirring the bath prior to immersion and by rotation of the probe. This can be seen from the lower of the two chill layers in the top photograph of Plate 7 , which has been grown under identical to the upper chill layer except that the bath was well stirred prior to the experiment, and the probe was rotated gently throughout the experiment.

6•^ Dissolution Results

Dissolution experiments have been carried out using probes made from the metals specified in Table *9,* under the conditions of bath temperature and rotation speed also specified in this Table. The weights of the probe before and after each experiment were recorded and used to calculate a mean dissolution rate, the total weight loss being divided by the initial cylindrical surface area of the probe in contact with the bath and by the time for which the probe surface was in contact with the bath. This latter time was determined as the total time of immersion less the time determined in the previous section for the melt-back of the chill layer. The results of these experiments are shown in Tables 10-16. . No measurements could be obtained for the alloys containing *QOfo* and 9*Off*o tin since the probes were attacked so rapidly that they disintegrated.

In addition probes removed from the bath were examined and photographed and sections were obtained for metallographic observation. These plates are presented in Section 6.2.5.

6.2.1 Dissolution Rates

The mean dissolution rates listed in Tables 10-16 are plotted in Figures 51 - 55 as a function of exposure time. Figure 51 shows the results for lead obtained when the rotation speed of the probe was 60 r.p.m. The Figure shows that the mean dissolution rates do not vary very much with exposure time, but increase quite rapidly with bath temperature. Figure 52 shows the results obtained for lead when the bath temperature was 250°C. These results show that the dissolution rate increases slightly with exposure time and very markedly with the speed of rotation.

Dissolution Results

TABLE 9

EXPERIMENTAL CONDITIONS FOR DISSOLUTION EXPERIMENTS

Probe Metal	Bath Temp. (°C)	Rotation Speed (r.p.m.)
Pb	200	60
	220	60
	230	0
		30
		60
		120
	250	60
		120
Sn	200	30
		41
		60
		120
90% Pb 10% Sn	230	50
		100
10% Pb 90% Sn	190	60
20% Pb 80% Sn	190	60

FIGURE 31

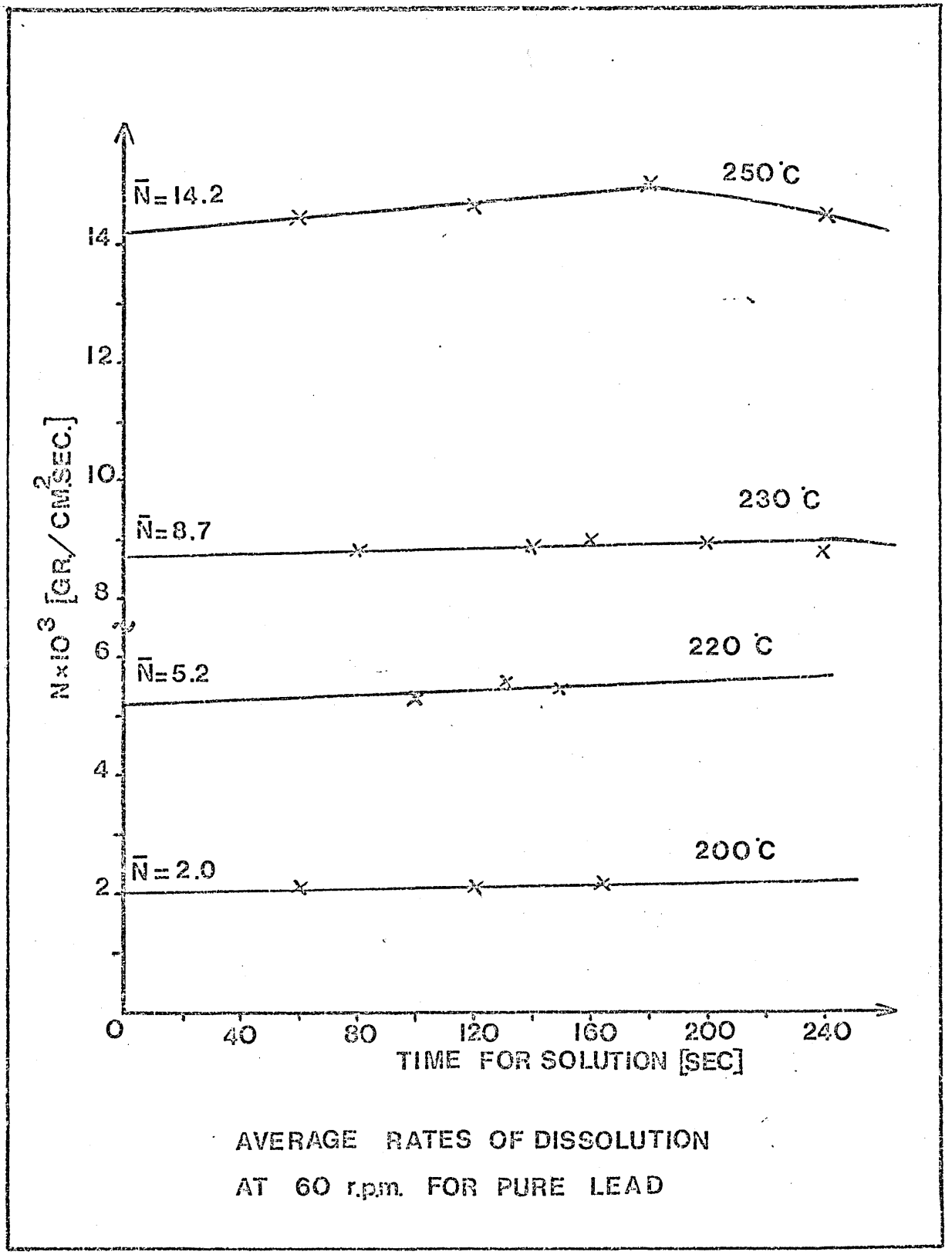

AVERAGE RATES OF DISSOLUTION
AT 60 r.p.m. FOR PURE LEAD

Average rates of dissolution for pure lead at different rotation speeds but constant temperature (230°C)

16-

120 r. p.m

N=14.1

60 r.p.m

N=8.7

30 r.p.m

N= 5.98

N=4.25

r.p.m

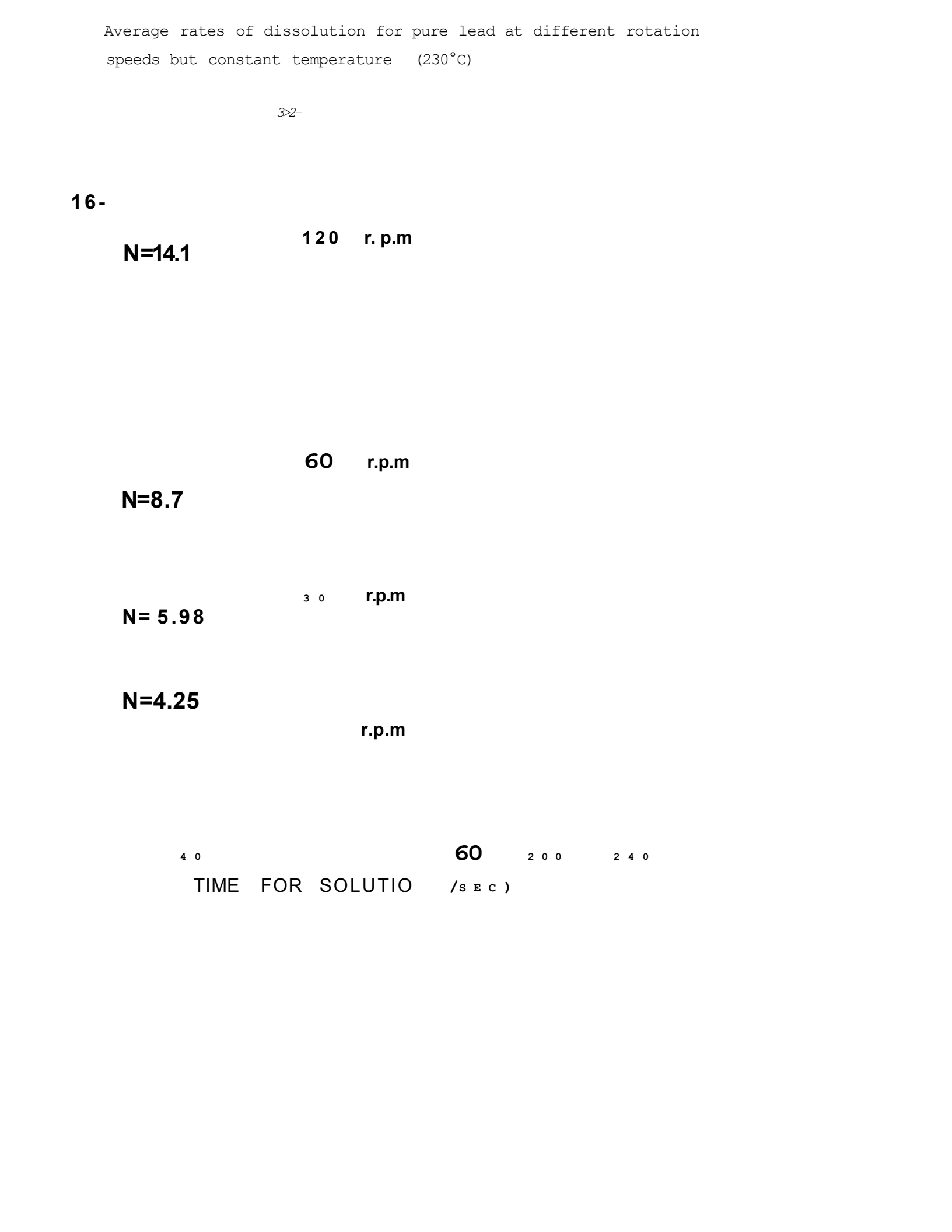

The results obtained for lead at 120 r.p.m. and at two different bath temperatures are shown in Figure 33 . The results obtained at 120 r.p.m. after fairly long exposure times suggest that the dissolution rate increases slightly at first with exposure time and then starts to decrease again.

Figures 34 and 35 show that the results obtained for pure tin and 90%Pb-10% Sn probes tend to behave in a similar way to the results for lead.

6.2.2 Calculation of Mass Transfer Coefficient

The dissolution rates presented in the previous section have been used to calculate mass transfer rates on the assumption that the dissolution process is controlled by mass transfer as outlined in Section 3.4.2.

Equation (117) in that section:

$$n''_B = \frac{\mathcal{D}^{\circ}_{AB} C_T}{(C^*_A)_{Ln}} \left[(C^*_B)_L - (C^*_B)_b \right] \qquad (a)$$

can be re-written in the form:

$$n''_B = \frac{\mathcal{D}^{\circ}_{AB}}{(C^*_A)_{Ln}} \left[(C_B)_L - (C_B)_b \right] \qquad (b)$$

where $(C_B)_L$ and $(C_B)_b$ are the mass concentrations of the dissolving metal at the liquidus, i.e. in equilibrium with the surface of the probe, and in the bulk of the liquid phase.

Equation (b) has been used to calculate values of $\mathcal{D}^{\circ}_{Pb\ Sn}$ from the initial dissolution rates obtained by extrapolating the lines in Figures 31 - 35 back to zero exposure time. The values involved in these calculations are set out in in Tables 17 and 18.

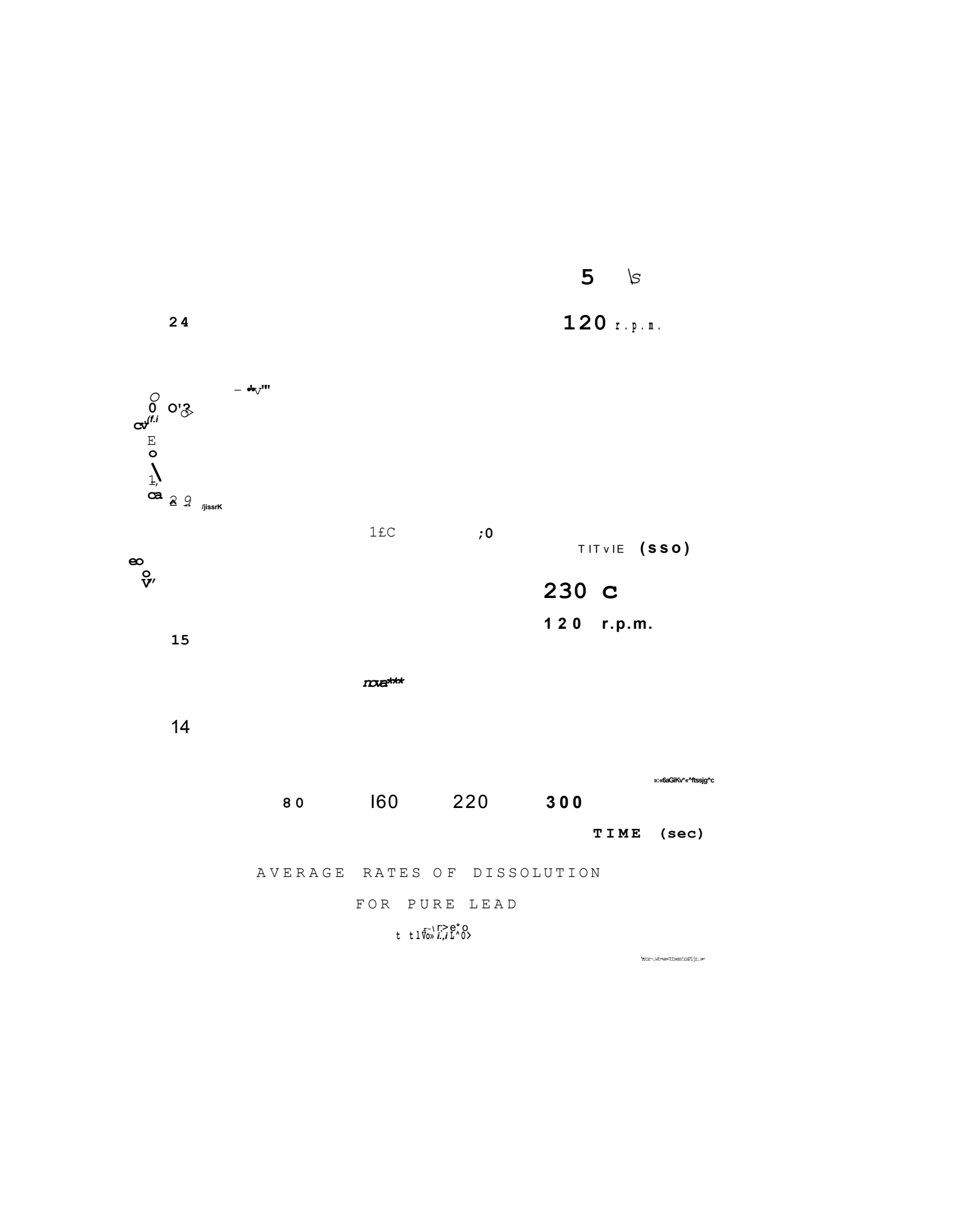

AVERAGE RATES OF DISSOLUTION

FOR PURE LEAD

FIGURE *34*

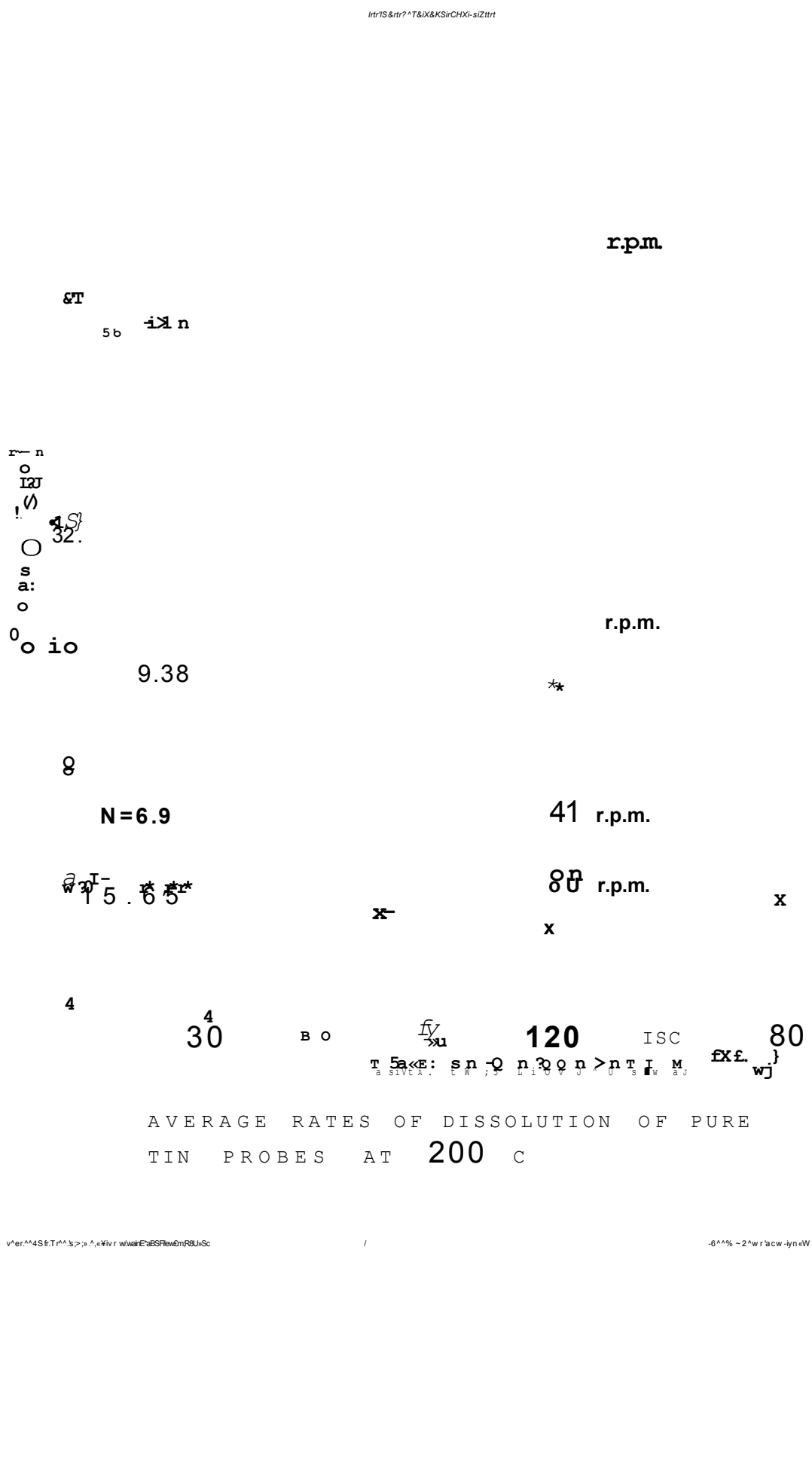

AVERAGE RATES OF DISSOLUTION OF PURE TIN PROBES AT 200 C

FIGURE 53

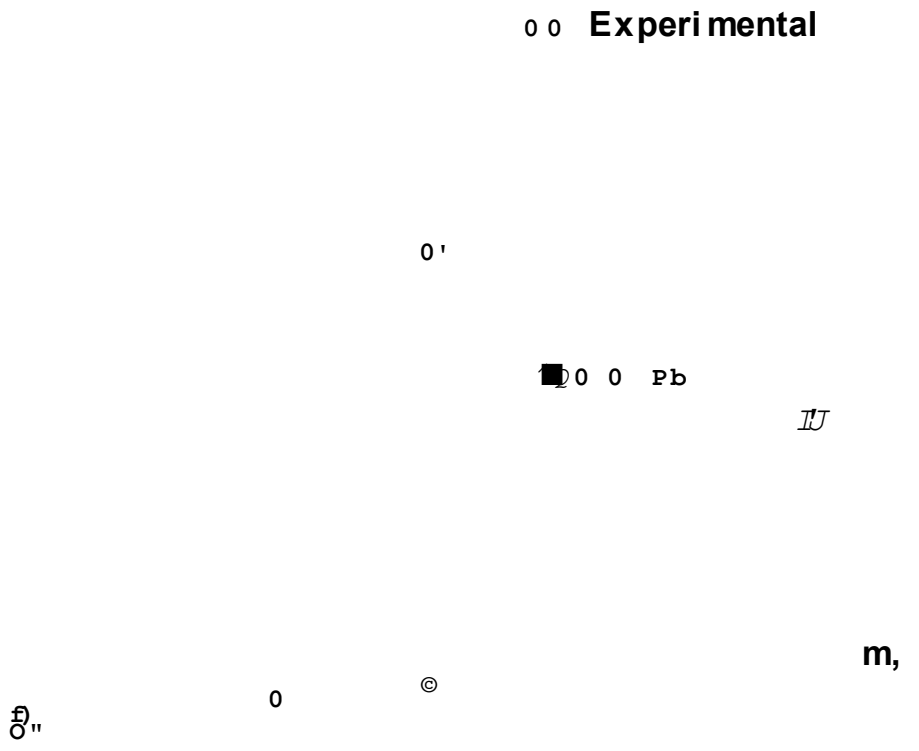

AVAREGE RATES OF DISSOLUTION-AT 230 'C

Probe Metal	Bath Temp. °C.	Rotation Speed r.p.m.	$\bar{N} \times 10^3$ initial dissolution rate ($gr/cm^2 sec.$)	$(C_B)_L$ = mass Conc. of dissolving metal at Liquidus (gr/cm^3)	$(C_A)_{ln}$ = log mean mass fraction of non-dissolved metal	$^{o}_{Pb\ Sn}$ = Mass transfer coefficient (cm/sec.)
Pb	200	60	2	3.61	0.62	2.22
	220	60	5.2	4.37	0.55	2.18
		0	4.25			1.06
	230	30	5.98	5.13	0.52	1.49
		60	8.7			2.18
		120	14.1			3.52
	250	60	14.2			2.13
		120	22.52	5.96	0.46	3.38

TABLE 17 Calculation of Mass Transfer Coefficients for Pb - Probes

Probe Metal	Bath Temp. °C.	Rotation Speed r.p.m.	$\bar{N} \times 10^3$ initial dissolution rate ($gr/cm^2 sec.$)	$(C_B)_L$ = mass Conc. of dissolving metal at Liquidus (gr/cm^3)	$(C_A)_{ln}$ = log mean mass fraction of non-dissolved metal	$^{o}_{Pb\ Sn}$ = Mass transfer coefficient (cm/sec.)
		30	5.65			1.83
Sn	200	41	6.9			2.235
		60	9.38	5.88	0.928	3.04
		120	14.9			4.28
90% Pb		50	7.2			1.79
	230			5.13	0.52	
10% Sn		100	11.8			2.95

TABLE 18 Calculation of mass transfer coefficients for Sn and (90% Pb - 10% Sn probes)

Values of the $(C_L)_{D,M}$, the mass concentration of the dissolving metal, have been calculated from the bath temperature using the lead/tin phase diagram shown in Figure 36• This Figure gives the mass fractions at the liquidus, and the values of the mass concentrations were then calculated using the relationship presented- by W. Hofmann ^ for the variation of the density of lead/tin melts with composition. The values for $(C_{x,j})_T$ for the experiments involving the 10*jo* Sn, *Qffo* Pb probe were calculated as if the probe were made of lead. However, the value of dissolution rate used to calculate the mass transfer coefficient was taken to be the rate at which lead dissolved from the alloy probe, i.e. $^9/_{*y}$ ^ths of the rate at which the probe dissolved.

Values of (C-g)^ were calculated in a similar manner from the eutectic composition shown in Figure 36. These values are

(Cpb)b = 3.05 g/cm5 (for 230°C.)

(cgn)b = 4.958 g/em5 (for 200°C.)

The values of the limiting mass transfer coefficient shown in Tables 17/18 are plotted in Figure 37 • The Figure also shows twp theoretical curves for the mass transfer coefficient in the system. The Figure will be discussed later.

Weight Percent Lead

Oin;eiodujOj_

FIGURE 56

Lead- Tin Phase Diagram

Comparison of the present limiting mass transfer corfficient with same other investigations

6*2.3 Visual Observation of the Probe System

The outer probe surface was visually examined after each experiment. Typical appearances of the probes are shown in Plates 9 to 17.

Plate 9 shows a pure lead probe freshly machined and ready to be immersed in the eutectic bath, Plate 10 showing the patchy uneven attack that occurred when unmachined probes were used in the experiments. All the subsequent Plates show the appearance of machined probes after dissolution attack. Plate' 11 shows a lead probe that had not been rotated during dissolution. It can be seen that the attack on the probe surface has tended to follow the vertical lines of the natural convection induced flow. Plate 12 shows the surface of a tin probe after it had been rotated at 41 r.p.m., equivalent to a Taylor Number of3.2xlO^ It can be seen that the attack on the probe now tends to follow tangential flow of the fluid flowing past the probe. Plate 13 shows a lead probe that was rotated at 60 r.p.m. mo 60~ 4.6x10^ during dissolution, and it can be seen that the regular tangential patterns of erosion are beginning to be disturbed by the more intense motion. Plate 15 shows tin probe treated under the same hydrodynamic conditions and showing a very similar appearance. A similar disturbance to the regular erosion patterns is demonstrated in Plate 14 which shows a lead probe rotated at 40 r.p.m. for some time and then at 80rpm Ta0~= 6.2x10^. Plate 16 shows the appearance of a lead probe after a dissolution experiment at 120rpm Ta = 9.2 x 10^. It can be seen that the regular patterns of erosion have been broken down completely. The pattern has been similarly broken down in the case of the probe shown in Plate 17* This probe had been mounted on the rotor mechanism with a slight eccentricity. It was then rotated at 60 r.p.m. super imposing a vibratory motion on the

PLATE 9

A Pb-probe, as machined prior to dissolution experiment

PLATE 10

A dissolution experiment

carried out with a Pb-probe

without surface machining

PLATE

PLATE 11

The surface appearance

of a Pb-probe exposed to a Pb-Sn eutectic bath

under static conditions

PLATE 11

PLATE 12

Probe: pure tin

Bath temperature: 200°C.

Rotation speed: 41 r.p.m.

Dissolution time: 180 secs.

PLATE 12

PLATE 13

Probe: Pure lead

Bath temperature: 230°C.

Rotation speed: 60 r.p.m.

Dissolution time: 220 secs.

PLATE 13

PLATE 14

Probe metal: pure lead

Bath temperature: 230°C.

	Rotation Speed (r.p.m.)	Dissolution time (secs.)
(i)	40	80
(ii)	80	80

PLATE 14

PLATE 15

Probe metal: Pure tin

Bath temperature: 200°C.

Rotation speed: 60 r.p.m.

Dissolution time: 120 secs.

PLATE 15

PLATE 16

Probe metal: pure lead

Bath temperature: 230°C

Rotation speed: 120 r.p.m.

Dissolution time: 180° sec.

PLATE 16

PLATE 17

Probe metal: pure tin

Bath temperature: 200°C.

Rotation speed: 60 r.p.m.

Dissolution time: 160 sec.

PLATE 17

regular tangential flow.

6.2.4 Metallographic Examination of the Dissolving Probe Materials

A number of sections were taken through the walls of probes after dissolution and examined metallographically. Typical macro- and micrographs areshown in Plates 18 to 26. They have been prepared as outlined in section 5.1.3. Plates 18 to 21 show sections through pure lead probes after dissolution attack at 120 r.p.m. Plates 18, 20 and 21 show that the uneveness of the surface attack is unrelated to the grain size, grain orientation or to the grain boundaries. Plate 19 demonstrates the problems involved in preparing micrographs of pure lead. The surface shown in this Plate had been polished for 4 hours, whereas the other three plates show surfaces that had been polished for 8 hours. The surface that had been polished for a mere 4 hours still shows signs of the falsely fine grain size produced by recrystallisation during the sawing of the section from the probe.

Plate 22 shows sections through a 80% Sn - 20% Pb probe the upper section having been photographed before the dissolution experiment and the lower section after a second dissolution time. The overall attack on the surface appears to have been fairly uniform except that there is evidence of a more rapid attack into the interdendritic eutectic metal. When longer dissolution experiments were attempted with this alloy, the probe disentegrated, the bottom section of the probe breaking off from the remainder. The breaks appeared to be due to partial melting of the eutectic metal, especially in eutectic rich regions in the probe. This is demonstrated in Plate 23, where the upper micrograph shows eutectic dense regions in a probe of this alloy, and the lower micrograph is taken through the region of fracture.

PLATE 18

Macrostructure of a lead probe after a dissolution experiment

Sectioned normal to the surface, viewed by oblique illumination.

Experimental conditions:

Bath temperature = 230°C

Dissolution time = 180 seconds

Magnification: x 2.5

Rotation speed = 120 r.p.m.

As above

Magnification: x 10

PLATE 19

Typical ambiguous structure produced as a result of incomplete preparation technique.

Experimental conditions:

Probe material = lead

Rotation speed = 60 r.p.m.

Dissolution time = 150 seconds

Magnification: x 20

As above

Magnification: x 40

PLATE 19

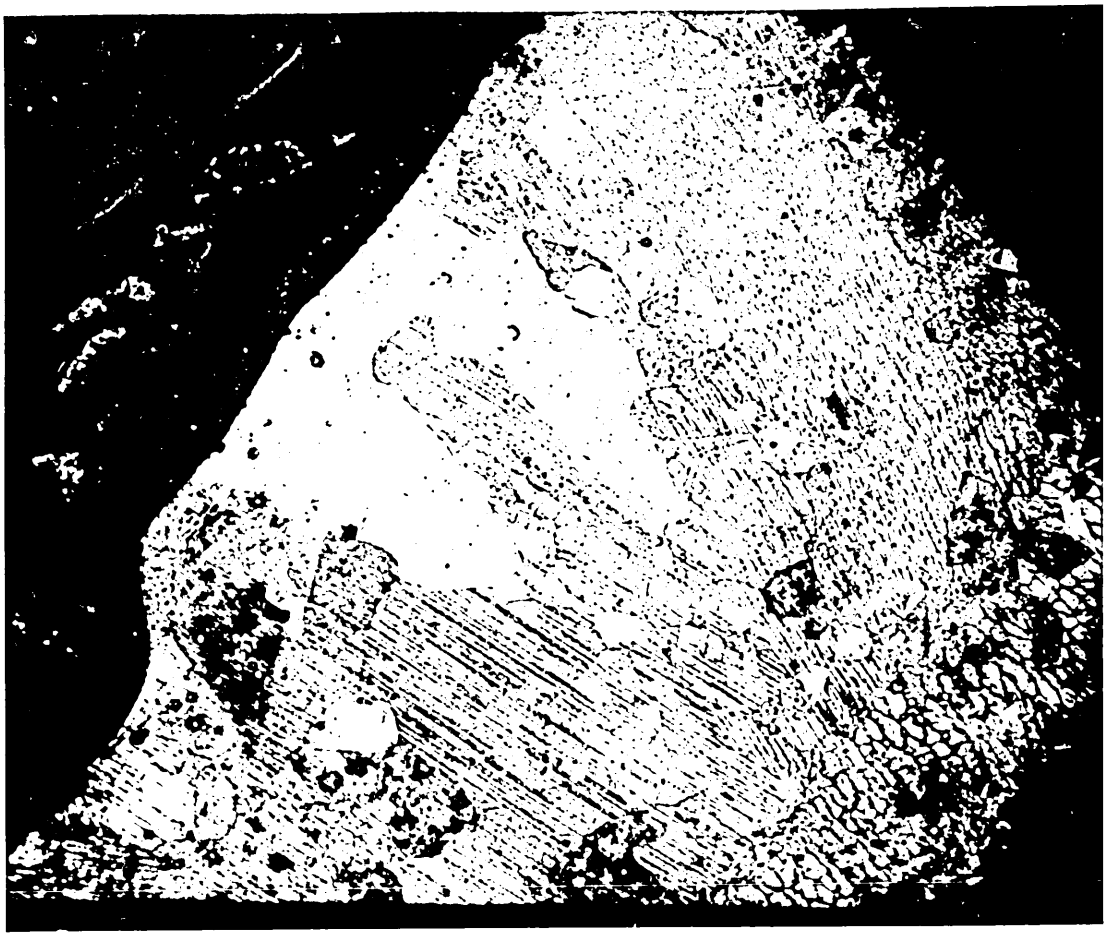

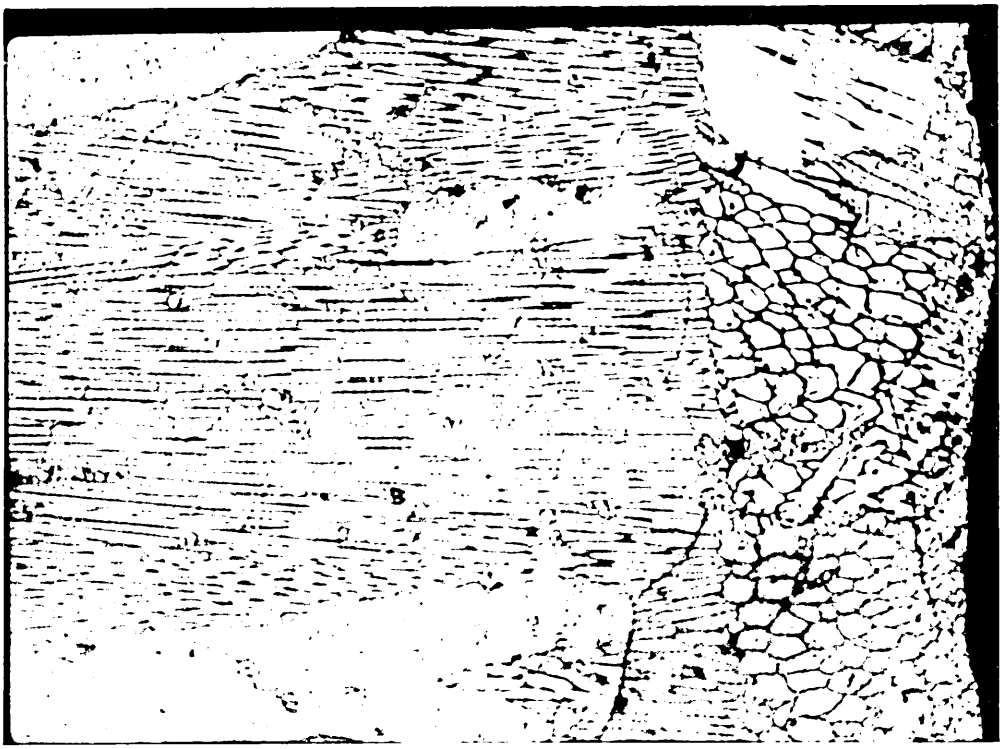

PLATE 20

Macrostructure of a lead probe after a dissolution experiment.

Sectioned normal to the surface, viewed by oblique illumination.

Experimental conditions:

Bath temperature:	230°C
Rotation speed:	120 r.p.m.
Dissolution time:	120 seconds
Magnification:	x 15

PLATE 20

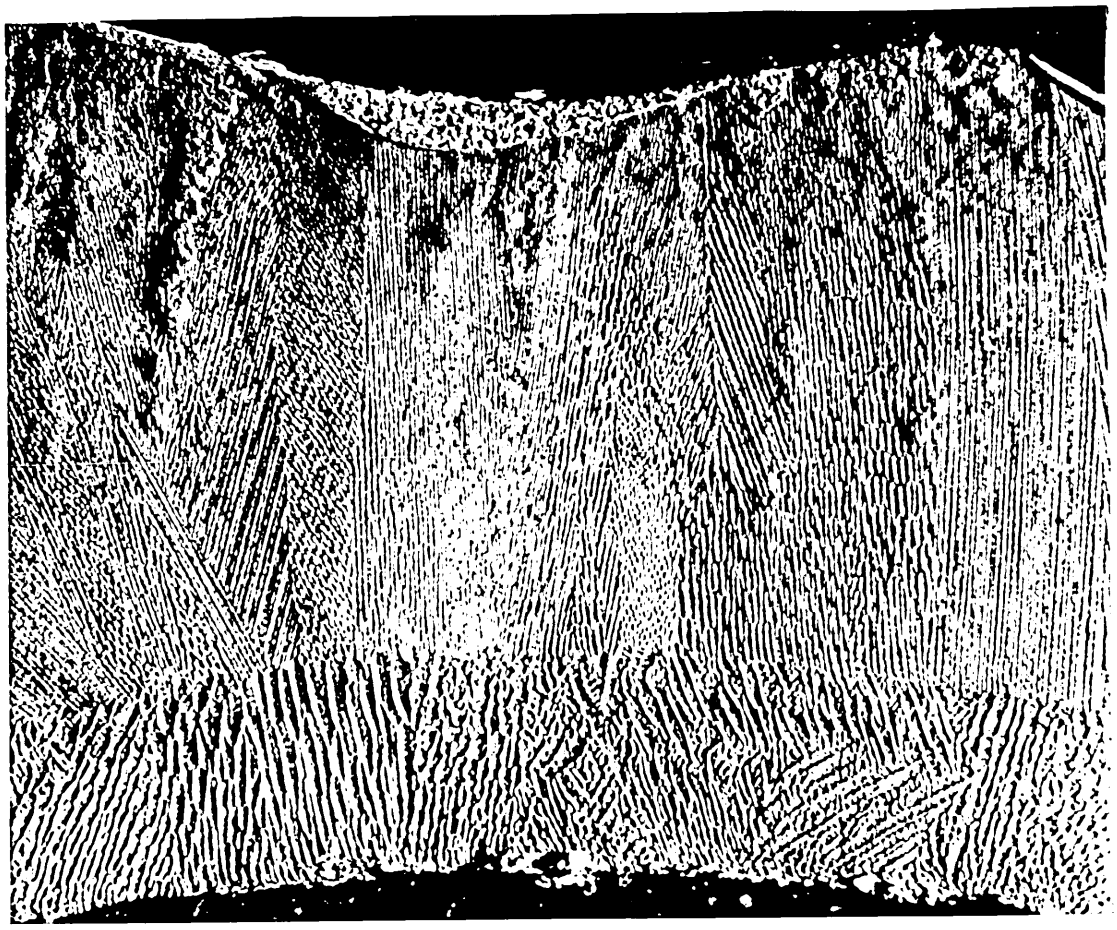

PLATE 21

Macrostructure of a lead probe after a dissolution experiment.

Sectioned normal to the surface, viewed by oblique illumination.

Experimental conditions:

Bath temperature	=	230°C
Rotation speed	=	120 r.p.m.
Dissolution time	=	160 seconds

Magnification: x 10

As above

PLATE 21

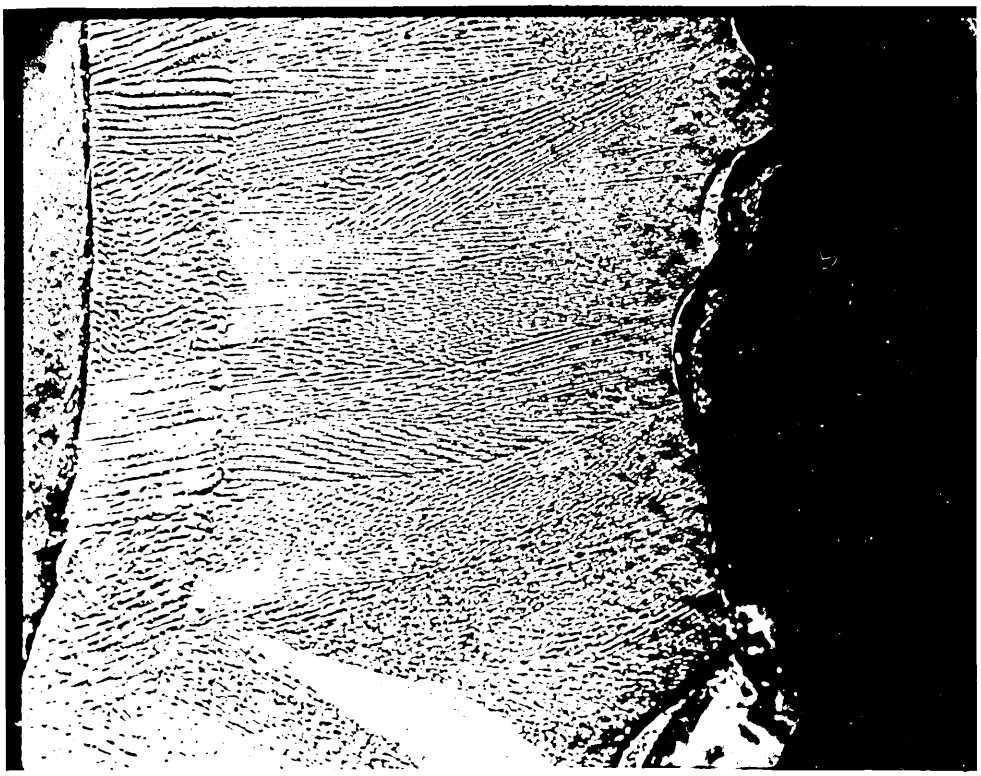

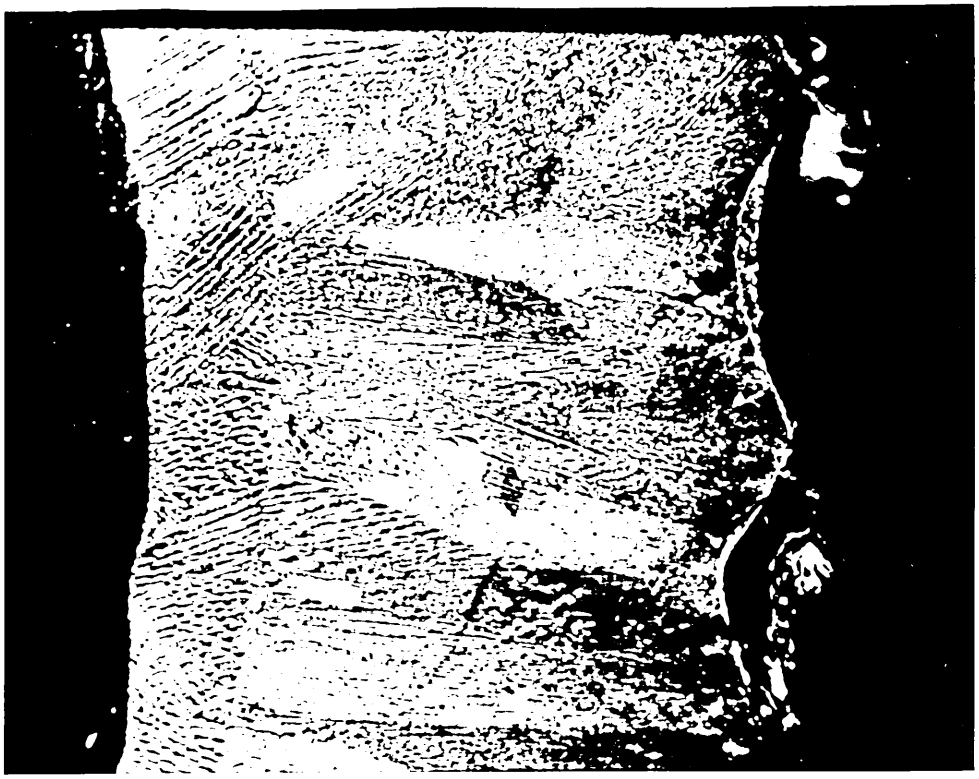

PLATE 22

Microstructure of 80 wt.% Sn, 20 wt.% Pb alloy probe before dissolution experiment. (Sectioned normal to the surface.)

x 60

Microstructure of above alloy after 30 seconds of dissolution time (right hand side of the picture being the attacked surface).

Experimental conditions:

Bath temperature = 190°C

Rotation speed = 60 r.p.m.

Etchant: 5% Nital

x 60

PLATE 22

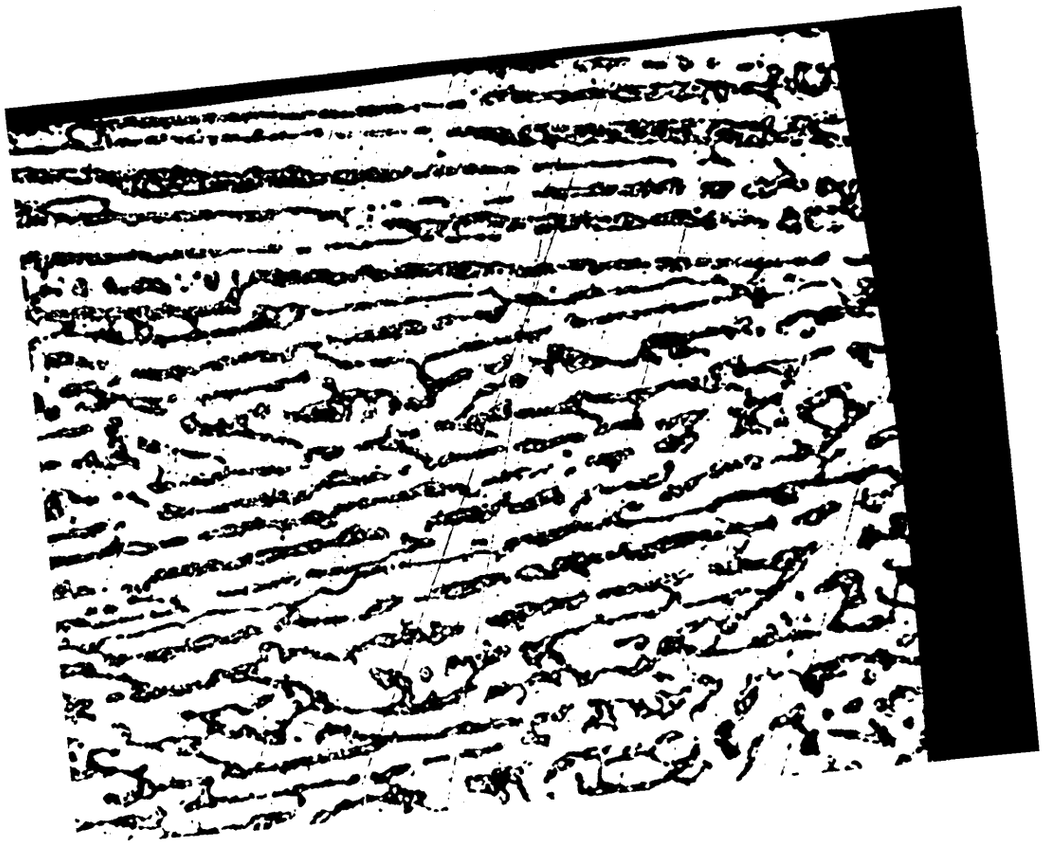

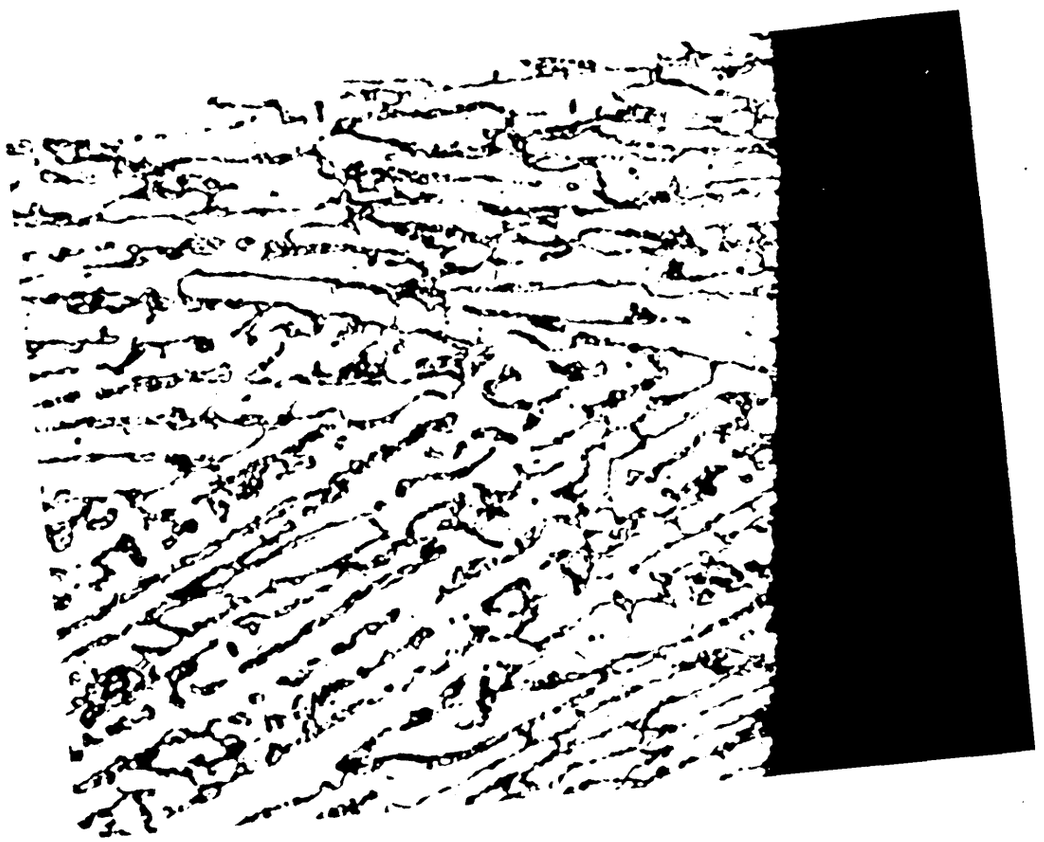

PLATE 23

Microstructure of 80 wt. % Sn, 20 wt % Pb alloy prior a dissolution experiment.

(Sectioned normal to the solidification direction)

Magnification: x 80

Microstructure of the above alloy after 60 seconds of dissolution time (section taken in the vacinity of the point at which the probe broke).

Experimental conditions:

Bath temperature = 190°C

Rotation speed = 60 r.p.m.

Magnification: x 120

Etchant: 2% Nital

PLATE 23

Plate 24 shows a 90% Sn - 10% Pb alloy probe after 40 seconds of dissolution time. The section A-A through the probe illustrates the approximate region in which sections were taken for all the micrographs shown here. The micrograph in the lower picture shows the surface region, the attacked surface being on the right hand side. Once again, there is evidence of more rapid attack into the eutectic metal. The upper micrograph of Plate 25 shows the surface of a similar probe after exposure to dissolution attack for 60 seconds. The more rapid attack in the eutectic regions is more obvious on the dissolution surface, (the right hand face of the upper micrograph). The lower micrograph, presented for completeness, shows a section parallel to the surface of the probe. Only a limited range of experiments could be carried out with this alloy since, once again, the alloy disintegrated after longer exposure times and at higher rotation speeds.

Plate 26 shows a section across the wall of a pure tin probe. The two micrographs at different magnifications, both demonstrate that the uneven surface attack is unrelated to the grain size, grain orientation or grain boundaries for tin as it is for lead.

Plate 27 shows the appearance of an attacked 90% Pb - 10% Sn probe and a micrograph of the structure of this probe taken parallel to the surface of the probe.

PLATE 24

A 90 wt. % Sn, 10 wt. % Pb alloy probe after 40 seconds of dissolution time.

Experimental conditions:

Bath temperature = 190°C.

Rotation speed = 60 r.p.m.

Microstructure of section A - A of above probe. Right hand side of the section showing attacked surface.

Magnification: x 60

Etchant: 5% Nital

PLATE 24

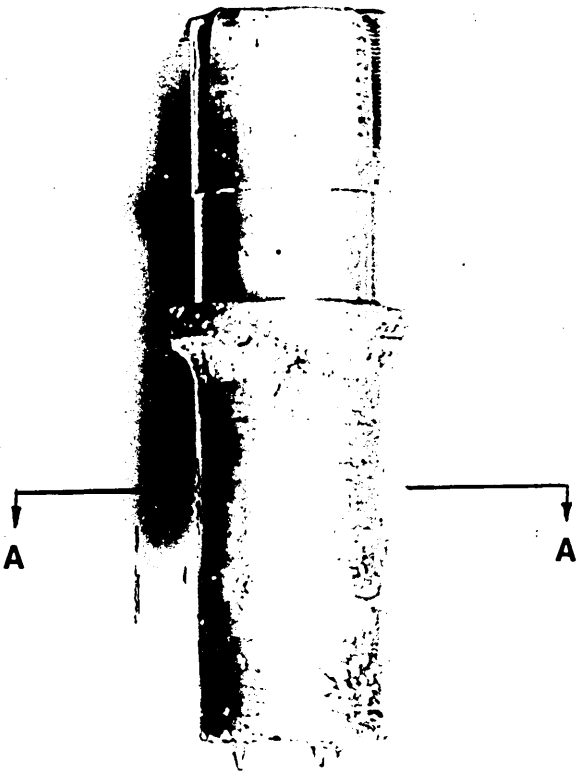

PLATE 25

Microstructure of a 90 wt. % Sn, 10 wt. % Pb alloy after 60 seconds of dissolution time, (sectioned normal to the surface).

Right hand side of the section showing attacked surface.

Experimental conditions:

Bath temperature = 190 C.

Rotation speed = 60 r.p.m.

Magnification: x 60

As above (sectioned normal to the solidification direction)

Etchant: **2% Nital**

PLATE 25

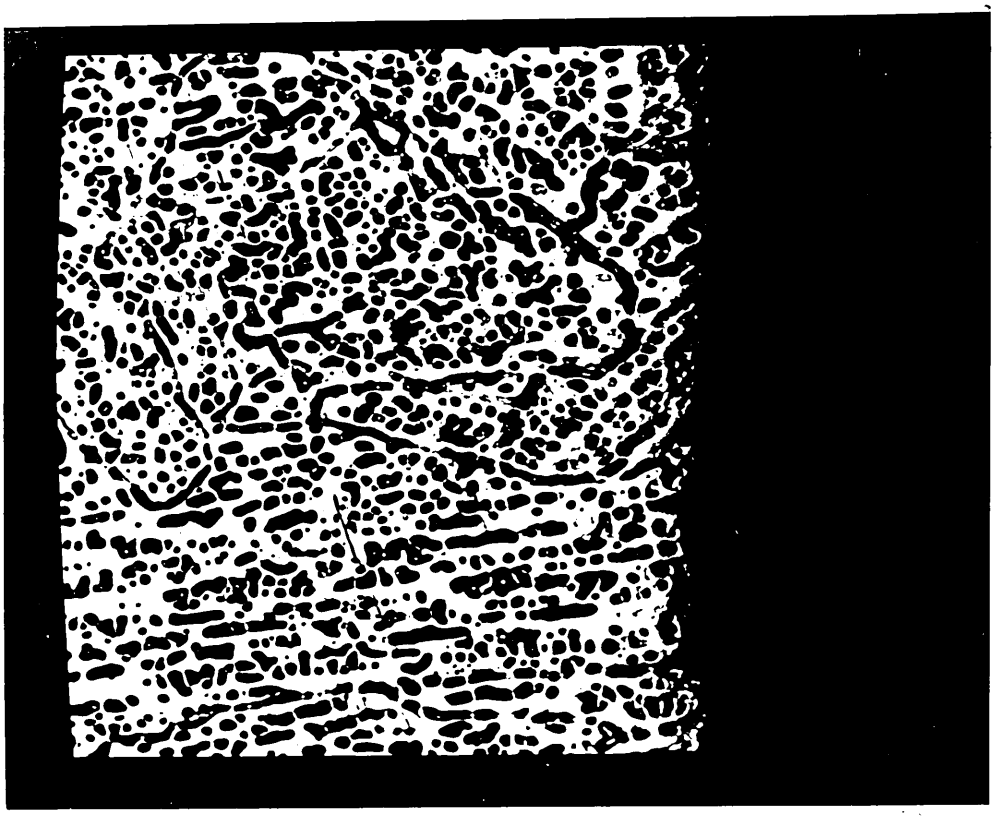

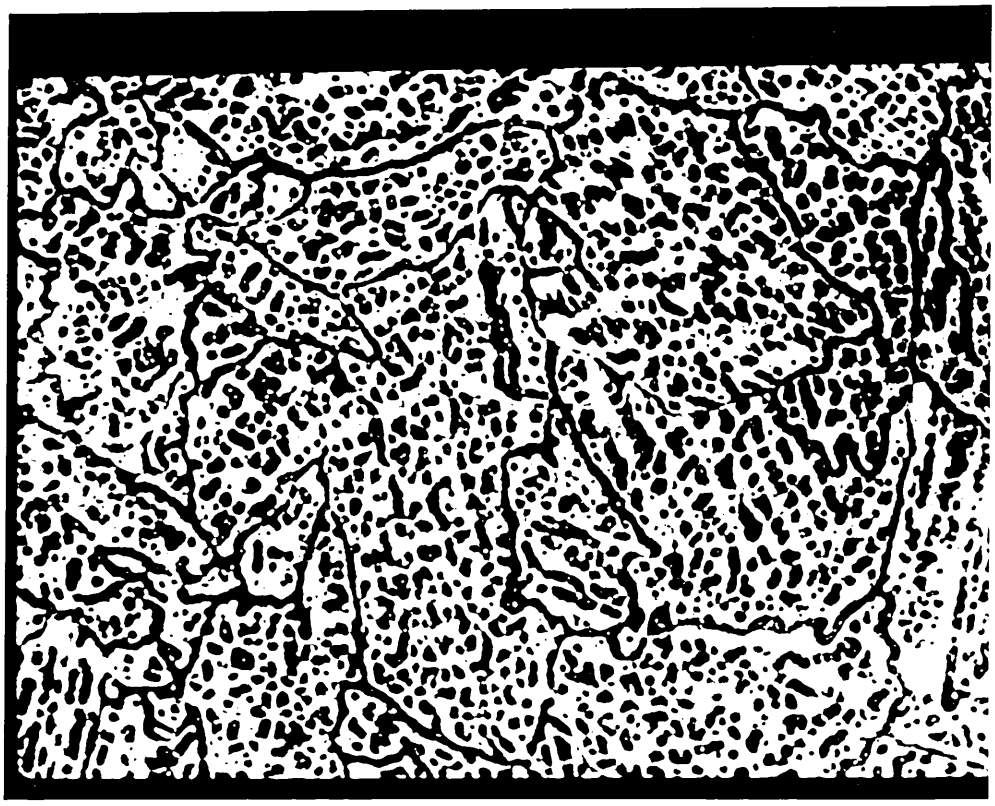

PLATE 26

Macrostructure of pure tin probe after a dissolution experiment, sectioned normal to the surface.

Experimental conditions:

Bath temperature = 200°C

Rotation speed = 60 r.p.m.

Dissolution time = 120 seconds

Magnification: x 10

As above

Magnification: x 15

A'Wx X

PLATE 27

The surface appearance of a 90 wt. % Pb, 10 wt. % Sn alloy probe after 100 seconds of dissolution time.

Experimental conditions:

Bath temperature = 230°C.

Rotation speed = 100 r.p.m.

Microstructure of the above probe(sectioned normal to surface).

Magnification: x 60

Etchant: 2% Nital

PLATE 27

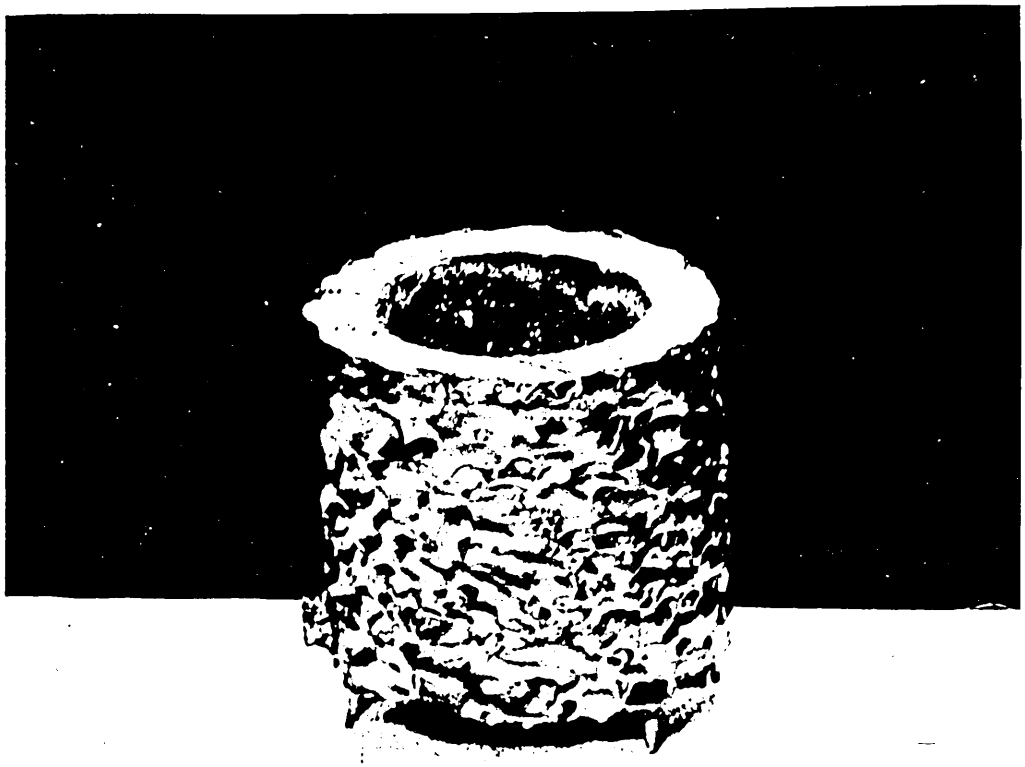

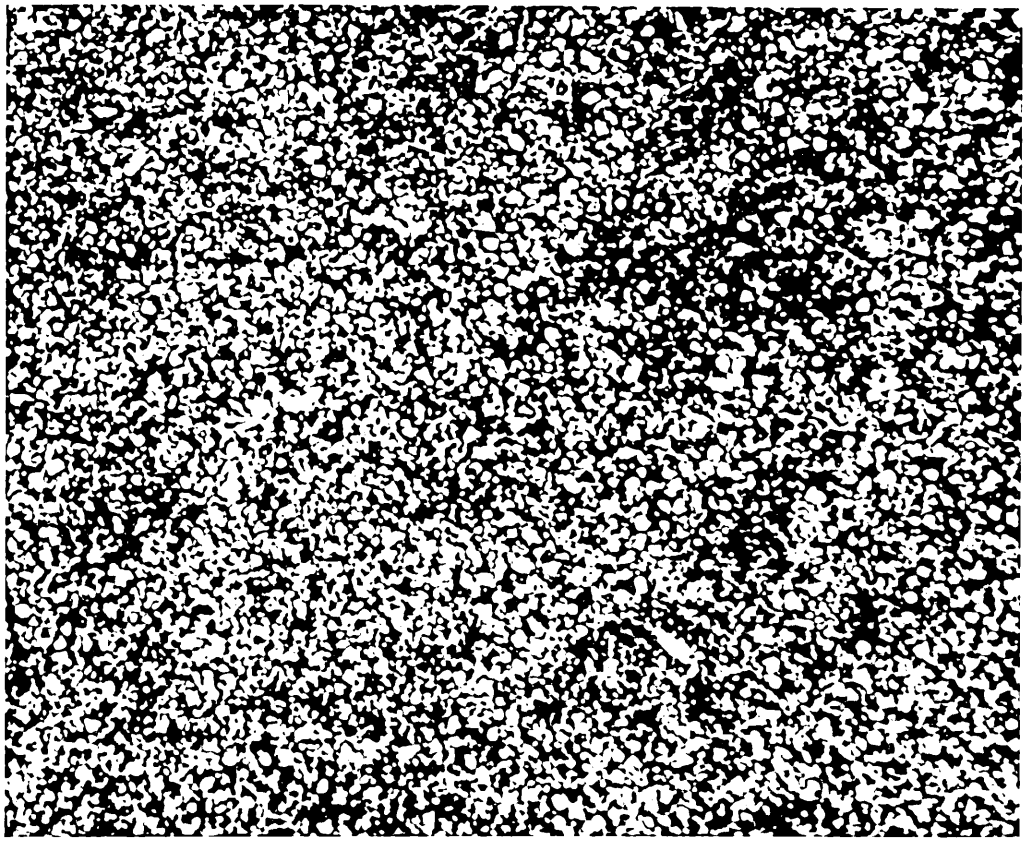

7 DISCUSSION

7.1 Introduction

The main object of this project was to establish conditions for successful cladding. For this purpose heat transfer phenomena during growth and melt back of a chill layer on a cylindrical substrate and the subsequent dissolution process were studied theoretically and experimentally.

Although the experimental results were mostly used to test the theories involved occasionally they were also used as an aid for making correct assumptions during the development of the theory.

7.2 Theoretical treatment of the heat transfer nhenomena

7.2.1 A comparison of the integral profile methods for cylindrical and planar cases at zero superheat.

A comparison between the integral profile methods for planar and cylindrical cases is shown in Figure 38 .

An integral profile method derived for a plane wall as applied to a cylindrical shape without making any allowance for the reduction in area normal to the heat flow direction, showed discrepencies between the predicted and measured values for chill-layer thicknesses and wall-temperatures. Figure 38 shows that the predicted chill-layer thickness is greater than the actual value at all times.

For zero superheat a "correction factor" can be obtained for each thickness using the solidification front radius predicted by the cylindrical method (r_{oL}) and a simple heat balance comparison between the two geometries . For a plane wall the heat balance for any solidification front radius r_d gives:

FIGURE 38 Chill-layer thickness versus Time curves for planar and cylindrical integral profile methods (zero

heat released during solidification = heat gained by the wall

$$\rho_s H (r_{s_1} - r_o) = Cp\, \rho_w\, \theta_s (r_o - r_r) \qquad (118)$$

calling $r_{s_1} - r_o = t_1$

$$t_1 = \frac{Cp\, \rho w}{s\ H}\ \theta_s\ (r_o - r_r) \qquad (119)$$

Similarly for the cylindrical case

heat released

$$\rho_s H (r_{s_2}^2 - r_o^2) = Cp\, \rho_w\, \theta_s\, (r_o^2 - r_r^2) \qquad (120)$$

calling $r_{s_2} - r_o = t_2$

$$t_2 = \frac{Cp \rho w\, \theta_s}{\rho_s\ H} - \frac{(r_o - r_r)(r_o + r_r)}{(r_{s_2} + r_o)} \qquad (121)$$

dividing (t_2) by (t_1) we get

$$\frac{t_2}{t_1} = \frac{(r_o + r_r)}{(r_{s_2} + r_o)} \qquad (122)$$

or

$$t_2 = \frac{(r_o + r_r)}{(r_{s_2} + r_o)} \qquad (123)$$

The broken line in Figure 38 shows corrected thickness values (P.M. corrected) obtained by applying equation (123) to the results of the planar integral profile method (P.M.) The values are in good, but not perfect, agreement with the values actually predicted by the cylindrical method (C.M.). As would be expected the uncorrected predictions of the planar integral profile method give greater thicknesses than the cylindrical method. As the heat balance shows, this is because the extraction of a given quantity of heat will result in the solidification of a progressively decreasing thickness of solid metal on the outside of the cylindrical probe. In the case of a plane wall, there

would be no such decrease, so that the planar integral profile method will predict the greater thicknesses.

The theoretical curves in Figure JQ have been calculated using a value of 2250 $W/m^2\ ^oC$ for the interface heat transfer coefficient between the inner surface of the solidifying metal and the outer surface of the probe wall. The value of this coefficient is discussed in the next Section.

7.2.2 Interface heat transfer coefficient

One unknown parameter in the heat transfer model for the growth and melt back of the chill-layer is the heat transfer coefficient describing the transfer of heat across the interface between the solidified chill layer, and the outer surface of the probe. The value adopted in this work for this coefficient is 2250 $W/m^2\ ^oC$. This value has been determined by a trial and error procedure in-which chill layer thicknesses and temperature variationspredicted by the cylindrical integral profile method for zero superheat using different values of the interface heat transfer coefficient were compared with the values determined experimentally.

Figure 21 shows growing chill layer thickness predicted using the two indicated values of the coefficient compared with the experimentally measured thicknesses.

7.2.3 The predictionof chill layer growth and melt back in the presence of superheat.

Figures 21 to 30 , showing the growth and melt back of chill layers of lead-tin eutectic on the lead probe, and the accompanying change of inner and outer wall temperatures^show computer predictions

as well as experimental'results. The predictions have been made using the equations developed in Sections and 3»3*2 for heat flow in the chill layer and in the probe wall, and the third model for heat transfer in the liquid metal described in Section 3■>3-3•

The experiments in which the results shown in these Figures were obtained were carried out at 60 r.p.m., over a range of liquid metal temperatures representing degrees of superheat varying from 3°S to 37°C.

The agreement achieved between theory and experiment for the chill layer thicknesses is remarkably good considering this range of degrees of superheat. The figures showing how the wall temperatures vary throug out the growth and melt back of the chill layer show similar good agreement, since the predicted mean temperature of the wall always lies between the measured temperatures of the inner and outer surfaces of the probe.

The curves for the growth and melt back of the chill layer in the presence of superheat are all based on a complicated conduction/ convection model for heat flow in the liquid metal. This model, and its development are discussed in the next Section.

7.2.4 The conduction/convection model for heat flow in the liquid metal

Figure 39 shows some theoretical curves predicted by Brooks on the assumption that heat transfer from the liquid metal to the growing and then melting chill layer could be described in terms of a constant heat transfer coefficient. Brook's curves are slightly in error because he used equations describing solidification onto a plain wall and not onto a cylindrical hollow probe, but the discrepancy between the theoretical and experimental curves is very great indeed. It is obviously due to an incorrect model for heat transfer in the liquid metal. The overall heat balance on the solidification and melt back process is more or less correctly predicted since the theoretical amount of heat absorbed by the probe wall and the total melt back time predicted theoretically can be arranged to equal that measured experimentally by choice of suitable values of the liquid heat transfer coefficient. The shapes of the experimental and theoretical growth and melt back curves, however, are entirely different and it is apparent that the heat transfer coefficient that predicts a correct melt back time provides too little heat during the early stages of solidification and too much heat during the later stages. The flow of heat from the liquid metal to the solidification front is incorrectly distributed throughout the growth and melt back time.

The cold rotating probe is suddenly immersed into the liquid eutectic bath which at that time is stationary. The liquid metal in contact with the probe will cool rapidly giving up its heat to the probe and a layer of cooled liquid will form around the probe growing outwards from the probe surface. At the same time, the liquid metal in contact with the probe will start to rotate with the probe, and a layer of circulating liquid will grow out from the surface of the probe.

o 68 r.p.m.

ooo

FIGURE 59

Chill Layer' Thickness vs. Exposure Time. Eutectic sn-pb.2o°c superheat,pb insert.

The rate at which the layer of cooled liquid will grow is determined by the value of the thermal diffusivity,and the rate at which the layer of circulating liquid will grow is determined by the kinematic viscosity, the ratio of the kinematic viscosity to the thermal diffusivity being termed the Prandtl number. Prandtl numbers for liquid metals are always considerably less than one because of the high contribution to the thermal conductivity made by the electrons in the liquid metal. Thus the layer of cooled liquid grows much more rapidly than the layer of moving liquid. The initial growth of the cooled liquid layer is controlled by conduction, and it is conduction that is the mechanism whereby this layer gives up its heat to the probe surface.

For these reasons, a model for heat transfer in the liquid metal was developed in which a layer of chilled metal grew outwards from the probe, giving up its sensible heat to the probe by conduction. Figure 40 shows theoretical curves predicted on this basis for liquid metal temperatures of 180°C and 220°C compared with the experimental results measured at those temperatures.

The figure shows that this model for heat transfer in the liquid metal predicts chill layer thicknesses that agree very well with the measured values during the initial stages of solidification. After some 5 seconds, however, the theoretical results start to diverge from the measured values giving increasingly greater thicknesses.

_Obviously_the model involving a growing conduction layer predicts much higher heat fluxes from the liquid to the solidification front than the model based on a constant heat flow - the temperature gradiants at the front are very high indeed being initially infinite. These heat fluxes inhibit the growth of the solidification layer at a time when the high temperature gradients in the probe confer on it

FIGURE 40 Chill-layer thickness versus Time (pure conduction model)

its greatest ability to absorb heat. Thus the heat transfer model based on the growing conduction layer predicts lower initial solidification rates than the model based on the constant heat transfer coefficient.

After the initial soldification process however, the thicknesses predicted by the conduction layer model are greater than the measured values - the model is predicting heat fluxes from the liquid metal that are too low. To see why this is, we must again consider the process occurring in the liquid around the probe. The growing conduction layer is followed by a growing layer c£ circulating liquid. At some stage the velocity of this circulating liquid will be sufficient to exceed the criterion for the formation of Taylor vortices. Once these vortices are formed, they will immediately stir up the liquid and destroy the conduction layer increasing very significantly the heat flux to the solidification front. It is for this reason that the measured thickness soon start to fall below those predicted by the model based on the existence of the conduction layer.

Examination of the measured of chill layer thicknesses shown in Figures 40 and 23 for 3°C of superheat (0^ = 186) show that the rate of melt back tends to a constant value. A straight line drawn through the measured values has a slope of -8.2 x 10-^ cm/s. A simple heat balance of the layer of melting metal shows that this constant slope • indicates that there is a constant heat flux from the liquid metal to the surface of the probe. By this stage in the solidification and melt-back process, the temperature difference across the interface between the probe and the chill layer will have become negligibly small - the chill layer is effectively insulated. A heat balance thus shows:

$$q_s = \rho H \frac{dt}{AT} \quad (124)$$

The constant heat flux from the liquid can be described in terms of a

constant heat transfer coefficient:

s $h_{"XIQ}$ (125)

Thus the value of this heat transfer coefficient can be determined from the slope measured from figures 23 and 40*

(126)

$$(QT - 0_s)$$

Substituting the measured value of the slope into this equation gives:

(127)

Thus examination of the theoretical and experimental curves shown in Figure 40 shows that a conduction layer grows initially in the liquid but is then disturbed by the developing convection currents. These convection currents eventually give rise to a boundary layer whose thickness corresponds to the heat transfer coefficient value given in equation 126.

The exact mechanism whereby the conduction layer is disturbed and the convection layer established is extremely complicated. If it could be analysed, any such analysis is certainly beyond the scope of this work. The simple approach described in Section 3»3*3 in terms of the half life of the process is the best approach that can be developed. The value of the halflife has been found by trial and error. Figure 41 shows theoretical curves predicted for halflifes of 2.5* 5 and 6 seconds. The best agreement is obtained when the half life is chosen as 6 seconds, and it is this value that has been used throughout this work for all predictions made when the probe speed is 60 r.p.m.

The theoretical curves shown in Figures 23 to 29 all show very good agreement with the experimentally measured thicknesses. This agreement serves as justification for the appropriateness of the liquid metal heat transfer model proposed in this work. Further evidence for its appropriateness is provided by Figure *A2*

O

I-r

-p

•H

LO

•H

O

i!

I-i

•H

Ju

I-i

•H
-P

O

•H
-P

I-i

H

O

Figure 42 shows results obtained by Brooks for the growth and melt back of a chill layer of lead/tin eutectic on a stainless steel probe, rotated at 68 r.p.m. and at 200 r.p.m. The theoretical curve at 68 r.p.m. has been obtained using the liquid heat transfer coefficient and the half-life of the decay process used in obtaining the previous curves at 60 r.p.m. The curve at 200 r.p.m. has been obtained using the following values:

$$= 17000\ V/i$$

$$?"_{i_2} = 3 \text{ seconds}$$

This value of the heat transfer coefficient has been obtained from the value at 60 r.p.m. on the assumption that the coefficient is proportional to $(Re)^{0.7}$. The value of $T \pm$ has been obtained by assuming that the time taken to establish the Taylor vortices will be reduced as the speed of rotation of the probe is increased, following a similar power law.

FIGURE 42 Chill-layer thickness versus time curves. Stainless steel probe; Pb - Sn eutectic bath (30°C superheat)

7.5 Dissolution of lead, tin and lead/tin alloys in molten lead/tin eutectic

7.3.1 Mechanism of the Dissolution Process

Whenever a solid is dissolved in a liquid, the question is raised as to whether the dissolution step is controlled by mass transfer in the liquid, or by the actual dissolution step at the solid/liquid interface. As pointed out in Section 2.4.3» a number of workers have investigated the dissolution of solid metals in liquid metals using the rotating cylinder geometry used in this work. In the main, these workers have concluded that the processes are mass transfer controlled because their rate increases as the speed of rotation inceases. Lommel and Chalmers ^ , however, concluded that dissolution of lead in lead/tin eutectic was surface controlled.

The experiments on the rate at which lead, tin and lead/tin alloys dissolve in lead/tin eutectic reported here allow the mechanism of the dissolution process to be investigated. The results of the experiments show quite clearly that the dissolution process is controlled by mass transfer in the liquid metal and not by any effect at the dissolution interface. The separate items of evidence for this conclusion are discussed in the subsequent sections.

7.3*2 Effect of grain size, orientation and grain boundaries

If the dissolution of a metal is controlled by the actual dissolution step at the surface, it will be dependent on differences in the orientation of individual grains to the surface. The dissolution interface will take on an uneven shape as different grains are attacked to different extents. Dissolution will also occur more rapidly at grain boundaries than in the middle of grains, further contributing to the uneveness of the dissolution surface. The external appearances

of the probes shown in the Plates 12 - 17 show a very uneven attack which suggests surface control. For this reason, the micrographs shown in Plates 18 to 26 were prepared to allow investigation of any relationship that might exist between the irregularities in the surface, and the grain size of the dissolving probe. The micrographs of pure lead and tin (Plates 18 to 21 and 26) show that the irregularities in the shape of the surface are not dependent on the grain size or the orientation of individual grains. Thus the irregular shape of the dissolution interface is not an indication that the dissolution of lead, tin or lead/tin alloy is controlled by the surface dissolution step. As the next section shows the irregularities are directly related to mass transfer in the liquid phase.

The micrographs of the lead/tin alloys, which were obtained after much shorter exposure times and are presented at a greater magnification, show that the prime attack was on the inter-dcndritic eutectic metal. The upper micrograph of Plate 25 being a particularly clear illustration of this. It is not surprising that the inter-dendritic metal was attacked preferentially because it merely has to melt off into the eutectic bath. Indeed, in the highly alloyed probes, the attack was so extensive that large regions in the probe melted, and the probe disintegrated. Plate 23 represents two micrographs which illustrate how areas with a high fraction of eutectic could be very rapidly attacked.

7.3*3 Morphology of the dissolution interface and fluid flow

The previous section has shown that the uneven shape of the surfaces of the probes after dissolution is not related to the grain structure of the probes. Close examination of the morphology shows, in fact, that it is related to the flow patterns in the eutectic bath.

Plate 11 shows a lead probe after it has been immersed, in the

eutectic bath but not rotated. It can be seen that the surface shows vertical grooves broken up by random attack in places. Molten lead is denser than the lead tin eutectic so that the lead saturated layers of liquid close to the probe will be denser than the bulk of the liquid eutectic. Thus concentration driven natural convection currents will be set up leading to a vertical flow down the probe. It is this downwards flow that results in the vertical grooves, the regions of irregularities correspond to regions of turbulence in the natural convection flow.

Plates 12 and 13 show respectively lead and tin probes that have been rotated at 41 and 60 rpm during dissolution. They both show fairly continuous tangential grooves regularly spaced along their lengths. ghe^4^ Taylor numbers corresponding to these speed of rotation are f= x n4 / (41 ~ x i whereas the Taylor number that corresponds to the breakdown of Coutte flow and the formation of Taylor vortices is 1571 • Thus one would expect Taylor vortices to be well established in the liquid melt around the two probes shown in Plates *12* and *13* •

Figure 43 has been taken from the work of Taylor and shows in the left hand sketch Taylor vortices as he observed them. The similarity between this sketch and the two Plates is striking, and it is apparent that the grooves shown in the Plates are formed by the Taylor vortices, increased attack occurring where the vortex flow is inwards towards the probe surface. The morphology of the probe surface does provide, in fact, a permanent impression of the fluid motion around the probe.

Plate 15 shows **a** tin probe that has been rotated at 60 r.p.m. The impression of the tangential grooves formed by the vortices still remains although it has been severely distorted. The right hand sketch

FIGURE 43

Braking of Taylor vortices at high rotation speeds [31]

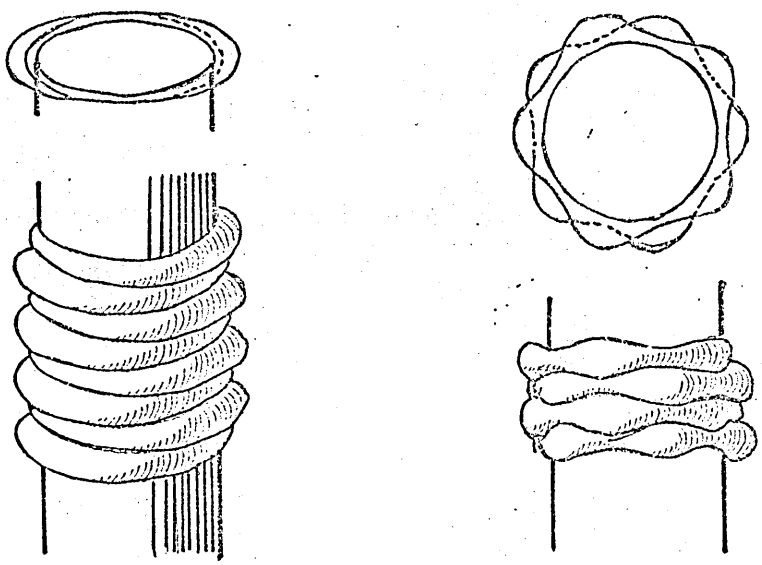

in Taylor's figure shows how the Taylor vortices become distorted as the speed of rotation is increased and the vortices start to break up. Once again, a strong similarity exists between Plate 15 and the sketch. It is apparent that the morphology of the probe's surface shown in this Plate is again providing a permanent record of the fluid flow - this time of the break up of the Taylor vortices.

Increased distortion of the vortex flow is apparent in Plate 17 which shows a lead probe that had been rotated at 60 r.p.m. and vibrated during dissolution. In this case, it is the vibration that is further disturbing the stable vortex flow.

At higher speeds, the vortices break up cumpletely, and the entire fluid flow regime becomes turbulent. Random turbulent eddies exist over the entire surface of the probe and give rise to the completely random erosion pattern shown in Plate 16^which shows a probe that has been rotated at 120 r.p.m. during dissolution.

Thus the surface morphologies resulting from the irregular dissolution of lead and tin probes do not indicate uneven attack on different grains due to a surface controlled reaction. The morphologies are, in fact, directly related to the flow patterns existing in the liquid during dissolution, and are a definite indication that the dissolution process is controlled by mass transfer in the liquid. So much is this so that the morphologies of the dissolved surfaces form a permanent impression of the fluid flow patterns existing in the liquid during dissolution.

7.3•4 Effect of rotation speed on dissolution rates

By far the most important evidence for the conclusion that the dissolution of lead, tin and lead/tin alloys in lead/tin eutectic is

mass transfer controlled is contained in Figure 37 * This Figure shows mass transfer coefficients calculated from the dissolution rates measured in this work, plotted together with curves calculated from the correlations of Eisenberg, Tobias and Wilke [46] and Kosaka and Minowa 55 • These +i"C correlations have been based on extensive investigations into mass transfer rates of rotating cylinders involving a wide range of different systems. It can be seen that the coefficients obtained from this work fall very close to and mainly between the two curves. It can thus be concluded that the dissolution processes studies in this work are mass transfer controlled®

.5 Comparison with previous work

As stated earlier, the majority of workers who have studied the dissolution of solid metals in liquid metals have reached the same conclusion as in this work - that the dissolution process is mass transfer controlled in the liquid metal. The one notable exception is Lommel and Chalmers [51] who concluded that the dissolution of lead in lead/tin eutectic was surface controlled.

Examination of reference 51? however, show why these authors came to a mistaken conclusion. They immersed lead rods 0. 63 cm in diameter into a eutectic lead/tin bath that was additionally stirred by a large impeller rotating at a constant speed. They found that the rate at which the rod dissolved was not dependent on the rate at which it was rotated. They also observed uneven attack on the surface of the probe - describing the uneveness as 'etching11 They did not, however, examine metallographically whether or not the uneveness was related in any way to the grain structure of the rods.

• It is apparent that the stirring effect produced by rotating the small rod will be very much less than that produced by the large

impeller. Any effect on mass transfer rates to the rod's surface, and therefore on dissolution rates, produced by varying the speed at which the rod was rotated would be swamped in the overall effect produced by the impeller in the bath.

The 'etching* effect that Lommel and Chalmers report as providing further evidence that the dissolution is surfs.ce controlled is nothing more or less than the effect of turbulence and fluid flow discussed in Section 7«2.3« Had Lommel and Chalmers been able to obtain micrographs of their probes after dissolution, they would have seen this to be the case.

7.4 Accuracy of comparison between the theory and the experiments.

7.4*1 Heat losses during chill-layer experiments

A considerable amount of heat was conducted longitudinally along the cylinder to the portion of the probe which was not immersed into the bath. The heat which escaped from the inner surface of the probe was negligable compared with other heat losses.

Starting the experiments 1-1.3°Cabove selected experimental temperature provided the extra heat required during the first 4 - 10 seconds of most of the experiments necessary to balance the sudden heat losses caused by lowering the cold probe (room temperature) into the bath. The ensuing 0.8 - 1.3°C drop in the bath temperature was recovered by the thermal heater in approximately 8 - 14 seconds, the heater being switched on as soon as the experiment started. After the first 3 - 4 experiments full experience was gained in keeping the temperature in the range + 1°C of selected temperatures.

The extra material at the bottom of the probes and the heat lost from top of the probes caused accumulation of extra chill layer around these areas. As a result of this, meltback of the chi11-layer took longer in these areas than it did in the remainder of the probe.

S

Figure (44) illustrates diagramatically the typical shape of an initial chill-layer growing on the substrate, and its subsequent meltback.

FIGURE 44

Typical shapes of chill-layer diri ng growth and meltback

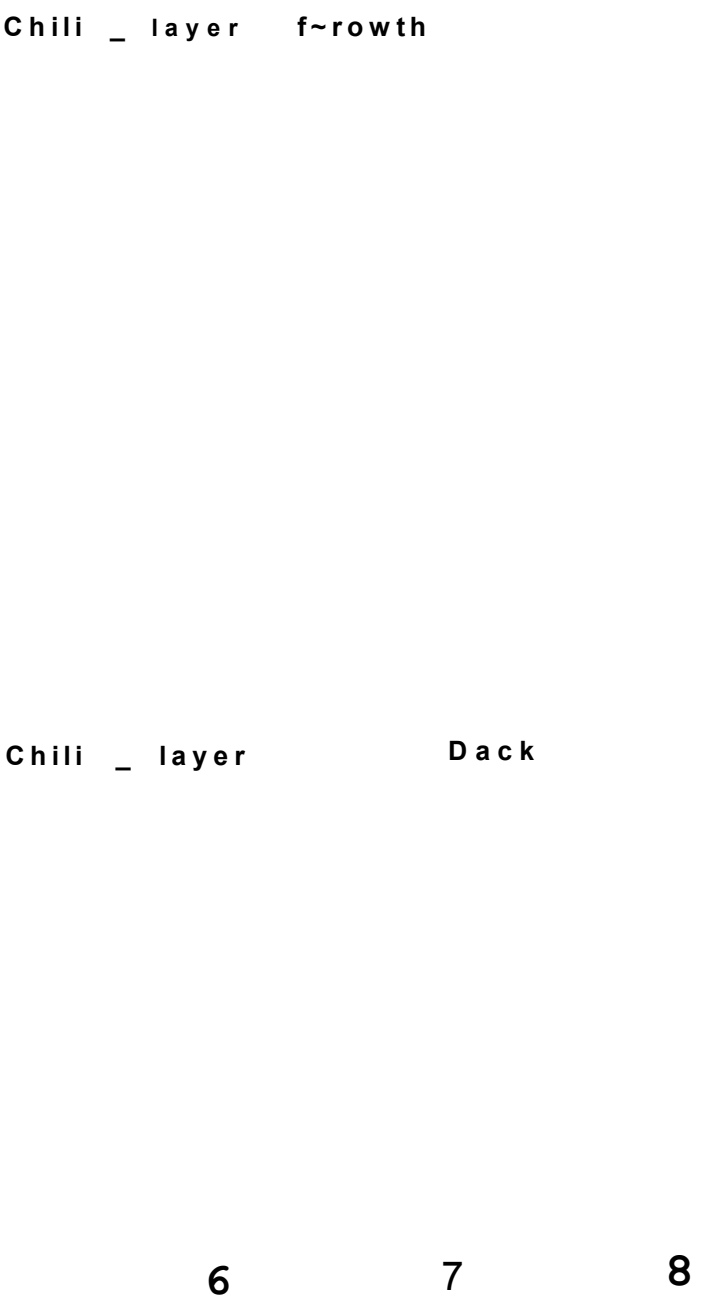

Exploratory experiments showed that surface heat losses caused a cold layer to exist at the surface of the bath, this layer growing after the halt of stirring. But when the probe remained static and the bath was not stirred, the temperature difference between this layer and the bulk of the liquid was never greater than 2°C. Further, this layer did not extend more than 3 cm below the surface. This was measured with a thermocouple tip being bent at a 90 angle so that it could lie in the plane of the isothermals, and conduction from the probe tip was minimised. During rotation of the probe the extent of this layer was reduced to about cm below the surface, thus being situated well above the main reading area.

7.4»2 The accuracy of the theory

7.4.2.1 Heat transfer phenomenon

Predictions made using the integral profile method for heat transfer during cylindrical solidification have already been compared with the experimental results in sections
These experiments were conducted using lead probes and Pb-Sn eutectic bath. Good agreement between experiments and theory was achieved.

The errors between successive integrations were always preset at a half a step length before the computation, and as the entire method relied on an original heat balance applied to each section in turn, the largest uncertaintity was in the physical data.

As a result of this the theoretical final temperatures with tin-lead systems after prolonged exposure were only 1 - 1.4°C greater than expected. The liquid and interface heat transfer coefficients were determined by trial and error during computing. Due to the random nature of this "trial-and-error" technique, the accuracy of these

values was hard to assess; this being, due in part to different combinations of the variables giving numerically similar answers.

7*4*2.2 Dissolution

The experimental results agreed well with the theoretical results forecast by combination of the Thomas-Eisemberg relationship and the theory developed here for mass transfer controlled dissolution.

The power dependence (n) of 0.7 for dissolution rate was found to be linear between the speeds 40 - 120 r.p.m. for all experiments, when the results were plotted on a log-log basis. There was a slight positive deviation of the experimental results from linearity at lower speeds.

At lower speeds, it is thought that the power dependence (n) decreases slowly with decreasing speed, until it reaches a value corresponding to that for natural correction.

7*4*3 Errors of Measurement

7.4*3*1 Thickness

Each individual micrometer measurement was in error by less than 0.02 mm, which is reduced to negligible proportions by averaging.

7.4*3*2 Time

The static exposure time, measured by stop watch, had an uncertainty of 0.4 seconds which was between^4 and ^0.4 of the total exposure time. As the speeds of the monitoring recorders were preset and the starting and finishing of experiments were marked with the event marker it was possible to recheck the exposure time values from the charts of the recorders.

The difficulty in measuring melt-back' time was mostly a matter of judgment. For this reason the main reading area from several experiments was observed after removing the probe from the liquid in order to assess melt-back.

The real exposure times for chill-layer experiments are found by adding the static time to the two travelling times of that particular measurement.

This difference changed between 2 ~ 4 seconds for a 4 cm wide area starting 4 cm above the bottom of the probe (the main reading area). During the dissolution experiments, as the mainreading area was represented by the whole portion of the exposed probe the dissolution time was found by substracting the corresponding melt-back times from the appropriate exposure time.

7.4*3*3 Temperature

Although the thermocouples measuring the wall-end temperatures were bent through 90°, in order that the final 10 mm of their length lay in the plane of the isotherms in the probe wall, thus removing errors due to conduction, some conduction losses occurred to an unknown extend by movement of the thermocouple tip during casting.

It is believed that movement of the thermocouple tip caused the recorded temperature to fall below the predicted values when the limiting values were approached.

The sliprings which conducted the e.m.f. from the inside and outside wall thermocouples indicated no error when rotating cold.

7.4.3.4 Additional possible sources of measurements

1 Inaccurate reading of some physical data.

2 Error in weighting of the probes.

3 The excentricity of the probe.

4 The possibility of an increased surface area of the probe.

5 The recorder readings.

The magnitude of these errors was small compared with the previously mentioned errors consequently their combined effect upon the accuracy of the results is thought to be negligible.

CONCLUSIONS

The growth and melt' hack of the chill layer formed when a solid metal is immersed in a liquid metal can be predicted accurately by the integral profile method provided appropriate values of the interface heat transfer coefficient can be ascertained, and the heat transfer process in the liquid metal is understood.

The values of interface heat transfer coefficients that are used in the theory in order to obtain agreement with experiments are similar to those quoted in the literature[57].

The heat transfer process that takes place in a superheated liquid metal is a complicated combination of unsteady conduction and developing convection, but it can be analysed in terms of a single model involving the growth of a conduction layer and its subsequent decay to form a steady convective boundary layer.

The dissolution of lead, tin and certain of their alloys in liquid lead/tin eutectic is controlled by mass transfer. The mass transfer process is dominated by natural convection when the speciman is stationary and by forced convection when the specimen is rotated.

The shape of dissolution interface can be very irregular since it forms an impression of the flow patterns in the liquid.

The conditions for solidification cladding can be predicted from heat and mass transfer considerations.

APPENDIX 1

An attempt to grow a bonded layer

Brooks has concluded that it is possible to bond two dissimilar metals by a process which entails controlled surface dissolution of the piece which is to be clad prior to the deposition of the clad layer by solidification.

The present work investigated the phenomena occurring both prior to and during surface dissolution of the probe which was to be clad.

The theory developed during the course of this work successfully described the heat transfer processes occurring during chill-layer growth, melt-back and surface dissolution, of a probe whose composition may be that of a pure metal or an alloy.

The experimental work and theoretical considerations examined during the course of this work enabled us to make predictions as to what pre-cladding conditions should exist within the probe. In fact the theory was developed in such a manner so as to enable the ready grafting into a unified theory which allows not only for the growth of the chill-layer, melt-back and surface dissolution, but also for the growth of a clad layer of a dissimilar metal.

Although no actual cladding experiments were carried out, a series of computations were completed in which clad layer thicknesses were predicted using the previously described theory to establish pre-cladding conditions.

The precladding conditions may be summarised essentially by saying that they allowed for 1 mm of dissolution once meltback was completed.

The results of these computations have been summarised in Figure 45 which shows two curves for $3^{o}C$ superheat and $12^{o}C$ superheat respectively.

Once 1 mm of probe dissolution had been allowed for, a high cooling rate was artificially created within the probe. This is achieved by putting a high heat transfer coefficient (for the heat transfer between the wall and the cooling medium) into the main program of computations which when entered the loop resulted in the growth of a clad layer.

theoretical curves of chill-layer growth, meltback, dissolution and cladding at 186 and

APPENDIX 2

TABLES OF EXPERIMENTAL CHILL-LAYER RESULTS »

TABLE 1

Experimental "chill-layer thickness" results for "zero" superheat

(Bath temperature: 183.0°C)

(Probe Rotation speed: 60 r.p.m.)

Exposure Time (sec)	Measured chill-layer thickness (mm)	Exposure Time (sec)	Measured chill-layer thickness (mm)
7.5	3.06	30	5.40
7.5	2.86	30	5.55
7.5	3.4	30	5.95
12.5	3.69	41	6.36
12	3.7	40.5	5.85
12	3.5	40	5.8
15	4.06	60	6.4
15	4.2	60	6.2
15	4.6	60	6.7
20	5.29	100	6.
20.5	4.81	100	6.75
20	4.60		
		120	7.09
		120	7.11

TABLE 2

Experimental "Chill-layer thickness" results for "3°C" superheat.

Bath temperature = 186°C

Probe rotation speed = 60 r.p.m.

Exposure Time (sec)	Measured chill-layer thickness (mm)	Exposure Time (sec)	Measured Chill-layer thickness (mm)
5	2.81	50	4.35
5	2.51	50	4.05
10	3.2	55	3.65
10	3.61	60	3.25
10	4.09	60	3.38
15	4.9	70	2.26
15	4.5	70	2.71
20	4.7	75	2.03
20	4.85	75	2.15
20	5.25	75	2.09
25	4.75	80	1.50
25	5.10	80	1.62
30	4.76	90	1.01
30	4.81	90	0.82
40	4.45	100	0.25
40	4.67	100	0.18

Comment: With probe exposure times of 110 and 115 seconds examination of the probe surface revealed the presence of slight spiral patches of remnant chill-layer material around the main reading area. At an exposure time of 125 seconds, all such phenomena had disappeared, the probe surface being clear.

TABLE 3

Experimental "chill-layer thickness" results for "7°C" superheat.

Bath temperature: 190°C

Probe rotation speed: 60 r.p.m.

Exposure Time (sec)	Measured chill-layer thickness (mm)	Exposure Time (sec)	Measured chill-layer thickness (mm)
	2.89	25	3.03
	3.41	25	3.15
	2.80	25	3.25
10	3.65	30	2.51
10	4.01	30	2.77
10	4.25	30	3.06
15	4.29	35	1.25
15	3.98	35	1.43
15	3.80	35	1.69
20	4.04	40	1.15
20	4.08	40	0.82
20	3.78	40	0.74

Comment:

With probe exposure time of 45 seconds examination of the probe surface revealed the presence of slight spiral patches of remnant of chill-layer material around the main reading area of the probe. At an exposure time of 55 seconds, all such phenomena had disappeared.

TABLE 4

Experimental "chill-layer thickness" results for "12°C" superheat.

Bath temperature: 195°C

Probe rotation speed: 60 r.p.m.

Exposure Time (sec)	Measured chill-layer thickness (mm)	Exposure Time (sec)	Measured chill-layer thickness (mm)
4	2.15	15	3.4
4	2.01	15	3.25
4	2.17	15	3.6
6	2.25	20	2.75
6	2.84	20	2.25
6	2.75	20	2.23
10	3.10	25	1.43
10	3.04	25	1.54
10	3.25	25	1.98

Comment:

With probe exposure time of 30 seconds examination of the probe surface revealed the presence of slight spiral patches of remnant chill-layer material around the main reading area of the probe. At an exposure time of 35 seconds, all such phenomena had disappeared the probe surface being clear.

TABLE 5

Experimental "chill-layer thickness" results for "17°C" superheat.

Bath temperature: 200°C

Probe rotation speed: 60 r.p.m.

Exposure Time (sec)	Measured chill-layer thickness (mm)	Exposure Time (sec)	Measured chill-layer thickness (mm)
5	2.45	20	1.78
5	2.56	20	1.88
5	2.20	20	1.91
10	2.80	22	1.01
10	2.82	22	0.98
10	2.67	22	0.89
15	2.54	26	clear
15	2.63	26	clear
15	2.60		

TABLE 6

Experimental "chill-layer thickness" results for "27°C" superheat.

Bath temperature: 210°C

Probe rotation speed: 60 r.p.m.

Exposure Time (sec)	Measured chill-layer thickness (mm)	Exposure Time (sec)	Measured chill-layer thickness (mm)
3	1.125	10	1.82
3	0.92	10	1.93
3	0.93	10	1.91
6	2.08	13	1.17
6	1.91	13	1.11
6	1.78	13	1.28

Comment:

With probe exposure times of 16 and 18 seconds examination of the probe surface revealed the presence of spiral patches of remnant chill-layer material around the main reading area of the probe.

At an exposure time of 18 seconds, all such phenomena had disappeared.

TABLE 7

Experimental results of "chill-layer thickness" for "37°C superheat.

Bath temperature: 220°C

Probe rotation speed: 60 r.p.m.

Exposure Time (sec)	Measured chill-layer thickness (mm)	Exposure Time (sec)	Measured chill-layer thickness (mm)
5	1.04	12	0.62
5	0.98	12	0.60
5	1.25	12	0.51
8	1.42	15	0.01
8	1.38	15	0.03
8	1.21	15	0.
		17	Clear

TABLE 8

Experimental "chill-layer thickness" results for "47°C, 57°C and 67°C" superheats.

Probe rotation speed 60 r.p.m.

Bath Temperature (°C)	Exposure Time (sec)	Measured chill-layer thickness (mm)
230°	5	0.26
	5	0.267
	5	0.195
	8	0.11
		0.14
	10	patches
	10	
	12	clear
240°	4	0.1
	4	0.12
	8	clear
250°	4	clear
	4	clear

APPENDIX 3

TABLES OF EXPERIMENTAL DISSOLUTION RESULTS

TABLE 10

Dissolution Rates of Pure Lead probes in Lead-Tin eutectic Baths.

Rotation speed: 30 r.p.m. Meltback time: 18 secs.

Bath Temp. (^{o}C)	Dissolution Time (s)	Dissolution Rate $N \times 10^{3}$ $(g/cm^{2}.s)$
230	80	6.12
	80	6.25
	120	6.21
	120	6.38
	160	6.43
	160	6.29
	160	6.35

TABLE 11

Dissolution rates of static pure lead probes in Pb - Sn eutectic baths.

Meltback time: 20 secs.

Bath Temp. (°C)	Dissolution Time (s)	Dissolution Rate $\frac{N \times 10^3}{(g/cm^2.s)}$
230	60	4.58
	60	4.67
	120	4.59
	120	5.01
	180	5.10
	180	5.9

TABLE 12

Dissolution rates of pure lead probes in Lead-Tin eutectic bath at different temperatures.

Rotation Speed: 60 r.p.m.

Meltback Time (s)	Bath Temp. (C)	Dissolution Time (s)	Dissolution Rate ($g/cm^2.sec.$)
26	200	60	2.01
			2.08
		120	2.11
			2.18
		160	2.21
			2.17
18	220	100	5.25
			5.31
		140	5.33
			5.39
		160	5.29
			5.30
13	230	80	8.72
			8.74
			8.73
		140	8.83
			8.80
			8.84
		160	8.8[illegible]
			8.84
		200	8.87
			8.89
			8.85
		240	8.68
			8.73
			8.75
35	250	60	14.35
			14.39
			14.38
		120	14.43
			14.49
			14.52
		180	14.73
			14.82
			14.84
		240	14.37
			14.28

TABLE 13

Dissolution rates of pure lead probes in Pb-Sn eutectic baths.

Rotation Speed: 120 r.p.m.

Meltback Time (s)	Bath Temp. (°C)	Dissolution Time (s)	Dissolution Rate $N \times 10^{-3}$ ($g/cm^2.s$)
15	230	120	14.4
		120	14.6
		180	14.24
		180	14.90
		240	14.55
		240	14.80
		300	15.32
		300	15.98
	250	60	23.31
		60	23.11
		120	23.39
		120	25.43
		120	25.18
		180	26.65
		180	26.48

TABLE 14

Dissolution rates of 90% lead 10% tin probes in lead-tin eutectic baths.

1 Rotation Speed: 50 r.p.m. Meltback time: 15 s

Bath Temp. (°C)	Time (s)	Dissolution Rate $N \times 10^3$ $(g/cm^2.s)$
230	60	8.2
	60	8.35
	100	8.51
	100	8.62
	160	8.92
	160	8.86

2 Rotation Speed: 100 r.p.m. Meltback time: 10 s

Bath Temp. (°C)	Time (s)	Dissolution Rate $N \times 10^3$ $(g/cm^2.s)$
230	60	13.62
	60	13.81
	100	14.1
	100	14.39
	160	14.70
	160	14.96

TABLE 15

Dissolution rates of pure tin probes in Lead-Tin eutectic bath.

Rotation Speed W (r.p.m.)	V (cm/s)	Time (s)	Dissolution Rate: N x 10^3 (g/cm^2. sec)
		75	5.69
		75	5.58
30	9.72		
		120	5.40
		120	5.31
		180	5.91
		180	5.95
		60	6.68
		60	6.83
41	13.29		
		180	6.63
		180	6.99

The bath temperature for all above experiments was 200°C.

TABLE 16

Dissolution rates of pure tin probes in Lead-Tin eutectic bath.

Rotation Speed W (r.p.m.)	V (cm/s)	Dissolution Time: (s)	Dissolution Rate: N x 10^3 (g/cm .s)	Meltback Time
		105	9.61	
		105	9.46	
60	19.45	120	9.56	29
		120	9.68	
		180	9.93	
		180	9.81	
		60	15.25	
		60	15.31	
120	38.9	100	15.43	18
		100	15.52	
		150	15.91	
		150	16.05	

Bath temperature for all the above experiments was 200°C.

APPENDIX 4

Analysis of Materials and Specification of Materials Used

			%
LEAD	Commercial Purity	Pb	99.948
		Cu	0.0050
		Fe	0.0114
		Mg	0.00025
		Zn	0.0002
		Sn	0.0050
		Ag	0.0002
		Sb	0.020
		Bi	0.010
Tin	Commercial Purity	Sn	99.89
		Pb	0.0310
		Cu	0.0292
		Fe	0.0113
		As	0.0281
		Sb	0.010

APPENDIX 5

Physical and thermal properties of Pb, Sn, and Pb - Sn eutectic and stainless steel.

H	36826	J/kg	
θ_s	183	^oC	Liquid Pb - Sn
C_L	217.36	J/kg^oC	Eutectic
k_L	28.57	W/m^oC	
$_L$	8010	Kg/m^3	
230°C	0.0226	Poise	
250°C	0.0215	Poise	
C_s	217	J/kg C	Solid Pb - Sn
k_s	52	W/m^oC	Eutectic
$_s$	8300	kg/m^3	
C_{Pb}	130	J/kg C	
			Solid Pb
$_{Pb}$	11300	kg/m^3	
k_{Pb}	31	W/m^oC	
$_{Sn}$	7290	kg/m^3	Solid tin
C_{Sn}	225	J/kg	
C_{St}	523	J/kg	
k_{St}	17.28	W/m^oC	Solid stainless steel
$_{St}$	7900	kg/m^3	

System	W(r.p.m.)	HO(W/m^2C)	HL(W/m^2C)	$\tau_{1/2(s)}$	$\tau_{c(s)}$
Pb - Probe					
Pb-Sn Eutectic bath	60	2500	8500	6	5
Stainless-Probe					
Pb-Sn Eutectic bath	68	3135	8500	6	5
	200	3135	17000	3	5

NOMENCLATURE

Variable	Description	Dimension
	Gap between rotating cylinders	cm
	Specific heat	j/kg°C
	Mass concentration	kg/u?
	•Mass fraction of metal A in bina.ry alloy of metals A and B	
$*_B$	Mass fraction of metal B in binary alloy of metals A and B	
H	Latent Heat	J/kg
h	Heat transfer coefficient	w/m2°C
k	Mass transfer coefficient	cm/sec
k	Thermal conductivity	w/m°C
n_i	Mass flux	gr/cm2 sec
N	Initial mass transfer rate	gr/cm2.sec
	Initial heat flux ($_v = h_o 0_s$)	w/m^2. sec
$_o$	heat flux	w/m^2. sec
R,r	radius	cm
Ta	See eq. 36	
Ta	See eq. 37	
V	peripheral velocity	cm/sec.
r	Time	sec.
S I	Angular velocity	rad/sec.
p_i	Density	kg/u?
0	Temperature	
ol_{AB}	Mass transfer coefficient	cm/sec.
/	kinematic viscosity	cm^2/sec.
F	viscosity	g/cm. sec.
f l	Functional expression defined by Eq. 67	
A	Functional expression defined by Eq. 68	

NOMENCLATURE (continued)

Variable	Description	Dimension
Γ	Functional expression defined by Eq. 69	
f'_0	See equation 82	
f'	See equation 84	
δ	Boundary layer thickness (diffusion)	cm
HO	Interface heat transfer coefficient	W/m^2C
HL	Liquid heat transfer coefficient	W/m^2C

DIMENSIONLESS VARIABLES

N_{Nu} (Nu)	Nusselts' number
N_{Re} (Re)	Reynolds' number
N_{Gr}	Grashofs' number
Pr	Prandl's number
$N_{Nu.cond}$	Nusselts' number for conduction
N_{Sc}	Schmids number
t^*	See eq. 10
θ^*	See eq. 11
H^*	See eq. 13
h^*	$h^* = h/h_o$
k^*	$k^* = k/k_s$
q^*_t	See eq. 15
q^*_o	See eq. 14
T^*, (N_{Ta})	modified Taylor number See eq. 38
γ^*	thermal capacity $\gamma^* = \frac{\gamma_w}{\gamma_s} = \rho.c.$
f'^*	See eq. 45
$f'\theta^*$	See eq. 44
ε	See eq. 12
Ω^*	Functional expression defined by equation 42
Γ^*	" " " " 42.1
Λ^*	" " " " 43

SUBSCRIPTS

A	Air
1	Inner
2	Outer
1/2	half life
b	value in bulk liquid phase
c	conduction layer growth
i	value at solidification interface (mass transfer)
L	value on Liquidus Line (mass transfer)
L,LIQ	Liquid metal
LIM	Limiting value
iw	inside wall of the probe
m	mean
ow	outside wall of the probe
r	value at inner probe wall
s	solidifying metal
t	value at solidification front (heat transfer)
0	initial value or value at solid-solid interface (probe-growing layer)
eff	effective value (see eq. 73, 74)

T. Shephard, and M. G. Brooks	Metalurgia. Oct. 1969. p.145
D. R. Brov/n and A. E. Jackson	Sheet Metal Ind. 1962. 22, p.249
W. Bullough	Iron Steel Inst. 19^7* 205* p.6
G. Sugano, K. Mori and 'K. Inoue	Eletrochem Tech. 1968. 6, p.526
W. N. Jenkins	Met. Fin. Jnl. 1966. 12, p.160
W. N. Jenkins	Sheet Met. Ind. 1968. 42? p.329
M. G. Brooks	Ph.D. Thesis. 1973* University of London
V. Kondic	Metallurgical Principles of Founding. 1968. p.102
H. G. Landau	Quart. Applied Maths. 1950* 2* p.81
C. A. Forster	English Electric Co. Ltd. 1954* Report L
A. W. L. Hills	T.M.S., A.I.M.E. 1969. 242, P-1471
K. Pohlhausen	Zeitschrift fiir Angewandte Mathematik und Mechanic. 1921. 1, p.252
T. R. Goodman	T.M.S., A.I.M.E. 1958. 80, p.335
T. R. Goodman	Jnl. of Aeoro Space Sciences. 1959• 26, p.187
T. R. Goodman and J. J. Sheq	Jnl. of Appl. Mech. i960. 27, p.16
T• R. Goodman	ASMS Paper Ho. 6O-SA-9. 19^0.
I. N. Sokolova	Jnl. of ARS. i960. 22, p.375

17	R. H. Tien and G. E. Geiger	Jnl. Ht. Transf. 1967. 89, p.230
18	R. H. Tien and G. E. Geiger	Jnl. Ht. Transf. 1968. 90, p.27
19	R. H. Tien and V. Koump	TMS, AIME. 1968. 242, p.1283
20	Schneider	Jnl. of Aeora Space Scienc. 1960. 27, p.546
21	W. C. Reynolds and T. A. Dalton	ASME Paper No. 58-A. 1958, p.248
22	A. I. Veinik	Approx. Calc. of Ht. Lond. Proc. Gosud Energetich. Izdat., Moscow. 1959. para. 24
23	A. W. D. Hills	Proc. Symp. Chem. Eng. in the Met. Ind. Inst. Chem. Eng. 1963. p.123
24	A. W. D. Hills	Jnl. Iron Steel Inst. 1965. 203, p.18
25	E. M. Sparrow	Discussion of "The Melting of Finite Slabs" by T. R. Goodman and J. J. Shea Jnl. Appl. Mech. 1960. 27, Trans. ASME. 1960. 82E, p.598
26	T. J. Lardner and F. V. Pohle	Trans. ASME. 1961, June. p.310
27	Rayleigh, Lord	On the Dynamics of Revolving Fluids. Scientific Papers. 16b, 6, p.447
28	Th. V. Karman	4th Int. Cong. Appl. Mech. 1934. p.54
29	J. L. Synge	Proc. Roy. Soc. '389, A167, p.250

30	L. A. Dorfmann	Hydrodynamic Resistance and Heat Loss of Rotating Solids. 1963* Oliver and Boyd.
31	**G. I.** Taylor	Phil. Trans. **Roy. Soc.** 1923. **P23A**, p.**281**
32	W. W. Hagerty	Trans. **ASME**. 1950. 72, p.54
33	F. S. Grunow and .H. Hein	Z. F. Flugwiss. 1956. Heft I/1 p.28
34	Pai. S. I.	MCA Tech. Rote. 892, 1943, p.1
33	E. M. Sparrow and ¥. 0. Munro and V. K. Jonsson	Jnl. Fluid Mech. 1964. 20/1, p.35
36	J. T. Anderson and 0. A. Saunders	Proc. Roy. Soc. 1953. 217A, p.555
37	Dropkin and A. Carmi	**Ht**. Transf. and Fluid. Mech. Inst. Stamford Univ. California. 1956*
38	V. M. Kays and **I.** S. Bjorklund	Trans. ASME. 1958* 80, P*70
39	**G.** A. Etmund	Trans. ASME. 1955. *JJ_*, p.**1283**
40	I. S. Bjorklund and W. M. Kays	Jnl. **Ht**. Transf. 1959* Aug., p.175
41	Carl Gazley	Trans. **ASME**., 1958. 80, P*79
42	King	Jnl. **A**. M. Chem. **Soc**. 1935*57, p.1212
43	A. G. Ward and J. W. Taylor	J.I.M., 1957. 8£, P.35
44	J. K. Jackson and R. E. Grace	Phys. Chem. Proc. Met. Symp., Pittsburgh. 1959* April Part 1, p.633
45	Roald and W. Beck	Jnl. Elecirochem. Soc. 1951* 98, p.277

46	M. Eisenberg and C. W. Tobias and C. R. Wilke	Chem. Eng. Prog. Symp. 1955. 51, p.1
47	T. K. Sherwood and J. M. Ryan	Chem. Eng. Sci . 1959. 11, (2) p.81
48	R. G. Olsson, V. Koump and T. F. Perzak	TMS., AIME., 1965. 233, p.1654
49	ibid 1966	TMS., AIME., 166, 236, p.426
50	R. D. Pehlke, P. D. Goodell and R. W. Dunlop	TMS. AIME. 1965. 233, p.1420
51	J. M. Lommel and B. Chalmers	TMS. AIME. 1959. 215, p.499
52	R. Ohno	Met. Trans., 1973. 4, p.901
53	Jackson and Chalmers	Canadian Jrn. of Phys. 1956. 34, p.475.
54	Hills A. W. D.	Ph.D Thesis Univ. of London. 1966
55	M. Kosaka and S. Minowa	Tetsu-to-Hagane. 1967. 53 p.1466.
56	W. Hofmann	Lead and Lead Alloys. New York. 1970. p. 98.
57	A. W. D. Hills and M. R. Moore	Met. Trans. 1969. 245. p. 1481

ACKNOWLEDGEMENTS

I wish to acknowledge the help of all the Research Section and Staff of Sheffield Polytechnic Department of Metallurgy, in particular Dr. B. Hattersley. The continuing encouragement and support of Dr. A. W. D. Hills during his supervision has been invaluable.

I also take this opportunity of thanking Mr. A. T. Sheridan of BSC Special Steels Division, Research and Development Department, for his assistance in this work.

A large part of the work was financed by the Turkish Research Council (Tubitak), to whom thanks are due.

More recently, the typing of Mr. E. W. Chandler has been an essential part of this work.